Meso- scale Wind Variability. Final Report

Larsen, Søren Ejling; Larsén, Xiaoli Guo; Vincent, Claire Louise; Sørensen, Poul Ejnar; Pinson, Pierre; Trombe, Pierre-Julien; Madsen, Henrik; Cutululis, Nicolaos Antonio

Publication date:
2011

Document Version
Publisher's PDF, also known as Version of record

Meso- scale Wind Variability. Final Report

Risø-R-Report

S. Larsen, X. Larsén, C. Vincent, P. Sørensen,
P. Pinson, P-J Trombe, H. Madsen, N. Cutululis
Risø-R-1794(EN)
November 2011

Risø DTU
National Laboratory for Sustainable Energy

Author: S. Larsen, X. Larsén, C. Vincent, P. Sørensen, P. Pinson, P-J Trombe, H. Madsen, N. Cutululis
Title: Meso- scale Wind Variability. Final Report
Energinet.dk project 2007-1-7141
Division: Wind Energy

Risø-R-1794(EN)
November 2011

Abstract:
The project has aimed to characterize mesoscale meteorological phenomenon for the North Sea and the Inner Danish waters, and additionally aimed on improving the predictability and quality of the power production from offshore windfarms.
The meso-scale meteorology has been characterized with respect to the physical processes, climatology, spectral characteristics and correlation properties based on measurements from wind farms, satellite data (SAR) and mesoscale numerical modeling (WRF).
The abilities of the WRF model to characterize and predict relevant mesoscale phenomenon has been proven. Additionally application of statistical forecasting, using a Markov switching approach that can be related to the meteorological conditions, to analyze and short term predict the power production from an offshore wind farms have been documented.
Two PhD studies have been conducted in connection with the project.
The project has been a cooperative project
between Risø DTU, IMM DTU, DONG Energy,
Vattenfall and VESTAS. It is registered as Energinet.dk, project no. 2007-1-7141.

ISSN 0106-2840
ISBN 978-87-550-3937-7

Contract no.:

Group's own reg. no.:
(Føniks PSP-element)

Sponsorship:

Cover :

Pages:
Tables:
References:

Information Service Department
Risø National Laboratory for
Sustainable Energy
Technical University of Denmark
P.O.Box 49
DK-4000 Roskilde
Denmark
Telephone +45 46774005
bibl@risoe.dtu.dk
Fax +45 46774013
www.risoe.dtu.dk

Contents

1Preface

This report is the final report of the Energinet.dk project no. 2007-1-7141 " Meso-scale atmospheric variability and the variation of wind and production of offshore wind farms". The objective is to improve power quality and prediction of efficiency for offshore wind farms by understanding the meso-scale meteorological phenomena causing significant variability in wind speed over areas of the size of the present and future offshore wind farms. The overall idea behind this objective is that a number of meso-scale meteorological phenomena, due to their spatial and temporal scales, will induce higher correlations between the outputs of nearby turbines and nearby wind farms than anticipated in the standard models build on boundary layer turbulence formulations. Within this project therefore, the overall objectives are met by enhancement of the understanding and predicting ability of short term wind variations caused by the meso-scale effects, as well as by efforts to integrate these aspects of the meteorology into the wind power prediction soft-ware.
The following organizations participated in the project:
Wind Energy Division Risø DTU, IMM DTU, DONG Energy, Vattenfall, and VESTAS.

After an initial evaluation of the different meso-scale phenomenon over the Danish waters, the following meso-scale phenomena were considered: Convective structures during atmospheric unstable conditions, transient mini-fronts and thunderstorms, and internal wave induced wind variability, under thermally stable conditions. The transient phenomenon was removed from the present project after initial efforts, because another project, especially focused here and established with an associated observation program (Radar at Sea, PSO 2009-01-0226). Therefore the focus in the present project has been on analysis of wind data from Horns Rev and Nysted wind farms to establish the smaller scales and variability (a few kilometres and 10 minutes) and using WRF model simultaneous simulations to establish the variability over scales from about five km to hundreds of kilometres. WRF is the current dominating meso-scale meteorological model at use at Risø DTU.

From the work, we have established climatology and the statistics of the meso-scale wind variability for the different stability categories for the North Sea and the Baltic. (Larsén et al. 2011, Larsen et al, 2011, Vincent et al. 2011a)
In the process we have established the meso-scale cross correlations between winds at different points, to be used in simulation programs for wind farm productions (Vincent et al. 2011a, Vincent et al. 2011b, Sørensen et al. 2002).
Of the different convective elements of importance for wind farm production, the so called "open cells" with horizontal scales of 20-60 km has been found to be the most important, both with respect to wind speed variability 5-20 m/s, and to probability of 25-50 cases per year for the North Sea. (Vincent, 2011, Vincent et all 2009a-d)
The conditions over the Baltic Sea are more thermally stable, therefore the occurrence of internal gravity waves is more important here. They can be random and hard to distinguish from turbulence, but the clearer ones seems typically to have a period of about 10 minutes and spatial scales between wavelengths 5-20 km, with very long wave fronts. (Larsén et al, 2010 and 2011). In the project they have been tracked using the data at Nysted, Synthetic Aperture Radar and WRF modelling for extensive spatial coverage.
In the process of the data analysis we have also proved the WRF model is able to describe and predict the key meso- phenomena approaching the wind farms both in the North Sea (Horns Rev) and the Baltic Sea (Lillegrund- Rødsand). This is important since WRF is our foremost prediction tool at Risø DTU. For shorter timescales, 2-10 hours into the future, prediction has become easier because the of variability climatology established (Taylors hypothesis has been found to be valid for the meso-scale wind variability and the variations have been found to have many characteristics of being two dimensionally isotropic).

The statistical aspects of the wind power prediction have been studied by the incorporation of regime switching models that allow parameters to be switched depending on the statistics of the time series. This regime-switching is closely linked to the prevailing meteorological conditions. (Trombe & Pinson, 2009.), but can as well react to variables that are internal to the wind farm.

2 Objectives

The objective is to improve power quality and prediction of efficiency for offshore wind farms through understanding of meso-scale meteorological phenomena causing significant variability in wind speed over areas of the size of the present and future offshore wind farms or wind farm clusters. Generally, a number of meso scale meteorological phenomena, due to their spatial and temporal scales, will induce higher correlations between the outputs of nearby turbines and nearby wind farms than anticipated in the standard models build on boundary layer turbulence formulations. Within this project therefore, the overall objectives are met by enhancement of the understanding and predicting ability of short term wind variations caused by these meso-scale effects, as well as by efforts to integrate these aspects of the meteorology into the wind power prediction soft-ware.
The meso-scale phenomena were broken down into a number of categories: Convective structures during atmospheric unstable conditions, transient mini-fronts with thunderstorms or rain bands, internal boundary layer effects near the coastline, and internal wave induced wind variability, under thermally stable conditions. All phenomena were integrated in the global analysis, such as distributions of winds, stability, annual and seasonal power spectra, etc. Also they were available in the data used to calibrate and test the statistical forecast systems, used in the project. However for the more detailed physical studies, the transient phenomenon were after initial studies (Draxl et al2009) removed from the present project, because they were being the focus by a parallel project, which was especially focused here and established with an associated observation program (Radar at Sea, PSO 2009-01-0226). Also near – coast processes were not considered directly, because the aim was more to obtain the generally valid results, on to which one could always build models describing the near cost processes. However, near coast data was unavoidable in the data, see figures of the sites, where they gave rise to variability, due to the near coast location of the two wind farm sites. Therefore the focus in the present project has been on analysis of wind data from Horns Rev and Nysted wind farms to establish the smaller scales and variability (a few kilometres) and using WRF model simultaneous simulations to establish the variability over scales from about five km to hundreds of kilometres. WRF is the current dominating meso-scale meteorological model at use at Risø DTU, where it is involved in the forecast of wind farm outputs as well.
The statistical aspects of the meso scale variability has especially been studied, using Markov-switching approaches in the statistical forecast models, thereby allowing the models to switch modes reflecting the different atmospheric conditions, including the transient conditions not considered in detail during the project.

3 Project Work

To structure the project, the meso-scale phenomena were broken down into a number of categories: Convective structures during atmospheric unstable conditions, transient mini-fronts and thunderstorms, internal boundary layers for air masses passing the coastal line, and internal wave induced wind variability, under thermally stable conditions.

All phenomena were by definition integrated into the global analysis, such as annual and seasonal power spectra, in the statistical forecast systems, since all data were used or available here.
However for the more detailed physical studies, the transient phenomenon were after initial studies (Draxl et al, 2009) removed from the present project, because it was already going to be studied by another project, which was especially focused here and established with an associated observation program (Radar at Sea, PSO 2009-01-0226). Also near –coast processes were not considered directly, but were indirectly present in some of the measurements and data, where the wind came from land. Such data were included in the studies to have enough data, to obtain a reasonable statistics.

Therefore, the focus in the present project has been on analysis of wind data from Horns Rev and Nysted wind farms to describe the associated scales and variability (a few kilometres and a few tens of minutes to a few hours) and using simultaneous WRF model simulations to establish the variability over scales from a few kilometres and up to hundreds of kilometres. WRF is the current dominating meso-scale meteorological model at use at Risø DTU for analysis and forecasts.
We have established climatology for wind, thermal stability and the statistics of the meso-scale wind variability for the different stability categories for the North Sea and the Baltic. (Larsén et al. 2011a, Larsen et al, 2011, attached to this report, Vincent et al. 2011a) . The sites appear from Figure 2, below, taken form Vincent et al, 2011a, attached to this report. The associated WRF simulation domains (basis domain and high resolution domain) are shown in the next figure, 3, taken from the same reference.

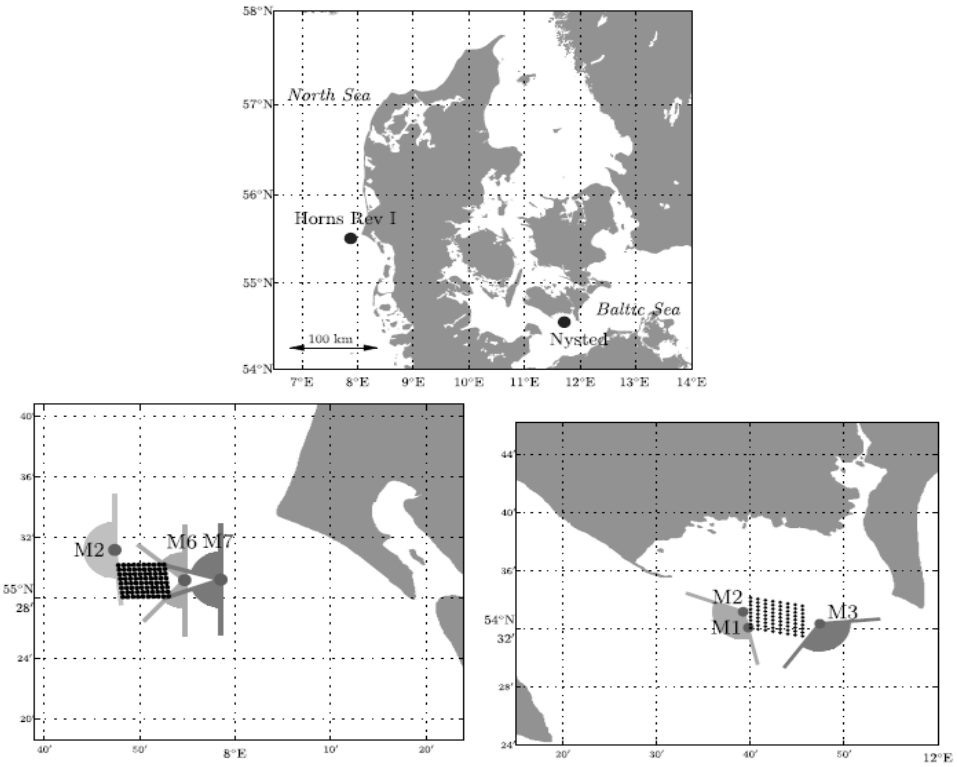

Fig. 2 The locations of the Horns Rev I and Nysted wind farms (upper plot), and the meteorological masts at the two sites (lower plots). The undisturbed flow sectors for the two sites are indicated by the shaded arcs.

Additionally, we have established the meso-scale cross correlations between winds at different points, to be used in simulation programs for wind farm productions (Vincent et al. 2011a, Vincent et al. 2011b, Sørensen et al. 2002).

The overall climatology, distribution function and annual and seasonal spectra, were based on the totality of data, fulfilling certain quality criterions. However, for detailed studies of the power spectra, cross-spectra and coherences as function of stability, a number of one- day-long data series were extracted,

which were considered to be reasonably stationary and homogeneity, and with a given stability and well defined characteristic features.

Of the different convective elements of importance for wind farm production, the so called “open cells” with horizontal scales of 20-60 km has been found to be the most important, both with respect to wind speed variability 5-20 m/s, and to probability of 25-50 cases per year for the North Sea. (Vincent, 2011, Vincent et all 2009a-d). These results agreed with earlier results from the German Bight (Hinzpeter, 1985). These open cell days were studied especially, to see their impact on the statistic parameters.

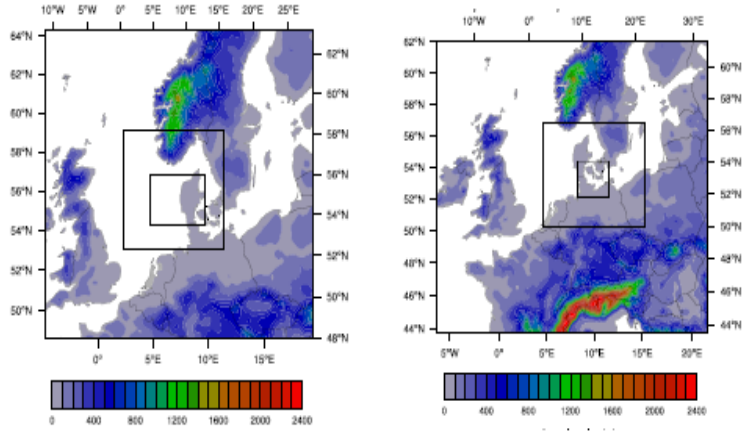

Fig. 3 WRF simulation domains. *Left* Domain for simulations over North Sea. *Right* Domains for simulations over Baltic Sea

The conditions over the Baltic Sea are more thermally stable, the occurrence of internal gravity waves is more important here. The internal waves typically appear as random internal waves that are virtually impossible to distinguish from turbulence, and hence, we made no such effort. However, also distinct and uniform internal waves appear, with uniform propagation and amplitude over most of the Danish waters. Over the Baltic such waves typically originate from thermally stable westerly flows impacting the Norwegian mountains. They seem typically to have a period of about 10 minutes and spatial scales between wavelengths 5-20 km, with very long wave fronts. They have been treated separately by Larsén et al, 2010 and 2011. In the project they have been tracked using the data at the Nysted masts, SAR (Synthetic Aperture Radar) and WRF modelling for extensive spatial coverage.
In the process of the data analysis we have also proved the WRF model is able to describe and predict the key meso- phenomena approaching the wind farms both in the North Sea (Horns Rev) and the Baltic Sea (Nysted), although the not necessarily the exact time of occurrence . This is important since WRF is our foremost prediction tool at Risø DTU.

In spite of these differences in conditions over the North Sea and the Baltic Sea, the power spectra, cross spectra and coherences were found to show very little sensitivity to the different conditions and in general being very insensitive to the changes in standard meteorological parameters. Some smaller modifications do appear however for selected situations, where the winds are strongly dominated by the convective cells or the distinct internal waves. (Larsén et al, 2011attached in this report).

Additionally to the simplifications above we found the meso-scale flow to show 2D isotropic characteristics (the power spectra looked alike in all directions, and the co-spectra between the two horizontal velocity components vanish).

For the meso-scale variations, we found as well Taylors hypothesis to apply, by comparing the spatial spectra extracted from WRF along the mean wind to the frequency spectra extracted from the mast data or the WRF simulations. The exceptions were here that for the distinct gravity cases, the simple Taylors hypothesis did not apply, but the phase speed of the waves had to be included).

On the statistical side, it was chosen to develop Markov-switching based approaches suitable for the analysis of time-series of power production at large offshore wind farms, as well as for very short-term forecasting of power generation (say, less than 2 hours ahead). The interest of these approaches is that they allow for the identification of an adaptation to various regimes with their own dynamics. It is expected that these identified regimes are physically motivated by various meso-scale phenomena, both those considered in detail in the present project and those that were not. In terms of data analysis, it then permits to extract crucial information for subsequently correlating regime sequences with the observed meso-scale phenomena or directly with onsite relevant measurements. This allows for instance for a linkage to the observation campaign of the previously mentioned Radar@Sea project. On the forecasting side, a number of other regime-switching and conditional parametric approaches were also considered and benchmarked, while new parametric distributions for the short-term probabilistic forecasting of wind power generation were proposed. All these statistical approaches were applied to various datasets available for the Horns Rev offshore wind farm.

4 Results

We have established climatology and the statistics of the meso-scale wind variability for the different stability categories for the North Sea and the Baltic. (Larsén et al. 2011, Larsen et al, 2011, Vincent et al. 2011a)
In the process we have established the meso-scale cross correlations and coherences between winds at different points, to be used in simulation programs for wind farm productions (Vincent et al. 2011a, Vincent et al. 2011b, Sørensen et al. 2002).

We have found that the annual- and the seasonal power spectra to be very similar for the North Sea and Baltic Sea sites. The power spectra, the co-spectra and the coherence functions have been found to largely insensitive to the atmospheric stability. Although closer inspection revealed that stability could be detected, by enhanced energy for higher meso-scale frequencies, of the order of 0,001 Hz) for unstable (convective) conditions and reduced energy for the stable conditions. The stable power spectra were found to be equally well represented by the conventional meso-scale spectral form and by the spectra, derived from considering the whole wind field as a superposition of random internal waves following the formalism from the abysmal ocean and the free atmosphere (Larsén et al, 2011, attached to this report). Since internal waves cannot exist for unstable –neutral conditions, one may wonder about the connection between the mesoscale spectra that equals the ones for stable conditions and the internal gravity waves. One explanation could be that the internal waves always exist in the layers above the unstable boundary layer, where they are to a large extent generated by boundary layer convection, and simultaneously can be considered the upper boundary for the convective variability taking place in the boundary layer.

We have found that the meso- scale spectra show 2 D isotropy characteristics, with vanishing correlation between the along and across wind fluctuations, relative to the mean wind, and with the spatial power spectra being equal in all direction, as found from the WRF simulations of the wind fields. From the WRF spatial spectra and the mast and WRF frequency spectra, we have found that the mesoscale wave number and frequency spectra can be related through Taylors hypothesis, i.e. through the mean wind speed.

All in all we have found the statistics of meso-scale wind speed to surprisingly simple. Only for very regular gravity waves, generated from the nearby Norwegian mountains, did we find systematic different behaviour of the coherence functions, now becoming strongly non-isotropic and wavy behaviour in the direction of the phase speed of the waves. Also the Taylor hypothesis was modified by the phase speed of the waves entering into the dispersion relation together with the mean wind. (Larsén et al, 2011 a, b). Also for data selected to represent convective open cell structures, both from the mast data and from WRF modelling, we found an enhancement for the scales representing the open cell activity, corresponding to the frequency –wave number spectral region, where one expects to find convective influence.

Of very important for the use of the meteorological modelling of wind farm production forecasting, we have found that the WRF model is able to predict the meso-scale features, we have studied, and hence that the WRF forecasts are able to predict events of meso-scale variability together with the forecast of the power production. In general we found WRF able to predict the physical and statistical properties of the meso-scale variations very well, but not the exact timing of their occurrence, although we for some cases also could get the match more precise, in the gravity wave case studied by Larsén et al (2011a,b).

The various Markov-switching approaches proposed were shown to be superior to classical linear statistical models for both the analysis of time-series and for short-term prediction of offshore wind power generation. The interest of considering that the parameters of these models should be time-adaptive was also shown (Pinson and Madsen, 2010). This implies that the dynamics of wind power fluctuations (at the time scales of a few minutes to a few hours) have evolving characteristics throughout the year, but also that the duration of the various regimes (and the transition from one regime to the next) changes in time. Such findings were confirmed by the climatology of wind power fluctuations reported by Vincent et al. (2011). The approaches proposed have shown their potential for further analysis of the power fluctuations at large offshore wind farms, which will be enhance when further observational data will be made available in the near future (eg. Lidar, weather radar, etc.). A general formulation of these Markov-switching models and of the estimation of their parameters was finally proposed (Trombe et al., 2011) to account for the dynamics in both the mean and variance of wind power fluctuations.
On the forecasting side, we proved that even though Markov-switching approaches may outperform classical linear models for the very short-term prediction of offshore wind power fluctuations, they would still be outperformed themselves if additional measurements (at least wind speed and direction from nacelle anemometry) were to be made available in real-time (Gallego et al., 2011). This is since observed wind characteristics onsite may allow to further characterize the dynamics of power fluctuations to be expected in the very-near future. Also, such observations may serve as a proxy for identifying the type of meso-scale phenomenon being prevailing at the time forecasts are to be issued. The resulting improvements in lead scores, like the Root Mean Square Error – RMSE for instance, are in the order of 5-7%. Finally when extending to the case of the probabilistic forecasting of wind power fluctuations, the proposed new parametric distributions allowed for an appropriate capturing of the stochastic behavior of the these fluctuations as a function of the average power level, or as a function of wind direction for instance (Pinson, 2011). With this type of approach, probabilistic lead scores were further improved by 5-10%. One of the main advantages of all statistical approaches developed is that they may be readily implemented in existing forecasting software in order to improve our ability to forecasting wind power fluctuations at resolutions from a few minutes to potentially up to 2 hours ahead.

5 Discussion

We have found the climatology of meso scale wind variability to be surprisingly simple and universal , with respect to power spectra, co-spectra and coherences, in spite of the undoubted general climate differences of the North Sea and the Baltic Sea, involving both universal spectral forms, 2D isotropy qualities, and the applicability of Taylors hypothesis, with the advection velocity connecting the spatial variation of the wind field and the temporal variation observed by a stationary observer.

On the instrumental side we have proved that the satellite radar, especially with SAR images, and WRF modelling both were useful tools in studying, describing and forecasting meso-scale variability. In general WRF has been shown to predict the physical and statistical properties of mesoscale phenomena very well, but not necessary the exact timing of their occurrence.

As a special feature, we have found that the stable power spectra were found to be equally well represented by the conventional meso-scale spectral form and by the spectra, derived from considering the whole wind field as a superposition of random internal waves following the standard formulation for the abyssal ocean and the free atmosphere above the boundary layer (Larsén et al, 2011, attached). Since internal waves cannot exist for unstable –neutral conditions, one may wonder about the connection between the meso-scale spectra, which equals the ones for stable conditions, and the internal gravity waves. One assumption is that the internal waves always exist in the layers above the unstable boundary layer, where they are to a large extent generated by boundary layer convection , and simultaneously can be considered the upper boundary for the variability taking place in the boundary layer.

The results above correspond to general conditions of the Danish waters. We repeat from the work description that we have disregarded non stationary data, reflecting frontal passages and rain bands (because these are considered more effectively within the focused studies of the PSO-project “Radar at Sea”). Also, the direct modelling of roughness and heat flux changes at near coast environments has been disregarded, both to obtain more general results, and because these effects are already reasonably well modelled. However, to allow us sufficient data for some of the studies, data influenced by coastal factors were included in the studies, and are responsible for some of the statistical variability seen in the results (Vincent et al, 2011, attached, and Larsén et al, 2011, attached)

Therefore, while our annual and seasonal statistics is based on the total data sets, the studies of cross spectra, coherence and Taylor hypothesis are conducted on selected fairly stationary and fairly homogenous data situations of a typical length of 24 hours, where a statistical homogeneous and stationary mean wind and flow field could be assumed.

For the Horns Rev/North Sea data we have used in total 4 years of data for cross spectral analysis and 8 years of data for wind and stability climatology and power spectral analysis . For the Nysted / Baltic Sea data, we have used 4 years of data for the similar analysis. For the two areas the stationary and homogeneous 24 hours data sets included 300 days of data sets from Horns Rev and about 200 days of data from Nysted, or about 20-25 % of the total data available. Therefore some of the simplicity and universality, referred to above, will be a results of our selection of the most stationary and homogeneous weather situations at the two sites. The reason for the data screening was of course to ensure that the data fulfilled the necessary criterion for the spectral formulations to apply (Homogenous and stationary flow fields). Therefore, many of the non-studied weather phenomena, like front and rain bands, will be present in the remaining 70-80 % of the data. However, they do contribute to the data included in the general statistics and the power spectral analysis, which are based on all available data.

A somewhat different data set was obtained from a day, where very regular gravity waves were generated over the Norwegian mountains. Here we found power spectra that were slightly modified only, but with systematic variations of the coherence functions, now becoming strongly non-isotropic and wavy along the direction of the phase speed. For this situation, WRF was found to be an excellent prediction tool for the observed gravity waves, not just their physical and statistical properties, but also the time and place of occurrence very well.
Also the Taylor hypothesis was modified by the phase speed of the waves entering into the dispersion relation. (Larsén et al, 2011 a, b). We documented that these situations appeared fairly often, since they are coursed by thermally staple flows hitting the Norwegian mountain ridge from the West, a situation occurring quite often. By conjecture we will argue that also for transient phenomenon, like fronts and thunder storms, one can use an effective advection speed in the Taylor hypothesis reflecting the mean speed of the system, rather than the mean speed calculated form a homogeneous stationary series.

These considerations are applied already in some short time predictions and can then be the basis for future work.

The various Markov-switching approaches proposed were shown to be superior to classical linear statistical models for both the analysis of time-series and for short-term prediction of offshore wind power generation. The interest of considering that the parameters of these models should be time-adaptive, to enable meso-scale characteristics to be included in the models, was also shown (Pinson and Madsen, 2010). The approaches proposed have shown their potential for further analysis and prediction of the power fluctuations at large offshore wind farms, which will be enhance when further observational data will be made available in the near future (eg. Lidar, weather radar, on-line wind farm production data, etc.).

Education

A PhD project has been concluded in association with the project, Vincent (2011). Another PhD candidate has also been partly financed by the project (Pierre-Julien Trombe, DTU Informatics).

References

Brown, R. A. (1980) Longitudinal Instabilities and Secondary Flows in the Planetary Boundary Layer. Rev. Geophysics and Space Physics, 18, 683-697.

Hinzpeter, H. Editor, (1985) KonTur – Results. Contribution to Atmospheric Physics (Special issue), 58, 1-95.

Sørensen, P., A.D. Hansen, P.A. Carvalho Rosas (2002). Wind models for simulation of power fluctuations from wind farms. Journ. Wind Engineering and Inst. Aerodynamics, 90, 1381-1482.

From this project:

Gallego,C., P. Pinson, H. Madsen, A. Costa, A. Cuerva (2011). Influence of local wind speed and direction on wind power dynamics – Application to offshore very short-term forecasting. Applied Energy, 88(11), pp. 4087-4096

Draxl, C., Vincent, C., Hahmann, A., Giebel, G., Pinson, P.: 2009, Variability forecasts for wind farms using high resolution initial conditions. Presented at the 8th International Workshop on Large-Scale Integration of Wind Power into Power Systems as well as on Transmission Networks for Offshore Wind Farms in Bremen 2009.

Hahmann, A. N., C.L. Vincent and C. Draxl. (209) Real time forecast system for Denmark: Verification of PBL Processes for wind power forecasting and resource assessment. Presented in workshop on WRF-modeling UK 2009.

Larsen, S.E., X G. Larsén, C. Vincent and P. Sørensen (2011) Mesoscale variability of winds. Presented at Workshop on integration of Geospheres into Earth Systems, Dubrovnik 30.4-3.5., to appear in: Geofizika.

Larsén, X. G., S E Larsen and M. Badger, (2011a) A case study of mesoscale spectra of wind and temperature, observed and simulated. Quarterly Journal of the Roy. Met. Soc. 137, 264-274.

Larsén, X. G. , S E Larsen and A. Hahmann, (2011b) Origin of the waves " A case study of mesoscale spectra of wind and temperature, observed and simulated". Quarterly Journal of the Roy. Met. Soc. DOI: 10.1002/qj.916

Larsén, X. G., C. Vincent and S. E. Larsen (2011). Spectral structure of mesoscale winds over the water . In Preparation for Quarterly Journal of the Roy. Met. Soc. or Boundary Layer Meteorol. Attached to this report.

Sørensen, P. and N. A. Cutululis (2010) Wind farm' Spatial distribution effects on Power System Reserves Requirements. Submitted to IEEE ISIE 2010 in 2009.

Pinson,P., H. Madsen (2010). Adaptive modeling and forecasting of wind power fluctuations with Markov-switching autoregressive models. Journal of Forecasting, available online

Pinson, P. (2011). Very short-term probabilistic forecasting of wind power with generalized logit-Normal distributions. Journal of the Royal Statistical Society C, In press.

P. Pinson, P. (2009). Regime-switching dynamics and nonstationarity of wind speed/power time-series. in Seminar Series: Texas A&M, Department of Statistics, April 2009. Invited talk

P. Pinson, P. (2009). Selected topics related to wind power modeling, forecasting and decision-making - Nonlinearity and nonstationarity. in Seminar series: Lund University, Center for Mathematical Sciences, November 2008

Trombe,P.-J., P. Pinson, H. Madsen (2011). Markov-switching AR-GARCH models for the characterization and forecasting of short-term offshore wind power fluctuations. Attached to this report

Trombe P-.J, Pinson P.(2009). Modeling and forecasting of wind power fluctuations using Markov Switching AR-GARCH Models. Presented at:
- 2nd SafeWind project meeting, March 25-27, Toulouse, France.
- International Symposium on Forecasting, June 21-24, Hong Kong.

Trombe, P.-J., P. Pinson, H. Madsen (2009). Modeling and forecasting of wind power fluctuations at large offshore wind farms. European Offshore Wind Conference, 14-16 September, Stockholm, Sweden

Vincent, C., Giebel, G., Pinson, P. and Madsen, H., (a) 2010, Resolving Non-stationary spectral information in wind speed time series using the Hilbert-Huang Transform. Journal of Applied Meteorology and Climatology 49(2), 253-267.

Vincent, C., Draxl, C., Giebel, G. Pinson, P., Jørgensen, J., and Möhrlen, C. (b) 2009, Spectral Verification of a Mesoscale Ensemble. Presented at EWEC 2009.

Vincent, C., Giebel, G., Pinson, P. (c) 2009, Characterisation of wind variability at the Horns Reef wind farm. Presented at EWEC 2009.

Vincent C. P. Pinson, G. Giebel. (d 2011) Wind Fluctuations over the North Sea. International Journal of Climatology 31(5), DOI: 10.1002/joc.2175.

Vincent C., Hahmann A. (2011). Hour-scale wind fluctuations over the North Sea. Presented at EWEA 2011.

Vincent C., Hahmann A., Kelly, M. (2011) Idealised WRF simulations of open cellular convection over the sea. In press in Boundary Layer Meteorology.

Vincent, C. (2010) Mesoscale wind fluctuations over Danish waters, Risø – PHD-7O (EN) 168 p.

Vincent, C., X. G. Larsén, S. E. Larsen, P. Sørensen (2011a) Complex cross-spectra from observation and mesoscale modelling.. Submitted to Boundary Layer Meteorology. Attached to this report

6 Attachments

The following three manuscripts all submitted to publication are the latest publications being derived from the Meso scale project, and together they summarize the findings

Larsén, X. G., C. Vincent and S. E. Larsen (2011). Spectral structure of mesoscale winds over the water. In Preparation for Quarterly Journal of the Roy. Met. Soc. & Boundary Layer Meteorol. Attached to this report.

Vincent, C., X. G. Larsén, S. E. Larsen, P. Sørensen (2011a) Complex cross-spectra from observation and mesoscale modelling.. Submitted to Boundary Layer Meteorology. Attached to this report

Trombe,P.-J., P. Pinson, H. Madsen (2011). Markov-switching AR-GARCH models for the characterization and forecasting of short-term offshore wind power fluctuations, submitted Applied Energy, Attached to this report

Risø DTU is the National Laboratory for Sustainable Energy. Our research focuses on development of energy technologies and systems with minimal effect on climate, and contributes to innovation, education and policy. Risø has large experimental facilities and interdisciplinary research environments, and includes the national centre for nuclear technologies.

Risø DTU
National Laboratory for Sustainable Energy
Technical University of Denmark

Frederiksborgvej 399
PO Box 49
DK-4000 Roskilde
Denmark
Phone +45 4677 4677
Fax +45 4677 5688

www.risoe.dtu.dk

Spectral structure of the mesoscale winds over the water

Xiaoli Guo Larsén*, Claire Vincent and Søren Larsen
Wind Energy Department
Risø National Laboratory for Sustainable Energy
Technical University of Denmark
xiaoli.guo.larsen@risoe.dk, +45 21327332

November 17, 2011

Abstract

Standard meteorological measurements from a number of masts around two Danish offshore wind farms have been used to study the spectral structure of the mesoscale winds, including the power spectrum, the co- and quadrature spectrum and the coherence. When average conditions are considered, the power spectrum has shown universal characteristics, in agreement with the findings in literature, including the energy amplitude and the $-5/3$ spectral slope in the mesoscale range transitioning to a slope of -3 for synoptical and planetary scales. The slope transition is found to be more dominant for winter seasons when the baroclinic instability is strongest in the mid-latitudes. It is argued that this slope transition could be an indication of the limit where the Taylor hypothesis could be applied. The local stability does not seem to systematically affect the average mesoscale power spectrum or the coherence, rather it is the particular atmospheric structures under these stability conditions such as the open cells in the North Sea and the gravity waves over Denmark that have their own spectral behaviors. The spectral behaviors for the along-wind and cross-wind components, including power spectrum, the co- and quadrature spectrum and coherence, are highly similar for the general cases that satisfy stationary conditions, and there is no statistically significant correlation between the along- and cross-wind components. The vertical variation of the power spectrum is found to be small and there is almost no vertical variation of the co- and quadrature spectrum and coherence. These

findings suggest that the mesoscale flow does bare the characteristics of 2D isotropy.

Keywords: Mesoscale range, power spectrum, coherence, 2D isotropy

1 Introduction

The spectral behavior of the wind speed in the mesoscale range, from a few kilometers to hundreds of kilometers, or, from a few minutes to hours, is not only a fundamental atmospheric research topic, e.g. [1, 2, 3, 4], but also important for practical use in wind energy application. Modern wind farms are of the size of tens of kilometers, which means that the power spectrum in the mesoscale range is an important measure of accuracy for short term forecasting [5] as well as extreme wind estimation [6]. The spatial coherence of wind is a key parameter for wind energy planning and power integration [7, 8] for single farm as well as groups of wind farms within a limited geographical area such as the North Sea. It is the purpose of this study to examine the spectral behaviors (including the power spectrum and coherence) in this range and to examine the impact from a number of factors, including seasons, horizontal and vertical dimensions, stability and mesoscale phenomenon such as gravity waves and cells.

In the literature, the spatial mesoscale power spectra have been studied with measurements (through airplanes [9, 10, 1, 4] and satellite [11]), theoretical arguments [2, 12, 3] and numerical simulations [13, 14, 15, 16]. The scope of these studies ranges from the atmospheric surface layer to the troposphere and lower stratosphere, and from tropical to mid-latitude and polar regions. Most of the studies have been done for stable conditions, although the impact of stability has only been clearly reported for the potential temperature spectra e.g. [1, 4, 16]. The spectrum for an individual unstable case in the boundary layer during a one-day period has, however, shown high resemblance to those in the literature for the stable conditions [16]. Within the boundary layer, measurements from 10 m to about 500 m of several days of period have shown negligible dependence of the power spectrum on height [4, 16]. Upper air measurements from airplanes reported some difference in the energy amplitude between the troposphere and stratosphere, with the amplitude slightly larger in the stratosphere [1, 10]. Dependence

of the energy amplitude on latitude has been observed by e.g. [10, 17]; according to the data measured with commercial airplanes in [10], the tropospheric energy amplitude for the meridional winds seemed to be largest in the latitude band of 45 to 60°N. Seasonal variability was reported in e.g. [10] where it was found the energy amplitude is smallest in summer and in [18] the FGGE-IIIa data showed that for the planetary and synoptical scales the energy amplitude is greatest in winter. This was argued to be caused by the strongest temperature gradient cross latitudes and therefore stronger baroclinic instabilities in winter time.

In spite of these variabilities, one consistent character of the spectrum reported in the literature is the spectral form that the energy amplitude decreases with wave number as approximately $k^{-5/3}$ in the mesoscale range and changes to k^{-3} at smaller wave numbers. The generally accepted theoretical interpretation to the k^{-3} behavior is the enstrophy cascade from large scale to small scale and that to the $k^{-5/3}$ behavior is the energy cascade from small scale to large scale. As illustrated in [1] (their Fig. 1), the source for enstrophy injection at the large scale end of the k^{-3} region of the spectrum is the geostrophic turbulence that is related to the baroclinic instability and the source of the energy injection at the small scale end of $k^{-5/3}$ could be the force of thermal stratification such as gravity waves [1] or convective cloud systems [19]. This theory for a two-dimensional (2D) turbulence was first presented by [20] and [21], supported through years by numerous theoretical, numerical and experimental studies, including [19, 1, 2, 22, 13, 3]. Experiments also suggested that the mesoscale 2D flow bares an overall isotropy character, reflected as the lateral and meridional wind components having very similar spectral form [1, 4, 16]. However, the isotropy was reported to be invalid in the presence of rigid gravity waves where more kinetic energy was found to be distributed along the wave propagating direction [16].

In many of these studies, the spectra were analyzed in the spatial domain in terms of wave number k. The bridging of the spatial domain to temporal domain (in terms of frequency f) is normally through the application of the Taylor hypothesis using the advection velocity U_0. Because of the role of the advection in the hypothesis, one would expect the Taylor hypothesis not to be valid for scales that are dominated by geostrophic turbulence where the spectral slope is approximately -3. Indeed, the mesoscale spectra have only been reported to be successfully transformed between k

and f for scales of several hundreds of kilometers, corresponding to periods shorter than about one day [9, 1]. Regarding measurements, the analysis has mostly been done for spatially distributed measurements using airplanes and satellites, while point measurements have been paid less attention for this purpose even though they are much easier to access, partly because of the difficulties associated with Doppler shifting. The Doppler-shifted frequency had posed serious problems for spectral studies, (e.g. [23]) and it needs to be taken into account in the presence of gravity waves [24, 16]. Gravity waves are ever-present in stable conditions in the form of rigid waves or random waves. In geographical areas of climatologically stable stratification (such as one of the study areas in the current paper), this is a general issue. Nevertheless, with their stably stratified data, [1] and [4] found the Taylor hypothesis to be valid, suggesting that, with all random waves combined, the spectra could represent a non-dispersive turbulence-like process even though the data represent an overall stable condition.

In modeling the power spectrum, [2] through structure function analysis derived an expression for the kinetic energy spectrum in the meso to synoptic scales in terms of a combination of k^{-3} and $k^{-5/3}$:

$$E(k) = d_1 k^{-5/3} + d_2 k^{-3} \tag{1}$$

with $d_1 \approx 9.1 \times 10^{-4}$ and $d_2 \approx 3.0 \times 10^{-10}$. Eq. (1) fits perfectly the experimental data from [10, 1]. For the frequency domain, in stable conditions, [24] took the Doppler shifting taken into account and derived the general intrinsic horizontal wave spectrum between the Coriolis frequency (f_c) and the Brunt-Väisälä frequency N(Eq. (14) in [24]). The model of [24] describes the wind fluctuations in the range $f_c < \omega < N$ in terms of random gravity waves. Assuming the angle between the flow and the wave number k is 0 or 180°, and assuming the portion of energy from random waves with phase speed $c = \omega'/k \geq 0$ (ω' is the radian intrinsic frequency) equals that with $c = \omega'/k < 0$, it was derived that for $f_c \ll \omega < N$,

$$E(\omega) \simeq \frac{E_0}{f_c \cdot (\omega/f_c)^2}(1 + \frac{\beta^2}{1+\beta}) \tag{2}$$

where E_0 is the total energy density for internal gravity waves, including kinetic and potential energy, ω is the radian observed frequency, and β is the ratio of the mean wind and a characteristic intrinsic horizontal phase speed of the wave field. β describes the Doppler shift effect and it ranges

between 0 (no waves) and 10 (reported for lower stratosphere, [25]). With the β effect, one would expect that in reality, with random waves of different characteristics filling the stable atmosphere, the spectral energy $E(\omega)$ varies within a certain range. From measurements in various research papers, [26] adopted $E_0 = 7.5$ J kg^{-1} as a typical value for the tropospheric gravity wave total energy. Note, in deriving Eq. (2), the authors have arbitrarily chosen a spectral slope of -2 in order to obtain an analytical solution.

Compared to the power spectra, coherence for the mesoscale range is much less explored. [8] (hereafter V2011) summarized the limited number of studies of coherence in the mesoscale range, including [27, 7, 28, 29]. These studies are almost all for wind energy applications. In literature, coherence is mainly studied in the microscale range, from meters to tens of meters, or, from seconds to minutes [30, 31, 32, 33]. It is seen that the power spectrum in the mesoscale range is much simpler than the microscale range due to its quasi 2D character and it is expected to be similar for the coherence. [8] studied the coherence of wind speed in terms of its two components, the co- and quadrature spectrum for offshore conditions in the Baltic Sea and the North Sea, where mesoscale modeling, analytical modeling and measurements were used jointly for distance between a couple of kilometers to about 13 kilometers. It was found that (1) the coherence depends on the flow angle in relation to the orientation of the target locations (2) the co-spectrum can be expressed as a function of frequency normalized by multiplying by separation distance and divided by advection speed. (3) there is slight dependence of the coherence on the studied area where the dominant weather features might be different.

Classical studies of the spectra are mostly based on measurements from segments of relatively short periods. Considering the scales are consistent in space and time, the point measurements can easily provide information for planetary to synoptical scales which are relevant for the energy amplitude in the mesoscale range. In this study we make use of standard meteorological measurements to re-examine the spectral behaviors regarding the kinetic spectral form and energy amplitude as well as coherence of wind speed. The purpose is not only for the basic research interest but also in the context of wind energy application, therefore the typical wind turbine hub height (around 70 m) is of particular relevance. The measurements are of several years long from two offshore sites, Horns Rev in the North Sea and Nysted in

the adjacent Baltic Sea water, the same as those used in V2011. The study will thus be in the frequency domain. We are particularly interested in two issues, one is the 2D isotropy character of the mesoscale turbulence and the other is the effect of stability on the spectral behavior. These two issues have not been explored in depth in the above mentioned studies. With years of measurements, the study can be easily extended from the well-studied stable conditions as exists in literature to less explored neutral and unstable conditions.

The measurements, together with the climatological background at the two sites, are introduced in Section 2 and the results of power spectra and coherence are presented in Section 3.1 and 3.2 respectively. Discussion and conclusions follow in Sections 4 and 5.

2 Measurements and climatology at Nysted and Horns Rev

Standard meteorological measurements from masts around two wind farms in Denmark are used. The wind farm Horns Rev I is located offshore in the North Sea (Fig. 1a and b), and the wind farm Nysted is located offshore in the semi-enclosed water that belongs to the Baltic Sea (Fig. 1a and c).

Around the Nysted wind farm there are several meteorological masts, three of which are used in this study (Fig. 1c), where the wind speeds were measured with cup anemometers at heights above mean sea level of 10, 25, 40, 55, 65 and 69 m. Wind vanes and temperature sensors were mounted at 10 and 65 m. Air pressure was measured at 10 m. From pressure and temperature, the potential temperature was calculated. Water temperature was available at 2 m depth at mast 2 (M_2) and 3 (M_3).

Around the Horns Rev wind farm, there are three masts around the wind farm (Fig. 1b). Only mast 2 (M_2) existed before the wind farm was built in 2003. On M_2, wind speeds were measured at 15, 30, 45 and 62 m (mast top), wind directions at 60 m and 43 m, temperatures at 55 m and 13 m, pressure at 55 m. Water temperature has been measured at 4 m deep. Since 2003, masts 6 (M_6) and 7 (M_7) are mounted, with instrumentation different from M_2; the wind measurements were measured at 20, 30, 40, 50, 60 and 70 m (mast top), directions at 28 and 68 m, temperature at 16 and 64 m and pressure at 16 m. Wind measurements at some heights are missing during

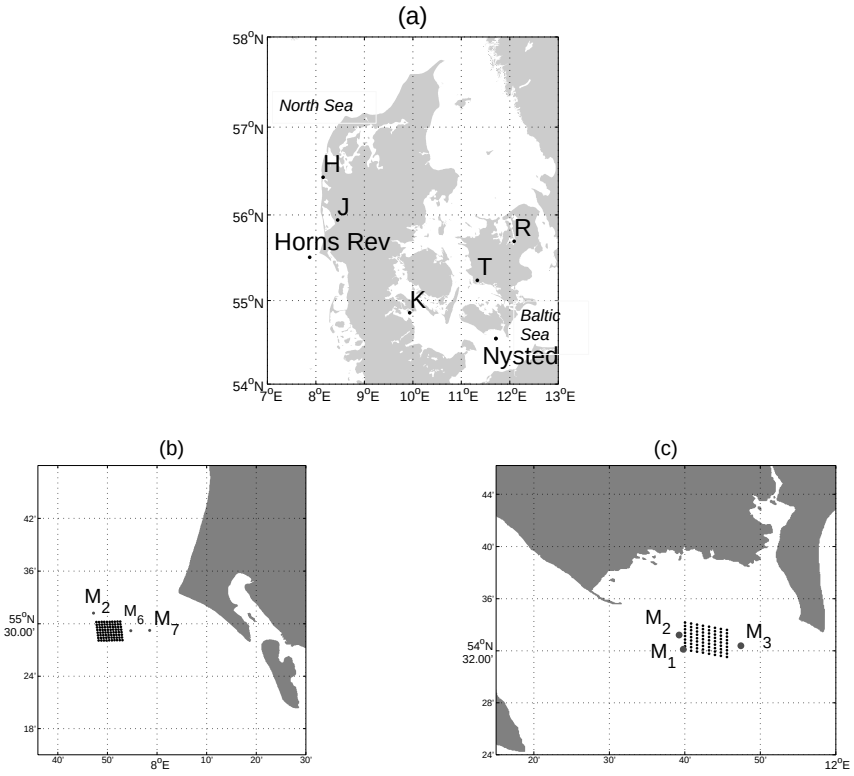

Figure 1: Maps and sites. (a) Map of Denmark and locations of Nysted, Horns Rev and several other stations labeled as H (Høvsøre), J (Jylex), K (Kegnæs), T (Tystofte), R (Risø). (b) The three masts and the wind farm at Horns Rev (c) The three masts and the wind farm at Nysted.

some periods, especially those at 30 and 40 m.

For both sites the time series used for the main analysis here are 10 min averages. The wind data availability for each mast at the two sites is described in Table 1. For a special analysis of a gravity wave case, 1 s time series at Nysted are also used.

Although both sites are offshore and geographically close to each other, the climatology is different regarding the stability conditions and wind distribution due partly to the different configuration of land and water around the sites. The Nysted wind farm, located in a water-body belonging to the semi-enclosed Baltic Sea and surrounded by land with relatively short sea fetches, has been reported to be of climatologically stable conditions due

predominantly to advection from land [34, 16]. At Horns Rev, the prevailing westerly winds from the open North Sea often accompany convective weather systems [35]. The monthly distribution of the Richardson numbers at the two sites are presented in Fig. 2, clearly confirming the climatologically stable conditions at Nysted and unstable conditions at Horns Rev.

The Richardson numbers are calculated with two methods. The first method is the same as in [16], i.e. to use measurements two measuring heights to calculate $Ri_B = \frac{g}{\theta} \cdot \frac{\Delta\theta}{\Delta z} \Big/ (\frac{\Delta U}{\Delta z})^2$. The two levels are 10 and 62 m at Nysted, and 15 and 45 m at Horns Rev; the temperatures at 15 and 45 m for the Horns Rev data are linearly interpolated from temperature measurements at 16 and 64 m. The other method is to calculate the bulk Richardson number between water surface and the lowest wind measurement level through $R_B = \frac{g}{T} \cdot \frac{(T-T_w)}{z} \Big/ (\frac{U}{z})^2$, with $z = 10$ m at Nysted and $z = 20$ m at Horns Rev. Due to the fact that the temperature gradient between two levels on M_6 and M_7 in Horns Rev are sometimes problematic and give suspicious statistics, and at the same time that there has also been concerns about the water temperature measurements at Nysted, both Ri_B and R_B are calculated whenever data are available at certain mast, so that they can be used as reference for each other. Note, for the Nysted site, in Figure 2a and c, Ri_B and R_B were calculated with the combined data at M_2 and M_3 from their undisturbed fetches because of the availability of water temperature measurements at the two masts. The results of Ri_B are consistent with M_1, even with the disturbed fetches included. For June, R_B was always greater than 0.015, which could be related to the large uncertainty in the water temperature (*check this out*). For the Horns Rev site, in Figure 2b, the calculation of Ri_B is done at M_2 for the period 1999 to 2005 and in Figure 2d, R_B has been calculated at M_7 for the period 2003 to 2007. When making the monthly statistics, at Nysted, the monthly data are only used if the data coverage is greater than 90%, and at Horns Rev, the monthly data coverage is required to be more than 99% because the data coverage is significantly better (Table 1). Note, the calculation of R_B is rather approximate by using water temperature at a certain depth (4 m deep at Horns Rev and 2 m deep at Nysted) and temperature, rather than potential temperature. Although, [36] showed that, at this particular site of M_2 at Horns Rev, the water temperature matched well with the sea surface temperature obtained from the satellite data. This, together with the different levels used for

calculating Ri_B and R_B, is actually of minor significance since our purpose is not to parameterize the stability effects but to use Ri_B and R_B to group data into approximate different stability categories. We see from Fig. 2 that in general the statistics of Ri_B and R_B are consistent, although the relative percentage could vary a bit when choosing different critical values for the grouping. Even though the data are not always from the same periods and not necessarily from the same masts, the consistent statistics from Ri_B and R_B suggests strongly the reliability of each of them for our grouping purpose and also suggests their representativity for the description of the stability climate.

Sensitivity tests are made regarding whether to use Ri_B or R_B and which critical value to choose, when grouping the data. When presenting the results, we use Ri_B for the power spectrum, both for Nysted and Horns Rev, and we use Ri_B for the coherence only for Nysted but use R_B for Horns Rev. It is always a big challenge with meausurements, regarding the data length, data coverage, technical failure and operating consistency, when we aim at making a climatological study. Even so, the data sets here, being in pairs, at multiple levels up to about 70 m, offshore and reasonably good quality, are very unique.

At Nysted, the stable situation is more related to flows from the sectors of east-south-northwest while the sector north-northeast contributes more to the unstable conditions. At Horns Rev, the unstable conditions are related to flow from the sea while stable conditions are more related to the flow from land.

3 Results

The results include the power spectra, the co- and quadrature spectrum and coherence. The power spectra are presented in Section 3.1, where the inter-annual variability, seasonal impact, variation with height and stability impact are examined. The daily spectra of both the along-wind and across-wind components, u and v, are shown. In Section 3.2, the coherence of wind speed for pairs of observations and its real and imaginary components, the co- and quadrature spectrum respectively, are presented for three pairs of masts at Nysted and one pair of masts at Horns Rev with the selected daily time series. The coherence of wind speed and the wind's two components, u

Table 1: Wind data coverage at each mast at the two sites

Year	Nysted			Horns Rev	
	M_1	M_2	M_3	M_2	M_7
1999				60%	
2000				99.975%	
2001				99.979%	
2002				99.9%	
2003				80.2%	46%
2004	52%	52%	52%	99.79%	90%
2005	95%	95%	95%	77%	98%
2006	92%	92%	92%	86%	89%
2007	52%	52%	53%	20%	73%
2008	35%	41%	41%		

Table 2: Masts and data description for the co- and quadrature spectrum and coherence studies, where dir range is used to select data for lateral or longitudinal separation conditions. $\parallel$ stands for longtitudional separation and $\perp$ stands for lateral separation.

Site	Masts	Orient.	Distance	Dir range		Nr.
Nysted	M_1, M_2	165°	2130 m	231 - 290°	($\perp$)	75
	M_1, M_3	82°	8178 m	136 - 200°	($\perp$)	36
	M_2, M_3	100°	8903 m	177 - 217° + 0 - 25°	($\perp$)	32
Horns	M_2, M_7	109°	12420 m	94 - 118°, from land	($\parallel$)	33
Rev				270 - 304°, from sea	($\parallel$)	150
				180 - 215° + 0 - 30°	($\perp$)	101

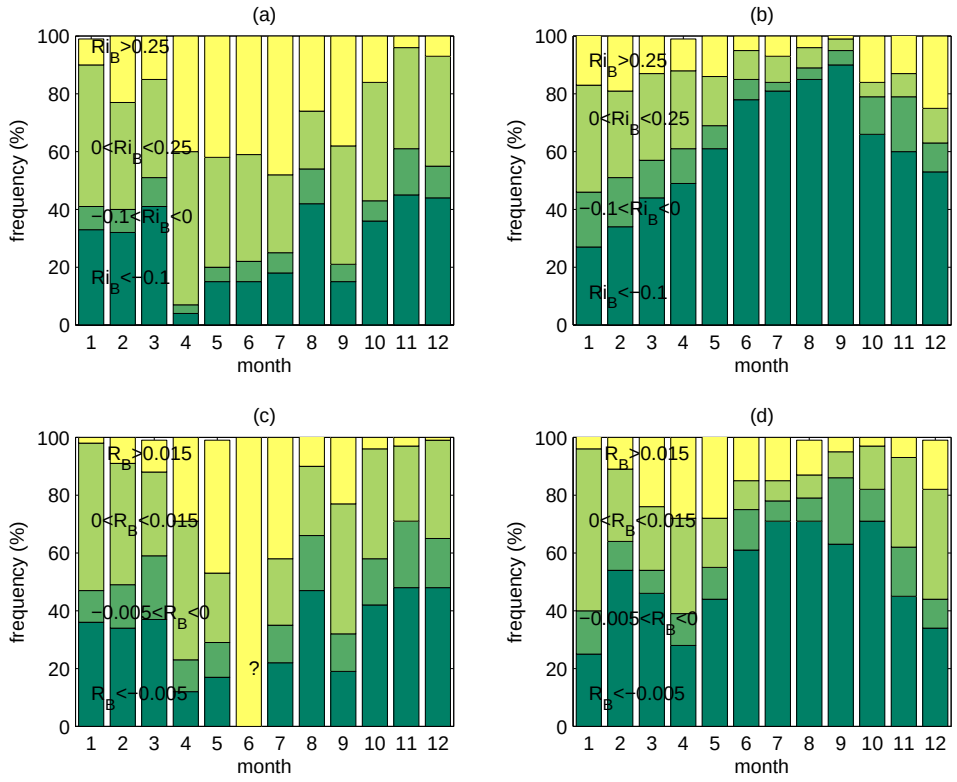

Figure 2: Monthly distribution of the bulk Richardson number at Nysted masts (a, c) and Horns Rev (b, d). In (a) and (b), the Richardson number Ri_B is calculated between two measuring heights, i.e. 10 to 60 m at Nysted and 15 to 45 m at Horns Rev. In (c) and (d), the bulk Richardson number R_B is calculated between water surface and the lowest wind measurement height, i.e. 10 m at Nysted and 20 m at Horns Rev.

and v, are shown for different stability groups.

3.1 The power spectrum

The annual wind power spectra are calculated using the Fourier Transform with a linear detrending applied to the yearly time series. The power spectral energy in the frequency domain is denoted as $S(f)$, to be distinguished from the references given in Section 1 where $E(k)$ is given for the wave number domain and $E(\omega)$ is for $2\pi f$. The annual spectra are only calculated for those years with best data coverage. According to Table 1, the Nysted data from 2005 and 2006 are used and the Horns Rev data from 2000 to 2002 at M_2 and 2005 at M_7 are used. There is almost no difference in the spectra from different masts during the same period. The year to year variation in the spectrum is obviously not important, as can be seen from Fig. 3a (Nysted) and c (Horns Rev). The results in Fig. 3 from data of several years demonstrate the following difference to be systematic: the logarithmic slope of the spectra at Nysted is straighter in the range $5{\cdot}10^{-6} < f < 10^{-3}$ Hz than that at Horns Rev where the spectra show a much clearer slope transition at a frequency of around $10^{-4.5}$ Hz. In Fig. 3b and d, the spectra at several measurement heights are plotted, indicating that there is some degree of vertical variation, which is more obvious at Nysted than at Horns Rev; the ratio of $S(f)$ between 55 m and 10 m is about 1.5 at Nysted and about 1.3 between 62 and 15 m at Horns Rev throughout the whole frequency range. Comparing Fig. 3c and d, one could see that at Horns Rev, the height dependence is systematic but is not more significant than the annual variability.

The average annual power spectra from the two sites (thin black lines from Fig. 3a and c) are put together in Fig. 4 and the difference in the energy amplitude is actually very small, with the ratio of $S(f)$ on average 1.01 for $5{\cdot}10^{-6} < f < 10^{-3}$ Hz, even though the Horns Rev spectrum shows stronger curvature. Also shown in this plot is the model of Fritts and Zandt [24], Eq. (2) with $\beta = 0$, which corresponds to no gravity waves. This model, with a slope of -2 and $E_0 = 7.5$ J kg^{-1}, seems to overestimate our measurements mostly at for the scale greater than 10^{-4} Hz; for $3 \cdot 10^{-5} < f < 10^{-4}$ Hz, it overestimates on average by an order of 1.7. In the presence of gravity waves where $0 < \beta < 10$, the modeled energy level is greater. To the measurements, in analogy to Lindborg's model, Eq. (1) (see the black curve in Fig. 4), we

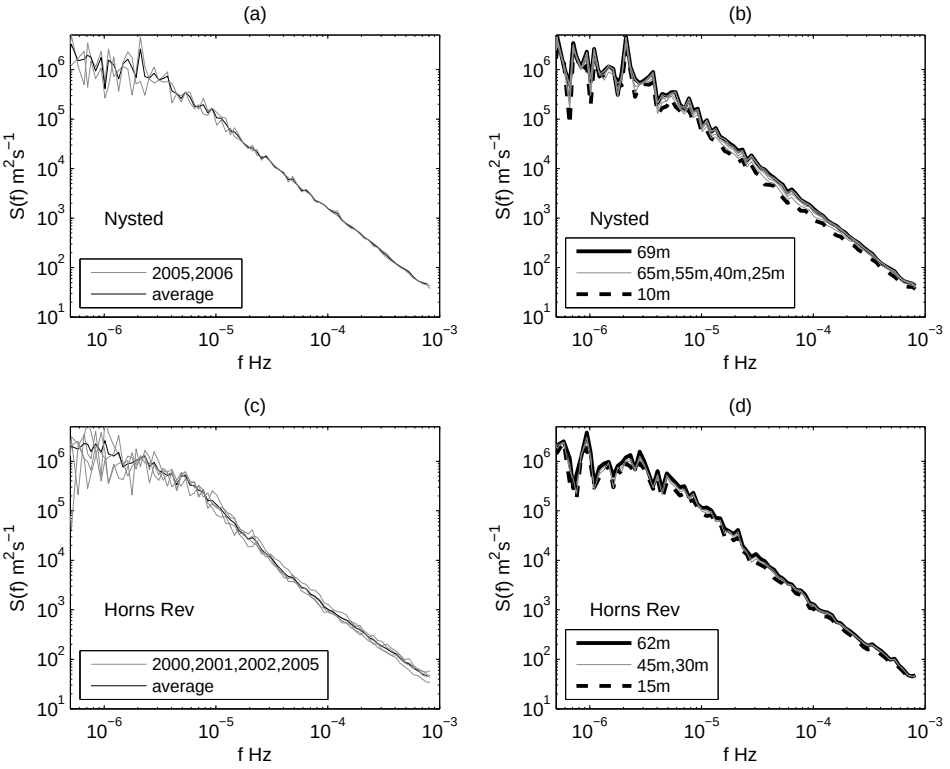

Figure 3: Power spectra from time series of 1 year long, at Nysted M_1 69 m (a and b) and Horns Rev M_2 62 m(c and d). (a) and (c): spectra from different years and an average spectrum for the site. (b) and (d): Spectra at several heights.

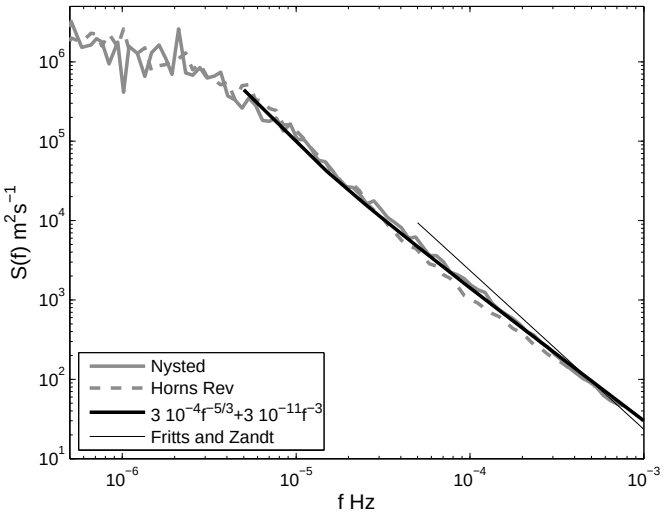

Figure 4: The yearly average power spectra from Nysted and Horns Rev, as the black curves in Fig. 3a and c, together with the model from [24] and the model of Eq. (3).

fit with the combination of $f^{-5/3}$ and f^{-3} and it gives a very satisfactory agreement with

$$S(f) = a_1 \cdot f^{-5/3} + a_2 \cdot f^{-3} \tag{3}$$

where $a_1 = 3 \cdot 10^{-4}$ and $a_2 = 3 \cdot 10^{-11}$.

The seasonal power spectra from the two sites are shown in Fig. 5a and b. Only months with data coverage greater than 95% are used for Nysted (due to the relatively low data coverage) and 99.9% for Horns Rev. From the Horns Rev data, it is found that changing the requirement of data coverage from 99% to 90% does not change the results, suggesting that using data of 95% coverage at Nysted does not bring statistically significant bias. From Fig. 5, it becomes immediately clear that summer months correspond to the relatively straighter spectrum where the range with $S(f)$ varying with $f^{-5/3}$ extends to very low frequency while the winter months corresponds to higher energy amplitude and a clearer slope transition from $-5/3$ to -3 at a relatively high frequency of about $2 \cdot 10^{-5}$ Hz (about half a day), see Fig. 5c and d for the winter and summer cases, respectively. The stronger geostrophic turbulence effect reflected in the -3 slope corresponds to a coefficient a_1 for the winter case several times larger than that for the summer

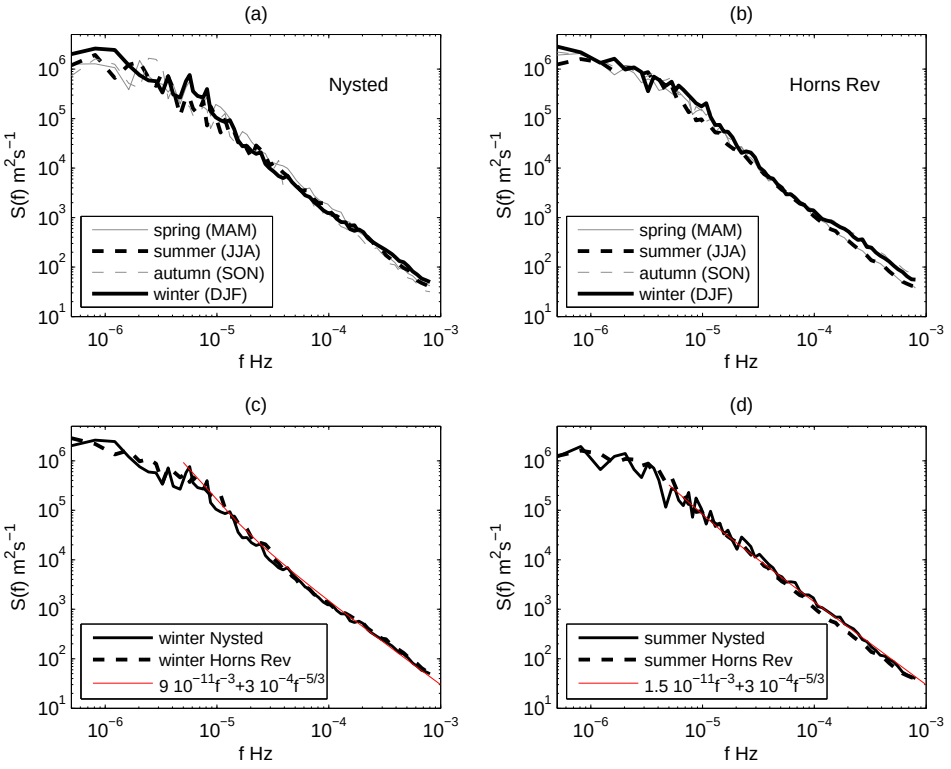

Figure 5: Power spectra in four season months. (a): Nysted. (b): Horns Rev. (c) Winter months for Nysted and Horns Rev and Eq. (3) with $a_2 = 9{\cdot}10^{-11}$. (d) Summer months and Eq. (3) with $a_2 = 1.5 \cdot 10^{-11}$.

case. Data from the two sites are highly consistent on this, in agreement with the findings in [10] and [18]; the stronger baroclinic instability in winter months is a reasonable interpretation. The overall annual spectrum from Horns Rev resembles more the winter months spectrum than that at Nysted, which could be an implication that the open sea condition at Horns Rev reserves better the geostrophic turbulence than the Nysted environment where the mesoscale land impact could play a significant role.

For the range with the $-5/3$ spectral slope, based on Fig. 3 to 5, when all conditions are mixed and averaged, the energy amplitude for both sites reaches a certain level; the dependence on year, the height and season can all be considered small. In the following we zoom in to this range by analyzing the daily spectra, with the aim to examine the possible impact of stability and to analyze the 2D spectral quality. All days that have 143 (the missing

data is linearly interpolated) or 144 10-min data are selected and grouped into three categories according to the daily mean Ri_B: $Ri_B > 0.1$, $0 \leq Ri_B \leq 0.1$ and $Ri_B < 0$, representing stable, neutral to stable (shortened to neutral) and unstable conditions, respectively. Using another value of Ri_B than 0.1 to group the data will only redistribute some of the cases within the first two groups, and the statistics remains same if it is not too different from 0.1, however using e.g. 0.25 will result in too few cases in the first group, which will make this group much less statistically meaningful. For all these days, it is required that the wind speed at the top measuring height does not vary more than 15 ms^{-1} per day and the direction change during a day is less than 50°. This ensures that the cases chosen for analysis approximate stationary conditions in order to be able to divide the wind into the along-wind (u) and cross-wind (v) components. Here we call data satisfying the stationary conditions for "normal" data. For the Horns Rev site, this analysis is done both for the period 1999 to 2002 and for the period 1999 to 2007; the former is before the wind farm existed and measurements at M_2 from all directions were used and for the latter, at M_2 only data free of the wind farm wakes were selected. Using the time series of 1999 to 2007 and the bulk Richardson number R_B to group the data into the three categories as $R_B > 0.05$, $0 \leq R_B \leq 0.05$ and $R_B < 0$ gives almost the same statistics as using the time series of 1999 to 2002 and Ri_B; this suggests the data representativity in this period and also the consistency of the results. In Fig. 6 the mean values of the daily spectra for the three categories are plotted for Nysted (left column) and Horns Rev (right column), together with their average annual spectra from Fig. 3a and c. For Horns Rev, data from 1999 to 2002 are used. Due to the series of strict restrictions to the data, for the Nysted site, there are only 36, 42 and 86 days in the three stability categories and for the Horns Rev site, there are 42, 18 and 197 in the three categories. For the neutral group, the mean spectra of both u and v are very close to the average annual spectra. Quite strikingly, for the stable group, at Nysted, the mean spectra correspond to considerably lower energy amplitude than the average annual curve. However, at Horns Rev the mean spectra are quite close to the average annual curve. For the unstable group, at Horns Rev, the mean spectra are of considerably larger energy amplitude at the high frequencies than the average annual curve (Fig. 6g) while this effect is not at all obvious for the Nysted data (Fig. 6c). Fig. 6g was based on almost

200 days of data, it is quite clear that the dominating unstable conditions at this site are responsible for the enhanced energy amplitude in the high frequency part of the mesoscale range, particularly in the winter and autumn seasons as seen in Fig. 5b. These results of higher energy amplitude during unstable conditions are consistent with the findings in [5] where a different spectrum analysis, Hilbert-Huang transform, was performed for this site.

For all groups in Fig. 6, the spectra of u and v are highly similar to each other. For each frequency, the ratio of the u- and v-power spectrum, $S_u(f)/S_v(f)$, is calculated. When putting the data from the two sites together, for f less than about $2 \cdot 10^{-4}$ Hz where there is higher uncertainty in the calculation of spectrum, the values of $S_u(f)/S_v(f)$ fluctuate around zero and for higher f, the average value of $S_u(f)/S_v(f)$ is about 1.2 - 1.3. The ratio of $S_u(f)/S_v(f)$ for this range has earlier been examined in [37] using 16 Hz sonic data from the Lammefjord experiment. From data of 11 periods ranging from 8 to 20 hours, they also found the similar spectral behavior for u and v for $10^{-4} < f < 10^{-3}$ Hz and the order of $S_u(f)/S_v(f)$ is about 1.5.

The co-spectrum of u and v for the three categories are plotted together in the last row for the two sites. The cospectra of u and v fluctuate around zero over the whole frequency range, even though the fluctuation could be rather big when the sample number is small (Fig. 6d and h), suggesting u and v are not correlated.

3.2 The coherence

The coherence study here was carried out with focus on the horizontal 2D behavior in terms of u and v, the vertical variation and the impact of stability. These issues were not the major subjects in V2011 where spatial correlations of wind speeds were studied. Because of these focuses, we construct and select the data slightly differently from V2011. The basic data length is still one day long. As for the calculation of the daily u and v power spectra, we select the "normal data", i.e. we require that the wind speed at the top measuring height does not vary more than 15 ms^{-1} per day and the direction not more than 50° per day. While V2011 explored extensively the effect of the inflow angle relative to the mast pair's orientation, we focus on two specific situations: the inflow along (longitudinal separation) and across (lateral separation) the displacement of the two masts. All data are required to be free of the wind farm wake effect. The direction restriction for the two

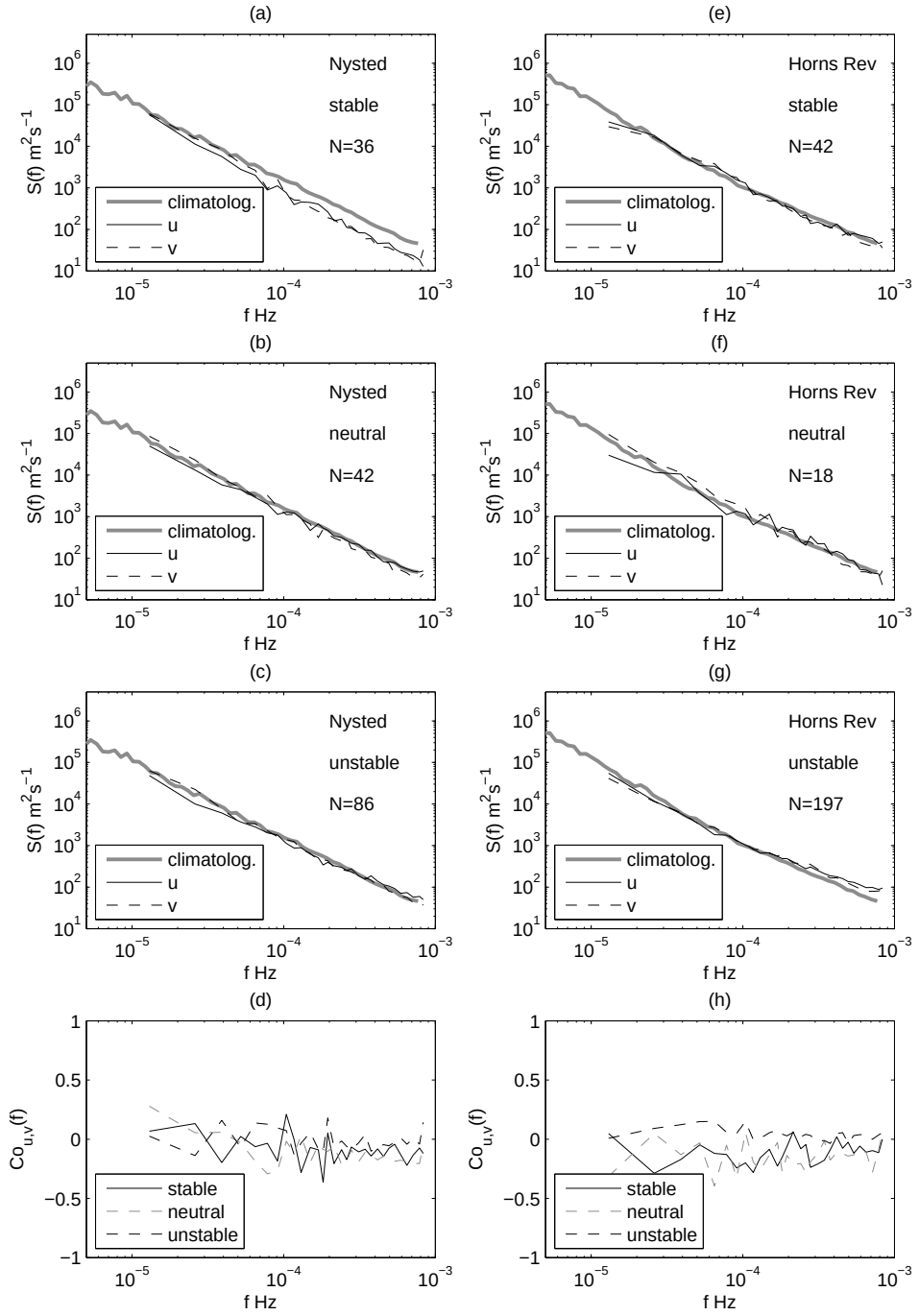

Figure 6: Power spectra from daily time series in three stability categories, with the daily mean $Ri_B > 0.1$ (a, e), $0 \leq Ri_B \leq 0.1$ (b, f) and $Ri_B < 0$ (c, f), for Nysted (left column) and Horns Rev (right column). (d) and (h): Co-spectra of u and v in the three categories.

situations for each pair of masts is described in Table 2. Three pairs of the three masts from Nysted are used for lateral separation study, the longitudinal separation cases are too few for obtaining the u and v components. At Horns Rev, only the pair with longest distance, M_2 and M_7, are used. The number of days that satisfy each category is given in Table 2.

Briefly, the algorithms for the key coherence parameters are displayed here. The coherence between the time series at two locations, i and j, is defined as

$$Coh(f) = \sqrt{Co_n(f)^2 + Q_n(f)^2} \tag{4}$$

where Co_n and Q_n are normalized co- and quadrature spectrum:

$$Co_n(f) = \frac{Co(f)}{\sqrt{S_i(f) \cdot S_j(f)}},\ Q_n(f) = \frac{Q(f)}{\sqrt{S_i(f) \cdot S_j(f)}} \tag{5}$$

As discussed in V2011, $Co_n(f)$ and $Q_n(f)$ together represent the in phase and out of phase of the wind variability at the two points i and j. S_i and S_j are the power spectra at i and j respectively.

Coh, Co_n and Q_n have been calculated for the wind speed and its along and across wind components, u and v, at all measuring heights. The time series went through a linear de-trending and a Hanning window was applied before Co_n, Q_n and Coh were calculated. Same as in V2011, the coherence was calculated from a block averaged single realization of the spectra and cross-spectra. Here our Q_n was calculated with an opposite sign as in V2011. This method was shown by [38] to be equivalent to averaging over a large number of time series, see V2011 for detailed discussion.

There is no variation of the three parameters with height observed. The slight increase of the power spectral energy with height, as shown in Fig. 3, is of negligible influence when used in Eq. (5), probably due to the much considerable more scatter related to the coherence parameters.

The results for u and v are shown in Fig. 7 (longitudinal separation) and Fig. 8 (lateral separation) for the top measuring height, which is 69 m at all Nysted masts, 62 m at Horns Rev M_2 and 70 m at Horns Rev M_7. Note, on the x-axis, it is a normalized frequency fd/U_0 where d is the distance between a pair of masts and U_0 here is the daily mean wind speed at corresponding heights, which for the Nysted data is 69 m and for Horns Rev is 62 m (data from M_7 are interpolated to this height). The normalized frequency, fd/U_0, is equivalent to $\frac{k \cdot d}{2\pi}$, with k the radian wave number; it describes the number

of waves within the separation distance of the pair of masts. Although the days selected are not necessarily the same as those selected in V2011 as discussed at the beginning of this section, the distribution of Co_n and Q_n for u and v here are consistent with those from V2011 for the wind speed on several matters. For the longitudinal separation of M_2 and M_7 from Horns Rev (Fig. 7a), for u, v and wind speed, Co_n decreases with fd/U_0, becomes negative at $fd/U_0 \approx 0.25$ and reaches a maximum negative value at $fd/U_0 \approx 0.5$, which means that the wind components at M_2 and M_7 are almost equally correlated, but the correlation decreases with increasing wave number and they becomes negatively correlated once there is one quarter of the entire wave between M_2 and M_7, and they become most negatively correlated when there is half of the entire wave between the two masts. The correlation seems to return to be positive again when the wave number is greater than 1. As also shown in V2011 for the wind speed, the quadrature spectrum shows opposite curves for cases with flow land and for cases with flow from sea. Here, Fig. 7b shows more profound out-of-phase distribution of the quadrature spectrum with frequency for the undisturbed flow from open sea than from land. For $fd/U_0 \approx 0.25$, M_2 and M_7 from Horns Rev clearly suggest u, v and the wind speed at the two masts are most out of phase when their separation distance is equal 1 to one quarter of a wave length, while M_1 and M_2 from Nysted does not reach this range.

This profound out-of-phase signal in the quadrature spectra for the wind speed is absent for the lateral separation, see Fig. 8b for u, which is almost the same as for the wind speed. Here Q_n moderately fluctuates around zero through all frequencies, indicating no systematic phase change at i and j. However, the plots for v (Fig. 8d and e) reveal a couple of small but interesting differences. For the lateral separation, when the u components are almost entirely un-correlated for $fd/U_0 > 0.5$, the v components at the two masts, now aligning with the masts displacement, are negatively correlated with each other in a similar way to u and v for the longitudinal separation situation, but to a much smaller degree. At the same time, Q_n shows v to be slightly but systematically out of phase at the two masts, most dominantly at $fd/U_0 \approx 1/4$. By comparing Fig. 7 with 8, one could see that, overall, the situation with lateral separation is much simpler, where Co_n and Coh as functions of fd/U_0 from both sites collapse onto a single curve (although there exists small differences) with limited scatter. For the

longitudinal separation, the scatter is a lot larger and the winds with flow from sea are better coherent than the lateral separation situation.

The results from Horns Rev and Nysted seem to be highly consistent; there are respectively 143 days and 183 + 101 days at Nysted and Horns Rev (see Table 2), and they should be of statistical significance.

It is obviously an application of the Taylor hypothesis to use fd/U_0 to describe the spatial coherence in Fig. 7 and 8. If plotted versus f only, the wind and its components are better correlated at shorter separation distance at the same f. The fact that Co_n and Coh as functions of fd/U_0 from both sites collapse onto a single curve suggests the validity of the Taylor hypothesis. That is, the dominant atmospheric movement included in the daily time series is through advection. In Fig. 7 and 8, the thin smooth curves are an empirical exponential fit to the $Coh - fd/U_0$ distribution for the wind speed, and it reads:

$$Coh = \exp\left(-14(fd/U_0)^3 + 20(fd/U_0)^2 - 10(fd/U_0)\right) \tag{6}$$

The purpose of the fitting is to use it as a reference for comparison.

In the analysis of stability effect, because of the high similarity in the $Coh - fd/U_0$ distribution between the different groups, we present in Fig. 9 only results for two of the groups of lateral separation, one is $M_1 - M_2$ at Nysted to cover the low frequency range and the other is $M_2 - M_7$ at Horns Rev to cover the high frequency range. The three stability groups at Nysted are defined the same way as for the power spectrum analysis in Fig. 6, i.e. $Ri_B > 0.1$, $0 \leq Ri_B \leq 0.1$ and $Ri_B < 0$. For Horns Rev, because of the unknown problems in the temperature gradient at M_7, we use the bulk Richardson number R_B to group the data as $R_B > 0.015$, $0 \leq R_B \leq 0.015$ and $R_B < 0$. A sensitivity test is done by changing the critical number of R_B to 0.005 and 0.05 for the grouping, and the largest consequence is that there will be too few cases in some categories. However, the statistical results are consistent in spite of scatter of different degrees. When Coh is plotted against f (Fig. 9a and b), there is no distinguishable difference between the three groups of data, suggesting that stability impact is not important, although only small differences could be obscured by the scatter in the data. However, there is a slight change when Coh is plotted against fd/U_0 (Fig. 9c and d). Due to the strongest winds in the neutral condition group and weakest winds in the stable condition group, there is a slight shift of the curves. As a result, at the same wave number fd/U_0, stable cases on

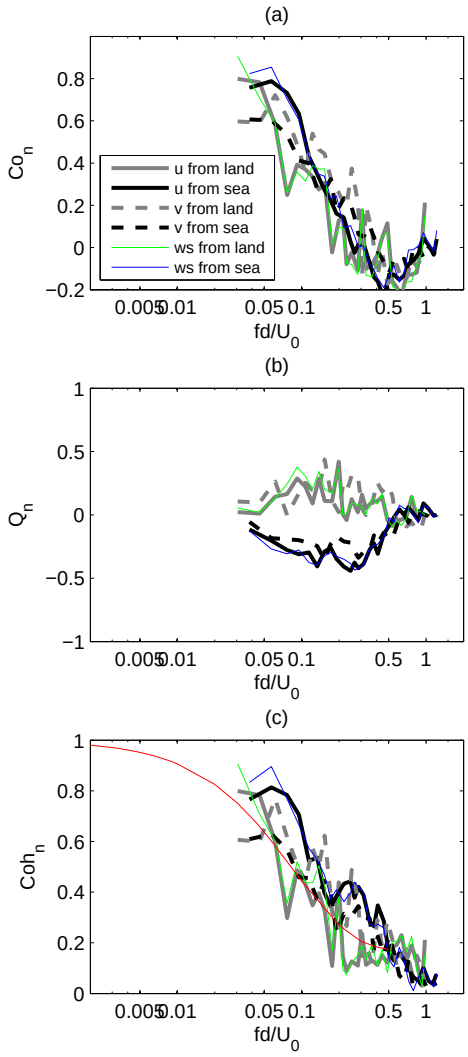

Figure 7: Longitudinal separation situations: Co_n, Q_n and Coh as functions of fd/U_0, for u, v and wind speed, for the four pairs of masts from Nysted and Horns Rev. The smooth curve in (c) is a reference from Eq. (6).

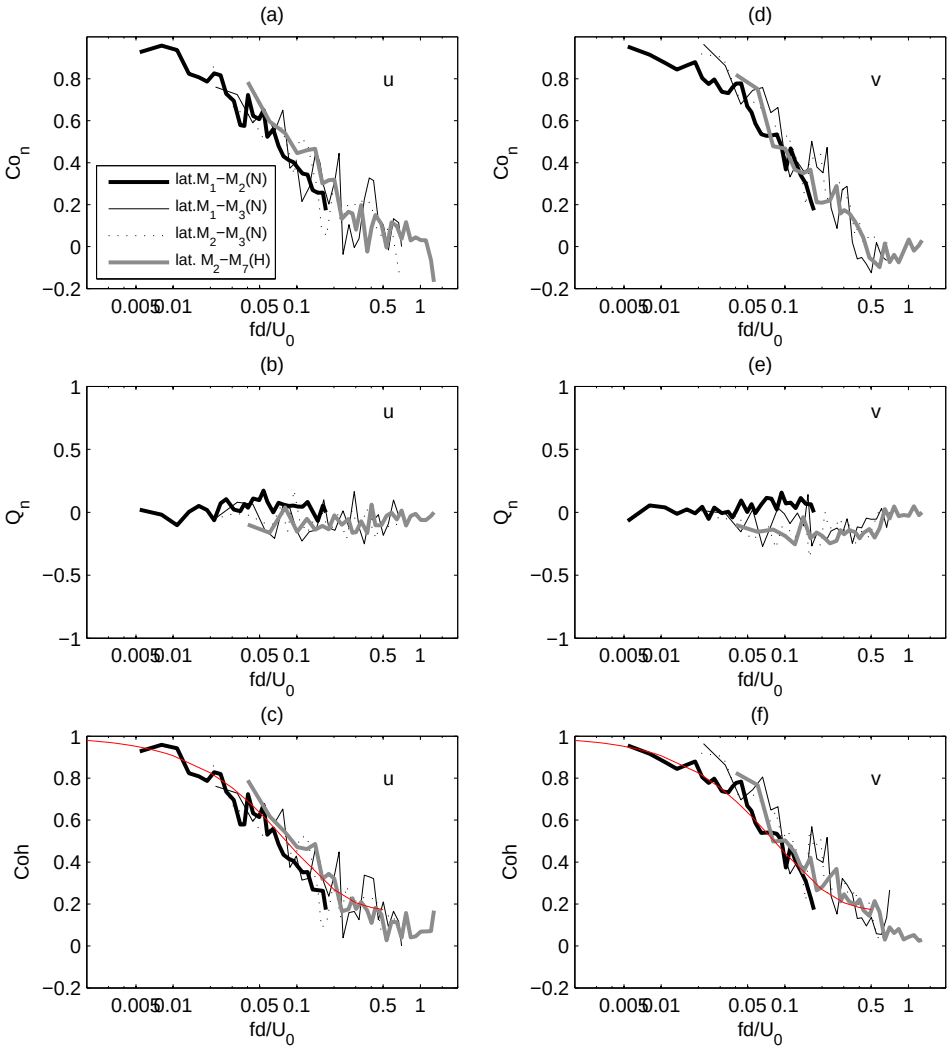

Figure 8: Lateral separation situations: Co_n, Q_n and Coh as functions of fd/U_0, for u (left column) and v (right column), for the four pairs of masts from Nysted and Horns Rev. The smooth curve in (c) is the reference Eq. (6).

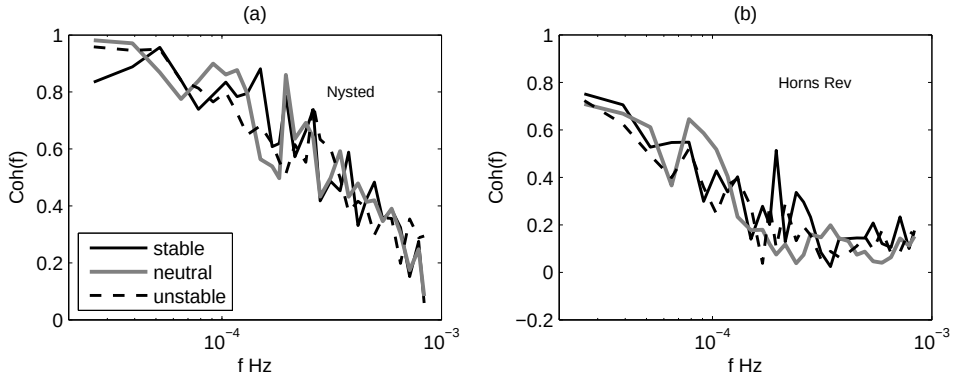

Figure 9: Coh of wind speed as functions of f (a, b) for the lateral separation between M_1 and M_2 at Nysted and M_2 and M_7 at Horns Rev.

average are best correlated and neutral cases are least correlated; however, the difference is very small compared to the scatter.

For each group, Coh has also been calculated for the u and v components as well as the wind speed. The results for the wind speed are very similar to those for u. The results for u and v are shown in Fig. 10. Even though in some plots, one curve is slightly higher than the other, but overall, Coh for u and v are very similar, and there is no clear impact of stability that can be detected.

4 Discussions

We have shown the potential of the standard meteorological measurements from two offshore sites in the mid-latitudes for studying the spectral structures in the meso to synoptical scales. Due to the continuity of scales in time and space, it was demonstrated that the point measurements could be used to successfully describe the spectral behaviors consistent with those in literature, which have mostly been reported in the wave number domain. Speaking of scales greater than a few kilometers or a few minutes, these structures include the power spectrum showing a slope of about $-5/3$ for relatively small scales and changing to a slope approaching -3 at larger scales, when plotted against frequency or wave number on log-log axes. The -3 slope behavior has been argued to be a consequence of the enstrophy transport from the large scale geostrophic turbulence. In agreement with the literature, our

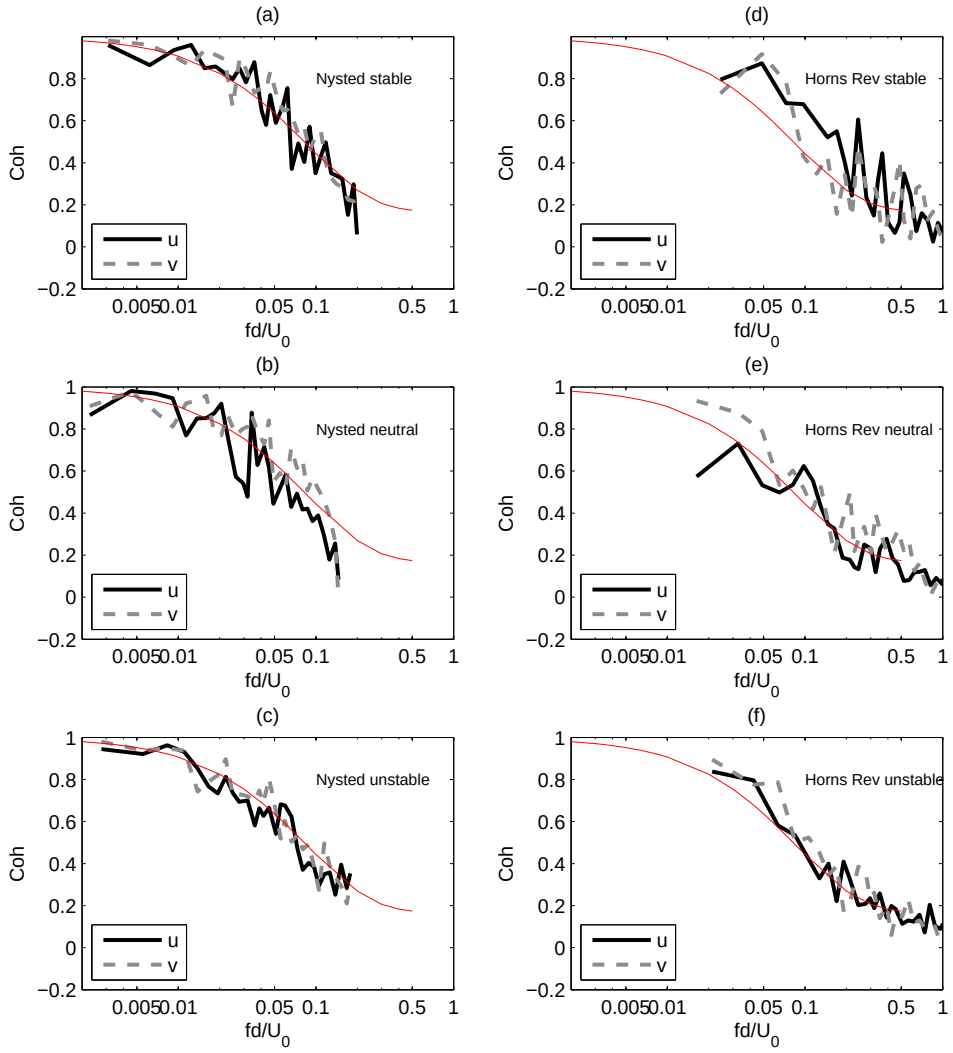

Figure 10: Coh as a function of fd/U_0 for u and v, Nysted (left column) and Horns Rev (right column), in three stability categories. The thin smooth curve in each plot is the same as that in Fig. 9, used as reference for the plot.

data also show the most dominant -3 slope during winter months, in relation to the strongest baroclinic instabilities in the mid-latitudes. Accompanying this, a more clear slope transition was observed for the winter months than the other months, especially the summer. Spring and autumn will inevitably overlap with winter and summer and they bare the characteristics somewhere in between. In the summer months, the $-5/3$ spectral slope extends to a scale of days, while in the winter months, the transition of the $-5/3$ to the -3 slope appears to happen at a smaller scale. This scale, where the spectral slope transition happens, represents the scale of the dominant local weathers and it is an important indicator for the application of the Taylor hypothesis. When we choose the length of the time series for the coherence and power spectrum analysis, we have chosen 1 day in this study. This is partly because it is the Coriolis frequency and partly because it has been reported in the literature that the Taylor hypothesis has been successfully applied for scales smaller than 1 day. One would not expect it to make sense to use fd/U_0 to normalize the frequency axes of the co- and quadrature spectra if U_0 does not only represent the advection of the same flow between the two locations, but also includes impact from the geostrophic movement. If we name the range with the $-5/3$ spectral slope the mesoscale range, the Taylor hypothesis seems only reasonable to be applied in this range. The conventional parameter to describe this weather scale is the integral time scale T, with $T = \int_0^\infty \rho(\tau)d\tau$, where ρ is the autocorrelation coefficient [39, 40, 6]. As shown in [6, 41], T calculated with measurements from Denmark is about 0.8 day on average. We calculated T here using the winter and summer months data with data coverage more than 99.99%. While the summer months give a similar T to the yearly data, i.e. about 0.8 day, winter months give a T of about 0.6 day. The difference in T for the prevailing weather dynamics in winter and summer implies that certain uncertainty has been introduced in the spectral analysis when we applied the Taylor hypothesis to all cases with one-day length time series.

The spectral behaviors for meso- to macro-scales seem to be well described by the combination of $-5/3$ and -3 slopes using Eq. (3), in analogy to Lindborg's description for the wave number domain. The measurements seem also fit well with the universal spectrum description for random gravity waves by [24] (Eq. 2) except that Eq. (2) overestimates on the order of 2 at the low frequencies of the mesoscale range. It is related to at least two

factors, firstly E_0, the total energy density of the troposphere, is used here and secondly that the slope of -2, instead of $-5/3$, was arbitrarily chosen by [24]. It is a question if our data from two offshore sites are only representative for offshore conditions and therefore partly responsible for the deviation from the model of [24]. For this, we used measurements from five more stations across Denmark and plotted their spectra together with those from Nysted and Horns Rev in Fig. 11. The locations of these sites can be found in Fig. 1a. Note, except for Høvsøre where 2006 was used, the data from 2001 were used for all other sites because the data coverage is almost 100% for all. Note also the measurement heights vary from 24 m to 100 m, which is expected to be partly responsible for some of the spectral energy amplitude differences. Overall, it can be concluded that the spectra from all these sites, including land, coastal and offshore, are consistent and therefore the power spectra from Nysted and Horns Rev in the meso to macro-scales do represent a universality for mid-latitudes. However, this universality does not dispel the possibility that there is slight vertical variation of the spectral energy amplitude as shown in our two offshore sites (Fig. 3b and d). This vertical increase of the energy amplitude is very small and it is speculated to be site-dependent. For all year round, the atmosphere at Horns Rev is much better mixed vertically due to its dominant unstable condition, the height dependence here is negligible while for most of the year the atmosphere around Nysted is of stable conditions. In spite of the fact that Eq. (3) and Eq. (2) are derived from completely different approaches for completely different mechanisms, the magnitude of the energy in the mesoscale range is rather comparable and both can be considered reasonably well for our measurements from several sites across Denmark.

The energy source to the mesoscale power spectrum has long been argued to be cascaded from the small scales through convective mixing or gravity waves. It is still an open question how the spectrum of the three dimensional small scale turbulence transitions to the mesoscale range for different conditions. According to Fig. 6, grouping the days into three stability categories reveals little systematic dependence of the wind spectra on the stability. Data from both sites tend to collapse with the climatological spectrum except for two situations. The two exceptions are the stable group at Nysted and the unstable group at Horns Rev. The former, Fig. 6a, shows an approximate $-5/3$ slope with comparable energy level to the climatological

spectrum only for scales greater than 3 hours, while for smaller scales, one can still say the slope is approximately $-5/3$ but the energy level is lower. The latter, Fig. 6g, shows good agreement with the climatological spectrum except for scales smaller than about 1 to 2 hours where the energy level is above the annual average. Fig. 6 therefore suggests that the local stability does not affect the mesoscale power spectrum systematically, it is rather the atmospheric structures behind that do. The selected 36 stable cases at Nysted with $Ri_B > 0.1$ obviously correspond to atmospheric motions with damped fluctuations at the scales 10 min to 3 hours than the 42 cases from Horns Rev with comparable stability conditions. The selected 197 unstable cases at Horns Rev with $Ri_B < 0$ show significantly higher fluctuations, very likely due to the actively convective system including cells structures that are common in this area [5, 35], which are less likely to happen in the Nysted area even with comparable unstable stability. In Fig. 13 the mean power spectrum for 18 individual cell cases from Horns Rev M_2 show clearly higher energy amplitude of wind speed than the climatological spectrum. The 18 days are of the longitudinal separation of M_2 and M_7, identified from visual satellite images from 2003 to 2006. Also can be observed from Fig. 13 is that the spectrum for u and v is not the same, suggesting that it is anisotropy during the cell conditions. The stable conditions at Nysted are favorable for gravity waves. One particular gravity wave case has been studied in [16] and [42] using the point measurements from Nysted together with satellite images and the Weather Forecasting and Research model over Denmark and adjacent waters. This case belongs to the neutral to stable group where the mean spectrum is very close to the annual mean spectrum. It was shown in [16] that the wind spectrum in the frequency domain is affected by the Doppler shifting effect. It seems that for our measurements, although individual cases bring fluctuations in the power spectrum in various ways, these fluctuations are averaged out when all situations are put together. One might expect higher energy even in the climatological spectrum It could then be questioned how the spectrum will look like in a place where one particular atmospheric motion is present most of the time, e.g. the cell convection is present about 50% of the time over Greenland and Barents Sea region in wintertime [**?**].

The stability does not either seem to matter much for the coherence (Fig. 9a and b) and the collection of stationary data seem to fit well with an ex-

ponential distribution with fd/U_0, which was already reported in V2011 for Co_n. Similar to the power spectrum, although the coherence for the stationary data seem to collapse to a certain distribution, individual cases with special structures do carry their own spectral characteristics. For the open cell structures at Horns Rev, Fig. 13 shows for the longitudinal separation, Co_n and Q_n do have more profound correlation and phase delay of u when the cell size is comparable to the separation distance between M_2 and M_7. The result for wind speed is very similar to that for u. The distributions of the three parameters are not the same for the u and v component, suggesting the spectral structure is not 2D isotropy for cell conditions. For the gravity wave case from [16], we used 1 s time series from 6 November 2006 to calculate Co_n, Q_n and Coh between M_1 and M_3 and the results are presented in Fig. 14. Since the wind was blowing through the wind farm, we expect the spectra be influenced somehow at $fd/U_0 \sim 6/8$, where 6/8 means the ratio of the wind farm length (approximately 6 km) and the distance between M_1 and M_3. As given in [16], the wavelength is about 12 km, thus M_1 and M_3 are approximately 3/4 waves away from each other. Clearly the spectral characteristics of u and v are different. The u component, aligning with the wave propagation direction, fluctuates wavelike with fd/U_0; it becomes sometimes entirely negatively correlated at the two masts. Co_n for the v component, on the other hand, decays exponentially with fd/U_0 but has a better correlation than the average curve with all situations included (the thin smooth curve). At the same time, the phase shift of u and v varies between $-180°$ and $180°$.

While we cannot draw decisive conclusions on the impact of stability, we may need to argue about the representability of the bulk Richardson numbers Ri_B and R_B, calculated from one point, even with the daily mean values, in describing properly the large scale stability conditions. In the future, we might consider using mesoscale modeling to obtain the bulk Richardson number of the boundary layer and take consideration of the spatial distribution of it, thus improving the description of the stability for this purpose.

Again, for the "normal" data that satisfy the stationary condition, the vertical variation of the power spectrum in the mesoscale range has shown to be small, only comparable to the seasonal variation, which is also very small. In the horizontal, Fig. 6 clearly shows that the along wind and across wind components, u and v, have very similar spectral characteristics, with

the power spectrum for u slightly larger than that for v, and u and v are not coherent. We thus interpret the results such that these "normal data" fit the description of 2D isotropy turbulence for the mesoscale range. By definition, 2D isotropy means that the turbulence of the wind is the same regardless of the direction. Without measurements over the whole space, it is hard to examine. Nevertheless, mesoscale modeling through the weather forecasting model can provide us such a wind distribution. [14] and [16] reported that the power spectra of the wind speeds from different transects in the model domain have the same power spectra, supporting the 2D isotropy turbulence for wind in the mesoscale range.

It is similar for the two points coherence, where u and v show very similar spatial dependence even though the scatter could be rather considerable due to limited number of samples (Fig. 10). It is a drawback that the number of samples for each category is limited because of the restrictions required for applying the statistic approaches. In V2011, cases with the wake effect of wind farm is included and therefore the number of cases is a lot greater than in this study. In spite of the wake effect, the coherence structure found in this study is consistent with those in V2011, suggesting the representability of the limited number of cases used here. The coherence decays exponentially with increasing wave number. If eddies in the one-day time series of all scales can be transported from one location to another through advection, we would expect the coherence to be 1 throughout all frequencies or wave numbers. The decreasing of coherence with increasing number of waves between the two locations suggests that the advection only transports the largest structures from one place to another, leading to the high coherence at the smallest wave number and the small scale fluctuations stay less- or un-correlated, same for u and v.

In the end, we would like to bring up a rather provocative hypothesis on why the power spectrum in the mesoscale range has a -5/3 slope. The spectrum is argued to represent an equilibrium state of energy transport that is under the impact of the elements of the earth itself. The following is a plot of the power spectra of the orography over mid-Europe. It is calculated from the SRTM elevation data (www.dgadv.com/srtm30), with a horizontal resolution of 3 km.

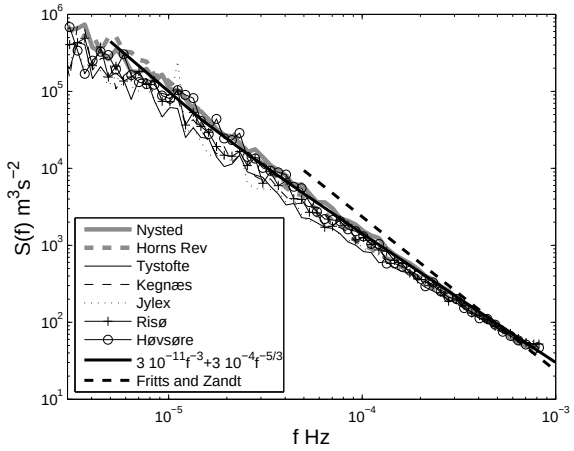

Figure 11: Annual power spectra of wind speeds from various stations.

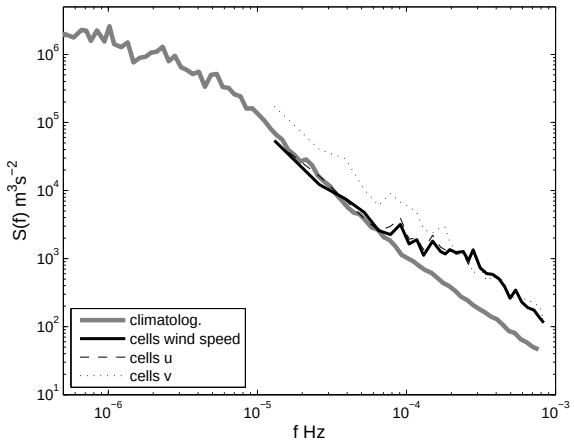

Figure 12: Mean power spectrum of 18 cases with open cell structures at Horns Rev, together with the mean annual spectrum from Fig. 3c.

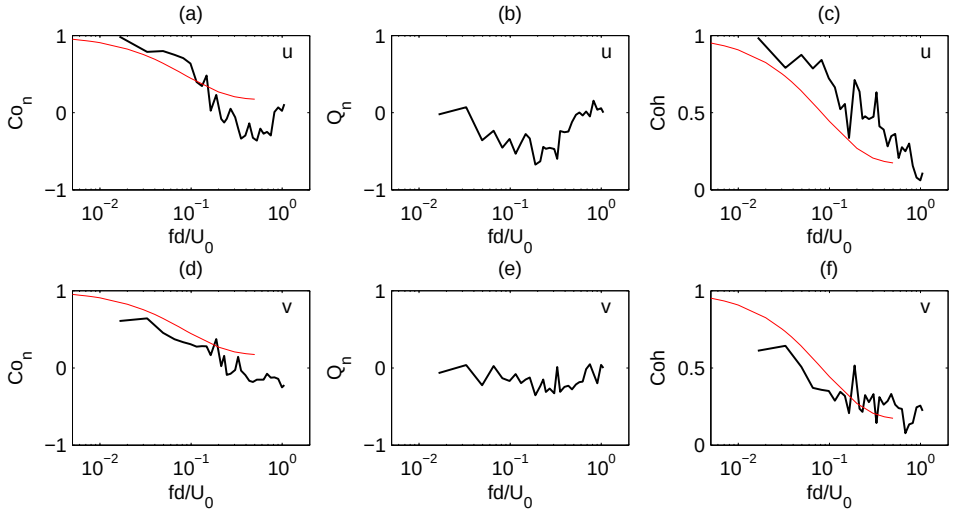

Figure 13: Co_n, Q_n and Coh between M_2 and M_7 at Horns Rev for the open cell cases, longitudional separation. The thin smooth curves in (a) and (c) are the reference Eq. (6).

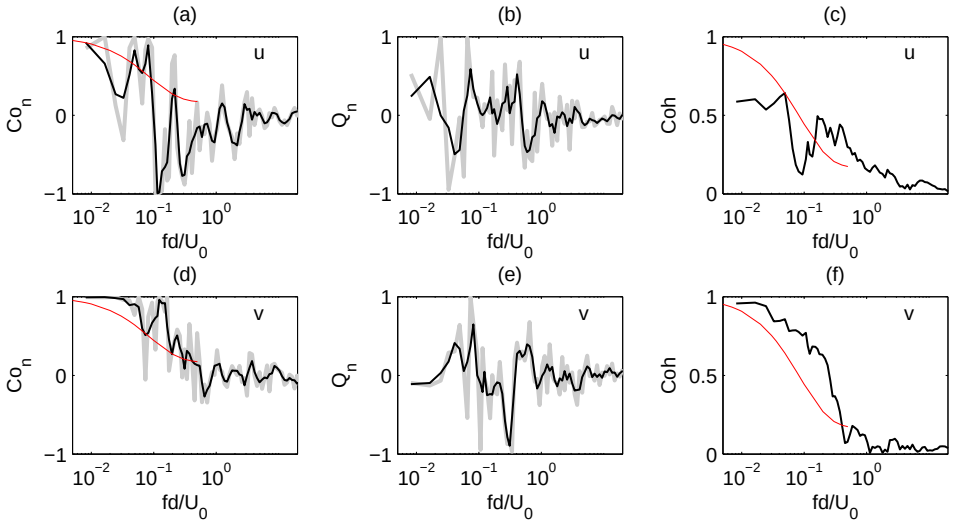

Figure 14: Co_n, Q_n and Coh between M_1 and M_3 at Nysted for the gravity wave case studied in [16]. The black curves are from the gray curves with running mean of three values. The thin smooth curves in (a), (c), (d) and (f) are the reference Eq. (6).

5 Conclusion

- The standard point meteorological measurements from tall meteorological masts over the sea can be used for studying the spectral structures of winds in the mesoscale range. The climatological wind power spectra from two offshore sites have shown some universality characteristics in agreement with the findings in the literature: the energy amplitude is comparable to the universal power spectrum model of [24] for random gravity waves; there is a $-5/3$ spectral slope in the mesoscale range which transitions to -3 toward synoptic and planetary scales; the slope transition is most dominant for winter months when the baroclinic instabilities are the strongest in the mid-latitudes.

- In the mesoscale range, the along- and cross-wind components, u and v, are not correlated and their spectral behaviors, including the power spectrum, the co- and quadrature spectrum and coherence, are very similar. This is a strong indication of the mesoscale 2D isotropy quality.

- The impact of stability is negligible for the coherence and does not seem to be systematic for the power spectrum. Specific atmospheric structures under the stability conditions bares their special spectral characteristics. They do bring variations to the group of spectra but do not change the climatological spectrum.

- The Taylor hypothesis is valid for the largest structures in the normal daily time series, as a consequence, the coherence between two points in the range of about 2 km to about 13 km can be expressed as an exponential function of fd/U_0. The smaller structures are less correlated and become uncorrelated at higher fd/U_0. The spectral slope transition from $-5/3$ to -3 is argued to be related to the integral time scale of the local weathers and it is smaller for winter months than the average. This integral time scale is also argued to be an indication for the limit for the validity of the Taylor hypothesis.

Acknowledgment This work is supported by PSO project "Mesoscale", 2007-1-7141 and the ICEWIND project. The second author acknowledges the support from the Danish Council for Independent Research - Technology and Production Sciences (10-093196). We thank Poul Sørensen from Risø

DTU for discussions. The authors acknowledge Dong Energy and Vattenfall for the measurements.

References

[1] K.S. Gage and G.D. Nastrom. Theoretical interpretation of atmospheric wavenumber spectra of wind and temperature observed by commercial aircraft during GASP. *J. Atmos. Sci.*, 43:729–740, 1986.

[2] E. Lindborg. Can the atmospheric kinetic energy spectrum be explained by two-dimensional turbulence? *J. Fluid Mech.*, 388:259–288, 1999.

[3] E. Lindborg, K.K. Tung, G.D.Nastrom, J.Y.N.Cho, and K.S.Gage. Comment on "reinterpreting aircraft measurements in anisotropic scaling turbulence" by Lovejoy et al. 2009. *Atmos. Chem. Phys.*, 10:1401–1402, 2010.

[4] U. Högström, A.-S. Smedman, and H. Bergström. A case study of two-dimensional stratified turbulence. *J. Atmos. Sci.*, 56:959–976, 1999.

[5] C. L. Vincent, P. Pinson, and G. Giebel. Wind fluctuations over the North Sea. *Int. J. Climatol., DOI 10.1002/joc.2175*, 2010.

[6] X.G. Larsén, S. Ott, J. Badger, A. Hahmann, and J. Mann. Recipes for correcting the effect of mesoscale resolution on the estimation of extreme winds. *Journal of applied meteorology and climatology, In press*, 2011.

[7] P. Sørensen, A. D. Hansen, P. André, and C. Rosas. Wind models for simulation of power fluctuations from wind farms. *J. Wind Eng. Ind. Aerodyn.*, 90:1381–1402, 2002.

[8] C. L. Vincent, X. G. Larsén, S.E. Larsen, and P. Sørensen. Cross-spectra over the sea from observation and the WRF model. *Bound. Layer Meteorol. submitted*, 2011.

[9] P.S. Brown and G.D. Robinson. The variance spectrum of tropospheric winds over Eastern Europe. *J. Atmos. Sci.*, 36:270 –286, 1979.

[10] G.D. Nastrom and K.S. Gage. A climatology of atmospheric wavenumber spectra of wind and temperature observed by commercial aircraft. *J. Atmos. Sci*, 42:950–960, 1985.

[11] C.K. Wikle, R.F. Milliff, and W.G. Large. Surface wind variability on spatial scales from 1 to 1000 km observed during TOGA COARE. *J. Atmos. Sci.*, 56:2222–2231, 1999.

[12] J. Y. N. Cho and E. Lindborg. Horizontal velocity structure fluctuations in the upper troposphere and lower stratosphere 1. Observations. *J. Geophy. Res.*, 106:10223–10232, 2001.

[13] K.K. Tung and W.W. Orlando. The k^{-3} and $k^{-5/3}$ energy spectrum of atmospheric turbulence: quasigeostrophic two-level model simulation. *J. Atmos. Sci.*, 60:824–835, 2002.

[14] W.C. Skamarock. Evaluating mesoscale NWP models using kinetic energy spectra. *Monthly Weather Review*, 132:3019–3032, 2004.

[15] K. Hamilton, Y. O. Takahashi, and W. Ohfuchi. Mesoscale spectrum of atmospheric motions investigated in a very fine resolution global general circulation model. *J. Geophy. Res.*, 113:1–19, 2008.

[16] X.G. Larsén, S. Larsen, and M. Badger. A case study of mesoscale spectra of wind and temperature, observed and simulated. *Q. J. R. Meteorol. Soc.*, 137:264–274, 2011.

[17] S. K. Kao and L.L. Wendell. The kinetic energy of the large-scale atmospheric motion in wavenumber-frequency space. I: Northern Hemisphere. *J. Atmos. Sci.*, 40:749–761, 1970.

[18] G.J. Boer and T.G. Shepherd. Large-scale two-dimensional turbulence in the atmosphere. *J. Atmos. Sci.*, 40:164–184, 1983.

[19] D.K. Lilly. Stratified turbulence and the mesoscale variability of the atmosphere. *J. Atmos. Sci*, 40:749–761, 1983.

[20] R.H. Kraichnan. Inertial ranges in two-dimensional turbulence. *Phys. Fluids*, 10:1417–1423, 1967.

[21] G.K. Batchelor. Computation of the energy spectrum in homogeneous two-dimensional turbulence. *High Speed Computing in Fluid Dynamics, Phys. Fluid.*, suppl. II:223–239, 1969.

[22] B. K. Shivamoggi. Direct and inverse cascades in two-dimensional turbulence with a generalized enstrophy invariant. *International journal of theoretical physics*, 39:83–87, 2000.

[23] T.E. van Zandt. A universal spectrum of buoyancy waves in the atmosphere. *Geophys. Res. Lett.*, 9:575–578, 1982.

[24] D.C. Fritts and T.E. van Zandt. Effects of Doppler shifting on the frequency spectra of atmospheric gravity waves. *J. Geophys. Res.*, 92:9723–9732, 1987.

[25] S.A. Smith. Evidence for a saturated spectrum of atmospheric gravity waves. *J. Atmos. Sci*, 44:1404–1410, 1987.

[26] C. Sidi, J. Lefrere, F. Dalaudier, and J. Barat. An improved atmospheric buoyancy wave spectrum model. *J. Geophys. Res.*, 93:774–790, 1988.

[27] W. Schlez and D. Infield. Horizontal, two point coherence for separations greater than the measurement height. *Bound.-Layer Meteorol.*, 87:459–480, 1998.

[28] T. Nanahara, M. Asari, T. Sato, K. Yamaguchi, M. Shibata, and T. Maejima. Smoothing effects of distributed wind turbines. part 1. coherence and smoothing effects at a wind farm. *Wind Energy*, 7:61–74, 2004.

[29] J.W. Woods, R. J. Davy, C. J. Russel, and P.A. Coppin. Cross-spectrum of wind speed for meso-gamma scales in the upper surface layer over south-eastern australia. *Bound. Layer Meteorol.*, 141:93–116, 2011.

[30] A.G. Davenport. The spectrum of horizontal gustiness near the ground in high winds. *Q.J.R.Meteorol. Soc.*, 87:194–211, 1961.

[31] L. Kristensen, H. Panofsky, and S. Smith. lateral coherence of longitudinal wind components in strong winds. *Bound.-Layer Meteorol.*, 21:199–205, 1983.

[32] A.-S. Smedman. Some additional coherence data in the inertial subrange. *J. Climate and Appl. Meteorol.*, 26:1770–1773, 1987.

[33] J. Mann. The spatial structure of neutral atmospheric surface-layer turbulence. *J. Fluid Mech.*, 273:141–168, 1994.

[34] B. Lange, S. Larsen, J. Højstrup, and R. Barthelmie. Importance of thermal effects and sea surface roughness for offshore wind resource assessment. *J. Wind Eng. Ind. Aerodyn.*, 92:959–988, 2004.

[35] C. L. Vincent, A. N. Hahmann, and M. C. Kelly. Idealized WRF simulations of open cellular convection over the sea. *Bound. Layer Meteorol., In press*, 2011.

[36] A. Peña, S. Gryning, and C. B. Hasager. Measurements and modeling of the wind speed profile in the marine atmospheric boundary layer. *Bound. Layer Meteorol.*, 129:479–495, 2008.

[37] S.E. Larsen, M. Courtney, and L. Mahrt. Low frequency behavior of horizontal velocity spectra in stable surface layers. *Nineth Symposium on Turbulence and Diffusion, American Metrorol. Society*, pages 401–404, 1990.

[38] L. Kristensen and P. Kirkegaard. Sampling problems with spectral coherence. Technical Report Risoe-R-526(EN), Risø National Laboratory, Roskilde, Denmark, *URL:www.risoe.dk*, 1986.

[39] L. Kristensen, P. Kirkegaard, and J. Mann. Sampling statistics of atmospheric observations. *Wind Energ.*, 5:301–313, 2002.

[40] S.B. Pope. *Turbulent Flows*. Cambridge University Press, 2000.

[41] X.G. Larsén and J. Mann. The effects of disjunct sampling and averaging time on mean maximum wind. *J. Wind Eng. Ind. Aerodyn*, 94:581–602, 2006.

[42] X.G. Larsén, S. Larsen, and A. N. Hahmann. Origin of waves in "A case study of mesoscale spectra of wind and temperature, observed and simulated":Lee waves from Norweigian mountains. *Q. J. R. Meteorol. Soc., Doi:10.1002/qj.916*, 2011.

[43] B. Brümmer and S. Pohlmann. Wintertime roll and cell convection over greenland and barents sea region: A climatology. *J. Geophys. Res.*, 105:15559 –15566, 2000.

Noname manuscript No.
(will be inserted by the editor)

Cross-spectra over the sea from observations and mesoscale modelling

C L Vincent · X G Larsén · S Larsen · P Sørensen

Received: date / Accepted: date

Abstract Co-spectra and quadrature-spectra are calculated for six pairs of tall offshore measurement masts near the Horns Rev wind farm in the Danish North Sea and the Nysted wind farm in the Baltic sea. The mast-pairs are separated from one another by horizontal distances of 2.13 km to 12.4 km. Co-spectra and quadrature-spectra for the two sites are classified in terms of the angle between the mean wind direction and the line connecting each pair of masts (α). The frequency axes of the spectra are normalized to remove the effect of mean wind speed and separation distance. Results indicate a larger contribution to the quadrature-spectrum for flow from the sea than for flow from the land, and the patterns in the spectra are clearer and better defined for Horns Rev (which has a long uninterrupted sea-fetch from the west) than for Nysted (which is surrounded by a more complicated coast-line).

The analysis is replicated based on 3 month simulations using the weather research and forecasting (WRF) model with a horizontal grid spacing of 2 km. For the sea-fetch directions, good agreement in spectral properties between the model and observations is found. Analytical expressions based on the properties of the cross-correlation function and an exponentially decaying coherence function are fitted to the normalized co- and quadrature-spectra. The expressions are shown to be a good fit to the spectra calculated from the WRF simulations, which suggests that to a good approximation, the average co- and quadrature-spectra over the sea can be written as functions of mean wind speed, separation distance and α.

Keywords Cross-spectrum · Wind speed spectrum · Mesoscale modelling

F. Author
first address
Tel.: +123-45-678910
Fax: +123-45-678910
E-mail: fauthor@example.com

S. Author
second address

1 Introduction

The successful implementation of high levels of wind energy over geographically limited areas such as the North Sea requires consideration of not only the mean wind and spectral properties of the wind at individual wind turbine locations, but depends on the cross-spectral properties of the wind speed at multiple locations within a large wind farm or at multiple neighbouring wind farms. This is because the aggregated power response of a number of turbines under fluctuating wind conditions depends on the extent to which the fluctuations are correlated at individual turbine sites. This issue has been partly accounted for in wind farm power systems models such as those described in Sørensen et al (2002) and Vigueras-Rodrìguez et al (2010). Two different scenarios for the spatial distribution of wind fluctuations are illustrated in figure 1, where pairs of time series from two offshore meteorological masts near the Horns Rev wind farm in the North Sea that are separated by a distance of 12.42 km are shown for 24 hour periods of longitudinal and lateral flow respectively. Here, longitudinal flow refers to flow where the mean wind direction is along the orientation of the two masts, and lateral flow refers to a mean wind direction that is perpendicular to the orientation of the masts. For the longitudinal case, there is an obvious lag between the time series, while for lateral flow case there is no obvious, systematic lag. In addition to the differences caused by the systematic lag, the pairs of time series differ from one another due to the decay or development of eddies over the separation distance. Together, the co-spectrum and the quadrature-spectrum quantify the contribution of in-phase and out-of-phase fluctuations to the overall co-variance between pairs of time series.

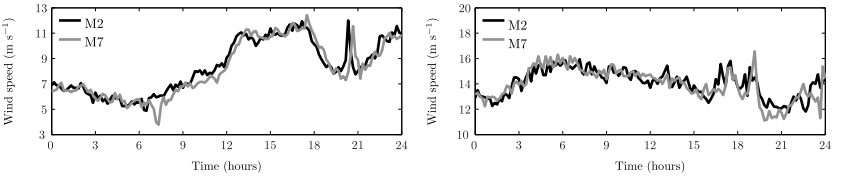

Fig. 1 Examples of pairs of wind speed observations from a two masts near the Horns Rev wind farm in the North Sea, separated by 12.42 km. Right: Longitudinal flow. Left: Lateral flow.

The spectral properties of the wind speed and other atmospheric variables in the mesoscale range have been documented using a variety of data sets and analysis techniques. For example, Gage and Nastrom (1986) used measurements from commercial aircraft to calculate spectra in wave-number space, and established that when plotted on a log-log axes, the zonal and meridional wind components and the temperature followed a spectral slope of $-5/3$ in the mesoscale range.

For length scales dominated by microscale fluctuations, the cross-spectral properties of pairs of wind speed observations have also been studied in detail. For example, Davenport (1961) calculated the coherence for pairs of vertically separated observations, and was the first to express the magnitude of the coherence, γ, as a function of vertical separation distance and mean wind speed.

$$|\gamma| = \frac{|Co_{12}(f) + iQu_{12}(f)|}{\sqrt{(P_1(f)P_2(f)}} = e^{-k\frac{f}{V_0}\Delta z}. \quad (1)$$

where $Co_{12}(f)$ and $Qu_{12}(f)$ are the real and imaginary parts of the cross-spectrum between the two time series, P_1 and P_2 are the power spectra of the two time series, k is a decay constant, Δz is the vertical separation of the two observations and V_0 is a reference velocity near the ground. Kristensen (1979) derived expressions for the longitudinal coherence in the inertial sub-range by considering the loss of coherence due to lateral diffusion and Kristensen and Jensen (1979) presented theoretical and experimental results for the lateral coherence of the lateral and longitudinal wind components. In both cases, the expressions were based on the exponential decay of the coherence, and results were presented as a function of the dimensionless frequency $\frac{fd}{V_0}$, where d was a separation distance between the observations. These results were based on separation distances of a few tens of metres. Schlez and Infield (1998) combined the expressions for lateral and longitudinal coherence to formulate empirical expressions for the coherence as a function of mean wind speed, separation distance and the angle between the mean wind direction and the separation of pairs of masts for separation distances of 62–102 m. The decay factor in their expressions depended on the standard deviation of wind speed for lateral flow, and on standard deviation and mean wind speed for longitudinal flow.

Calculating cross-spectra for longer separation distances up to a few kilometres is, however, more problematic due to the challenges in obtaining suitable pairs of observations, particularly over the sea. Furthermore, for cross-spectra calculated for micro-scales one can easily find segments of time series for which stationarity is a good assumption. In contrast, cross-spectra based on separation distances of several kilometres correspond to time scales on which the atmosphere can rarely be treated as stationary. In Sørensen et al (2002), an expression for exponential decay of coherence was combined with decaying sine and cosine terms to express the complex coherence for separation distances of around 1 km for the purpose of wind energy power production modelling over the sea. Woods et al (2011) built on expressions similar to those of Sørensen et al (2002) to propose models for the co-spectrum and quadrature-spectrum based on an extensive data set of pairs of measurement masts separated by distances of 1–30 km in south-eastern Australia. Their expressions were more complex than those of Sørensen et al (2002) and Schlez and Infield (1998) and include several extra fitted parameters - probably due to the inhomogeneous nature of the data set and the more complex cross-spectral properties of wind speed time series over the land. Larsén et al (2011b) used pairs of tall offshore measurement masts near the Nysted wind farm in the Baltic Sea and Horns

Rev wind farm in the North Sea to study the cross-spectral properties of the wind speed for across-wind conditions and separation distances of 2–12 km. Using a combination of the WRF mesoscale model and measurements, they demonstrated the impact of gravity waves on the shape of cross-spectrum.

In this work, the shapes of the co-spectra and quadrature-spectra over the sea are studied from three different perspectives. Firstly, co-spectra and quadrature-spectra are calculated using data from six offshore measurement masts: three over the North Sea near the Horns Rev wind farm, and three over the Baltic Sea near the Nysted wind farm. The two sets of masts provide six mast-pairs with separation distances ranging from 2.13–12.42 km. All data has a measurement resolution of 10 min, and our time scales of interest are 20 min to 24 hr. Secondly, the analysis of observational data is replicated using mesoscale model simulations, where the analysis focuses on conditions over the sea. Finally, mathematical models similar to those proposed by Sørensen et al (2002) are fitted to the co-spectra and quadrature-spectra from the mesoscale model, and it is implied that over the sea, the average spectra can be expressed as functions of frequency, wind speed, separation distance and angle between the mean wind direction and the orientation of the two sites.

In section 2, the background to the co-spectrum and quadrature-spectrum is briefly outlined, and the formulation of an analytical model based on the Davenport equation and the properties of the complex cross spectrum, as first proposed by Sørensen et al (2002), is described. In sections 3 and 4, the observation data sets and mesoscale model simulations that were used in the analysis are described. In section 5, the co-spectra and quadrature-spectra based on observations and mesoscale modelling are presented, together with the proposed semi-empirical functions that relate the shape of the spectra to the wind direction, separation distance and relative angle of the mean wind to the orientation of the mast-pairs. Discussion and concluding remarks are given in sections 6 and 7 respectively.

2 The co-spectrum and quadrature-spectrum

The co-spectrum and quadrature-spectrum are the real and imaginary parts respectively of the complex cross-spectrum. When normalized by the power spectra of the two input time series, the normalized co-spectrum and the normalized quadrature-spectrum make up the real and imaginary parts of the coherence, Coh, which is often expressed as an absolute value, $\gamma = |Coh|$.

$$\gamma(f) = \frac{|\overline{C_{12}}(f)|}{\sqrt{\overline{P_1(f)P_2(f)}}}, \quad \text{or,} \tag{2}$$

$$\gamma(f) = \frac{|\overline{Co_{12}}(f) + i\overline{Qu_{12}}(f)|}{\sqrt{\overline{P_1(f)P_2(f)}}}, \tag{3}$$

where C_{12} is the complex cross spectrum of two time series, P_1 and P_2 are the power spectra of the time series, and Co_{12} and Qu_{12} are the co-spectrum and quadrature-spectrum. In this paper we work with the normalized co-spectrum and quadrature-spectrum, $\mathrm{Co_n}$ and $\mathrm{Qu_n}$, and the complex coherence, Coh:

$$\mathrm{Co_n}(f) = \frac{\overline{Co_{12}}(f)}{\sqrt{\overline{P_1(f)P_2(f)}}} \tag{4}$$

$$\mathrm{Qu_n}(f) = \frac{\overline{Qu_{12}}(f)}{\sqrt{\overline{P_1(f)P_2(f)}}} \tag{5}$$

$$\mathrm{Coh}(f) = Co_n(f) + i\mathrm{Qu_n}(f) \tag{6}$$

Together, the co-spectrum and the quadrature-spectrum describe the in-phase and out-of-phase contributions to the covariance of the two time series. Time series that are perfectly correlated at a certain frequency have a co-spectrum of one and a quadrature-spectrum of zero at that frequency, while identical time series with a half-cycle phase-shift have a co-spectrum of -1 and a quadrature of zero. Time series that are one quarter cycle out-of-phase have a co-spectrum of zero and a quadrature of ± 1, depending on whether the first time series leads or lags the second.

If the coherence is calculated for a single pair of time series, then it will be identically equal to unity for all frequencies, since $|C_{12}(f)| \equiv |\mathcal{F}_1(f)\mathcal{F}_2^*(f)|$, where $\mathcal{F}$ denotes a Fourier transform, which is identical to the denominator of the coherence. On the other hand, if the numerator and denominator are both calculated and averaged over N segments, then the correct formulation of the coherence is obtained. As discussed by Kristensen and Kirkegaard (1986), this procedure is problematic for many time series from the geophysical time series, since the time series are usually non-stationary and not available for sufficient time periods for the calculation of meaningful averages. This is a particular problem for the analysis of mesoscale coherence, where we generally have no more than 24 hour periods of even near-stationary conditions, and any subdivision of the available time series into shorter segments results in an impractical loss of data at low frequencies. Fortunately, a solution is proposed by Kristensen and Kirkegaard (1986), who shows that the coherence calculated from a block averaged (smoothed) single realization of the spectra and cross-spectra is equivalent to averaging over a large number of time series. Analysis using the two methodologies shows that the resultant co-spectra and quadrature-spectra are relatively insensitive to the choice of analysis methodology, and to the degree of smoothing that is applied in the block averaging.

For pairs of time series with systematic lag between them, such as pairs of wind speed observations separated in the longitudinal direction, the maximum of the cross-covariance function will not be at zero, which introduces a bias into the cross-spectrum (Madsen, 2007). Specifically, it appears as non-zero values in the quadrature-spectrum. Removing the lag by adjusting the time series for the effect of advection means that the quadrature will be near-zero

for most frequencies. On the other hand, apparently systematic phase differences between pairs meteorological time series are never likely to be as simple as pure advection between the two sites. On time scales such as the diurnal or semi-diurnal cycles, a pair of time series from masts separated by tens of kilometres are expected to be perfectly in phase, while we expect a transition to time scales that are dominated by advection for time scales of several hours. Furthermore, advection is not the only physical process responsible for the movement of mesoscale features, as evident by the steering of convective systems by wind well above the surface (eg. Sioutas and Flocas (1996)), anomalous propagation of severe thunderstorms (eg. Davies-Jones (2002)) or gravity waves (Larsén et al, 2011a). For these reasons, we choose not to correct the lag in the pairs of wind speed time series that are analyzed here.

Sørensen et al (2002) proposes writing the cross-spectrum as:

$$C(f) = \gamma\sqrt{P_1(f)P_2(f)}e^{2\pi f\tau_{12}i} \tag{7}$$

where γ is the magnitude of the coherence, f is the frequency and τ_{12} is the delay time, which we assume is dominated by advection and is therefore constant. The normalized complex cross spectrum (Coh) can then be written as:

$$Coh(f) = \gamma e^{2\pi f\tau_{12}i} \tag{8}$$

Following the format of Davenport (1961), the magnitude of Coh can be expressed in the form $e^{a\frac{fd}{V_0}}$, where d is a separation distance, f is the frequency, a is a constant and V_0 is the mean wind speed, so the complex coherence becomes

$$Coh(f) = e^{(adf/V_0)}e^{-2\pi f\tau_{12}i}. \tag{9}$$

By consideration of advection between the two points, the delay time can be written as

$$\tau_{12} = \frac{dcos(\alpha)}{V_0}, \tag{10}$$

where α is the angle between the mean wind speed and the line connecting the two points and $dcos(\alpha)$ is the separation distance along the mean wind direction. Combining equations 9 and 10 gives

$$Coh(f) = e^{(-adf/V_0)}e^{-2\pi f\frac{cos(\alpha)d}{V_0}i} \tag{11}$$

Equation 11 can then be simplified by defining a dimensionless frequency, $n = \frac{fd}{V_0}$, adjusts for the differences in the spectra due purely to different rates of advection between the two masts. Using the normalized frequency, equation 11 can be rewritten as

$$Coh(n) = e^{an}e^{bni}, \tag{12}$$

where a is an unknown constant and $b = -2\pi cos(\alpha)$.

Taking the logarithm of both sides, and equating real and imaginary parts shows that the constants a and b can be found empirically from the slope of the real and imaginary parts respectively of the log of the complex coherence.

$$\log(Coh(n)) = an + bni. \tag{13}$$

$$\begin{aligned} \Re(\log(Coh(n))) &= an \\ \Im(\log(Coh(n))) &= bn \end{aligned} \tag{14}$$

The normalized co- and quadrature- spectra are then written as:

$$\begin{aligned} \mathrm{Co_n} &= e^{an} cos(bn) \\ \mathrm{Qu_n} &= e^{an} sin(bn) \end{aligned} \tag{15}$$

In section 5.3 of this paper, the parametrization in equation 14 are used to fit curves to the co-spectrum and quadrature-spectrum calculated from WRF simulations. It is shown that the parameters a and b both vary sinusoidally with the angle α, allowing $\mathrm{Co_n}$ and $\mathrm{Co_n}$ to be written as functions of α, separation distance d and mean wind speed V_0.

3 Observation data

The calculation of mesoscale co-spectra and quadrature-spectra over the sea requires pairs of observations from offshore measurement masts separated by distances of several kilometres up to tens of kilometres. The offshore measurement masts that were installed in association with the Horns Rev I and Nysted offshore wind farms satisfy these requirements, and provide a unique opportunity for calculating mesoscale co-spectra and quadrature-spectra. Each site has three tall measurement masts that were continuously collecting observations during the early stages of the wind farms' operations. The masts provide three mast-pairs for each site, separated by varying distances and aligned along various orientations, as summarized in Table 1. Measurements of wind speed and direction were available at several heights for each mast. Here, we focus on the top-mounted wind speed observations, thereby avoiding difficulties associated with boom distortion at the lower levels.

Although the masts are offshore, the flow was influenced by the wake of the nearby land as well as the wind farm wakes. In figure 2, the positions of the masts in relation to the turbines is shown for both wind farms. The undisturbed flow from the sea is indicated for each mast.

Table 1 Mast pairs at the Horns Rev and Nysted wind farms. The orientation refers to the wind direction that would blow from the first to the second mast in the pair.

Mast	Separation distance (km)	Orientation	Measurement period	Height (m)
Horns Rev M2-M6	8.72	295°	2003–2006	62
Horns Rev M2-M7	12.42	287°	2003–2006	70
Horns Rev M6-M7	3.99	269°	2003–2006	70
Nysted M1-M2	2.13	343°	2004–2008	65
Nysted M2-M3	8.90	280°	2004–2008	65
Nysted M1-M3	8.18	273°	2004–2008	65

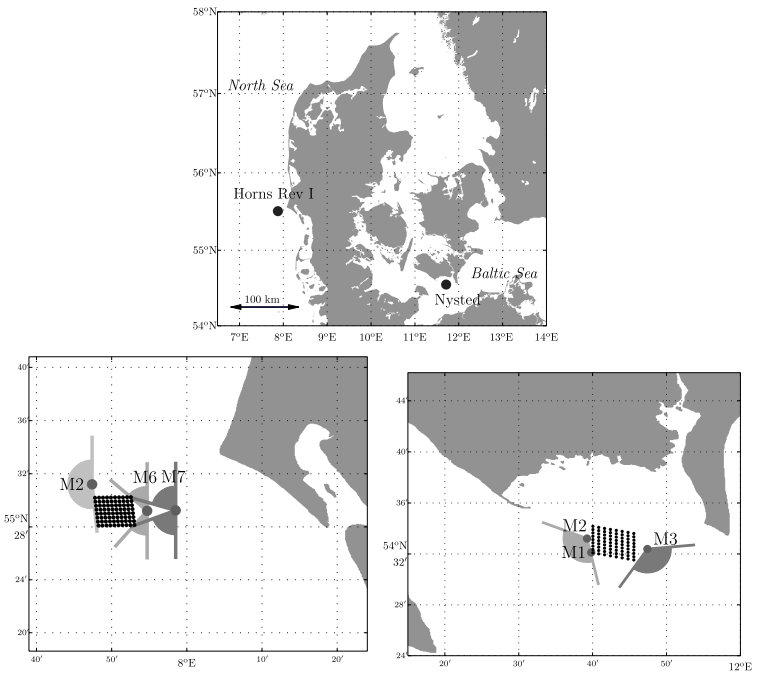

Fig. 2 The locations of the Horns Rev I and Nysted wind farms (upper plot), and the meteorological masts at the two sites (lower plots). The undisturbed flow sectors for the two sites are indicated by the shaded arcs.

For calculation of co-spectra and quadrature-spectra from the sea, it is preferable that both masts and all points on the line connecting them are free from wake and land effects. This restrictive condition means that it is necessary to discard most of the data, and in particular it becomes impossible to calculate spectra for longitudinal flow between the masts due to the position of the turbines between the masts. Therefore, these condition have been relaxed, and all directions have been included in the analysis. The wake-influenced and land-influenced direction sectors have been clearly indicated. In fact, the wind

farm wake may not actually influence the spectra on the time scales that we are interested in, since Larsen et al (2009) has shown that the wind speed in the wake of an 80-m diameter turbine rotor contains enhanced variance only for frequencies greater than about 0.004 Hz.

Pairs of time series were analyzed in 24 hour segments, each consisting of 144 ten minute observations. Due to missing data and large changes in meteorological conditions during some periods, it was necessary to reject many of the 24 hour segments. Although meteorological time series are never strictly stationary, a compromise between including sufficient data in the analysis and choosing the best possible time series for the analysis was sought. The following segments were therefore rejected from the analysis: segments where more than one observation was missing from either of the two time series, segments where the average wind direction at the two sites differed by more than 15 degrees or the average wind speed differed by more than 2 m s^{-1}, segments where the range of wind directions was greater than 90 degrees and segments where the range of wind speeds was more than 12 m s^{-1}. After applying these criteria, 364, 371 and 476 segments remained for the mast pairs M2-M6, M2-M7 and M6-M7 at Horns Rev respectively, and 305, 325 and 274 segments remained for the mast pairs M1-M2, M2-M3 and M1-M3 at Nysted respectively. These segments include both undisturbed flow from the sea, and land-influenced and wake-influenced flow.

4 Mesoscale simulations

For each region, a 90 day period was simulated using the WRF mesoscale mesoscale model Version 3.3 (Skamarock et al, 2008). For the North Sea, the simulation covered the months October–December 2004, while for the Baltic Sea, the simulation covered the months October–December 2006. The periods were chosen to match with data availability for verification purposes, but since we deal with average spectra, the precise time periods of the model runs are not compared with the equivalent time periods in observational data anyway. The months October–December are chosen to cover a range of atmospheric conditions, including the cold air-outbreak situations that are found during these months, and which are expected to be important for mesoscale coherence due to the organized boundary structures such as convective rolls or cellular convection.

The three-month simulation periods are in contrast to the observational time series of several years, and have the disadvantage that they do not represent a long enough time period to be considered as a climatological average. On the other hand, Larsén et al (2011b) suggests that average spectra in the range 10^{-5}–10^{-3} Hz are not particularly sensitive to the seasonal or yearly scales, although the relative occurrence of mesoscale phenomena at certain times of year could effect the analysis. Furthermore, the mesoscale model has the advantage that we are not restricted to using only the three fixed observational sites. Due to the gridded nature of the model output, it is always

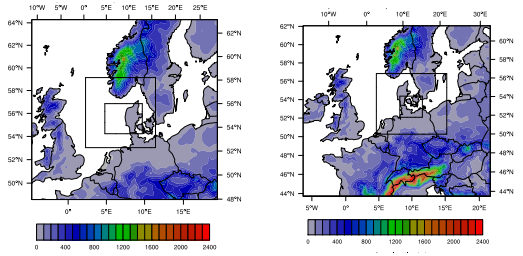

Fig. 3 WRF simulation domains. *Left* Domain for simulations over North Sea. *Right* Domains for simulations over Baltic Sea

possible to find a pair of points for which are almost upwind of one another, or a pair that are aligned in an almost cross-wind direction. This means that it is possible to use every 24 hour period that satisfies the basic stationarity criteria described in section 3 for the observational data for any direction of interest, so no additional subdivision into direction sectors was necessary. After applying the stationarity criteria, 36 days remained for the North Sea, and 60 days remained for the Baltic Sea.

The WRF simulations used NCEP CFSR data for initial and boundary conditions. Simulations ran in blocks of 11 days, with the first 24 hours discarded for spin-up purposes. Nudging was applied to the outer domain to keep the simulations true to the realistic evolution of the large scale weather. Three nests with horizontal grid spacings of 18km, 6km and 2km respectively were used. The model had 37 vertical levels, with the lowest five positioned close to 14 m, 52 m, 103 m, 160 m and 224 m respectively. The simulation domains are shown in figure 3.

The boundary layer parametrization was the MYNN scheme (Nakanishi and Niino, 2009), and the larger two domains used the Kain-Fritsch cumulus parametrization (Kain and Fritsch, 1990), while for the smallest domains the cumulus parametrization was turned off. It is expected that for a horizontal grid spacing of less than about 5 km, the effect of cumulus convection will be at least partly resolved (Molinari and Dudek, 1992), and we expect that explicit cumulus processes could make a significant contribution to mesoscale fluctuations and their spatial correlation.

For calculation of cross-spectra equivalent to those that were calculated from the observational data, the wind speed for the lowest five model levels was saved every 10 minutes. The observed and modelled wind speed at Horns Rev for the three-month simulation period is shown in figure 4, where the observations are from a height of 70 m (M7) and the model output is from the third model level at about 103 m. Figure 4 shows that the model accurately reproduces the slow variation in wind speed. To assess whether the fast variations in wind speed are modelled correctly, the spectra of the modelled time series are compared with the observed spectra for the three meteorological masts at Horns Rev in figure 5. The spectral slope is well modelled up to the highest resolvable time period of 20 minutes. Both the observations and the

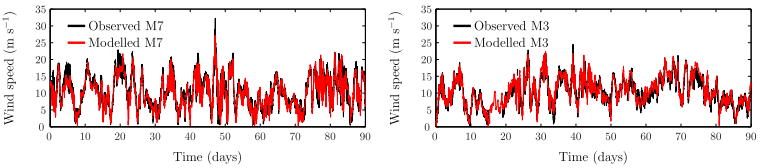

Fig. 4 Observed and modelled wind speed at Horns Rev M7 for the 90 day climate run. The observed time series is from a height of 70 m, and the model time series is from a height close to 103 m.

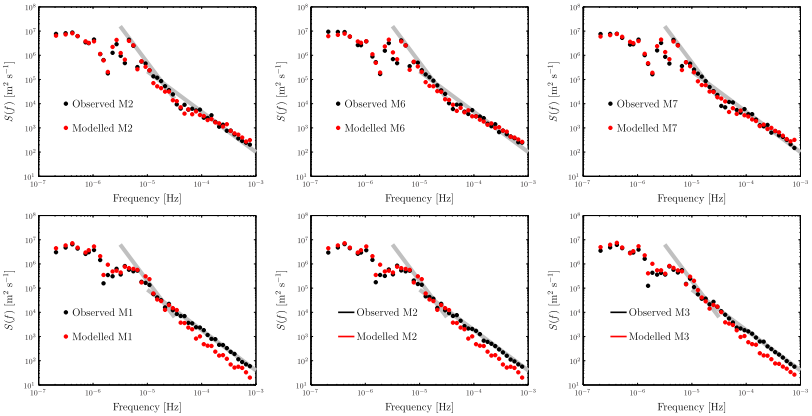

Fig. 5 Observed and modelled spectra of wind speed at Horns Rev M2, M6 and M7 respectively for the 90 day climate run. The observations are at a height of 62 m for M2 and 70 m for M6 and M7. The modelled wind speeds are from the third model level at a height of about 103 m. The thick grey lines indicate a spectral slope of -3 (periods greater than 24 hours) and $-5/3$ (periods less than 24 hours).

model spectra follow a spectral slope of -3 for time scales longer than about 24 hours, and a spectral slope close to $-5/3$ for shorter time scales, following the observational evidence of Nastrom and Gage (1985).

5 Results

As discussed in section 2, it is possible to normalize the frequency axis of the co-spectra and quadrature-spectra by $\frac{V_0}{d}$, where V_0 is the mean wind speed and d is the separation distance, to give a non-dimensional frequency. The normalization of the frequency axis for longitudinal flow from the sea for the three pairs of meteorological masts at Horns Rev is demonstrated in figure 6 for the original and the normalized frequency axis. It is seen that the normalization causes the spectra to collapse onto a single curve, thereby removing the impact of wind speed and separation distance. The normalized frequency will be used for subsequent spectra in this paper.

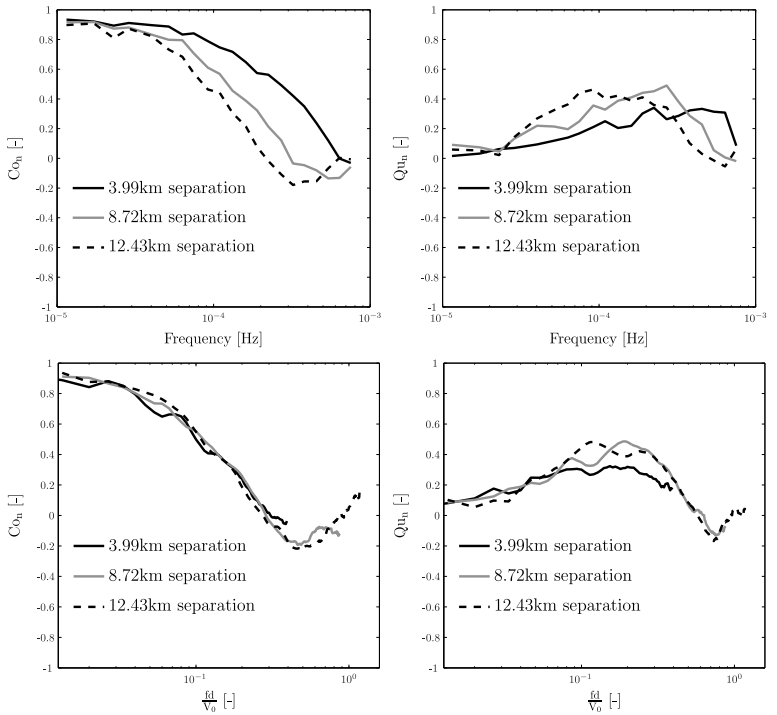

Fig. 6 Co-spectra (left) and quadrature-spectra (right) of wind speed as a function of frequency (upper panels) and normalized frequency (lower panels) for the three mast-pairs at Horns Rev for longitudinal flow from the sea.

5.1 Observed co-spectra and quadrature-spectra as functions of α

The 24 hour segments that satisfied the stationarity criteria were grouped into 8 direction bins according to the mean wind direction during the segment. Since the cases had already been selected on the basis that the range of wind directions was not more than 90°, the average wind direction was sufficient to further classify the cases. The direction bins each had width 45°, and were defined with respect to the direction of the line separating the two masts such that the angle α was 0°, 45°, 90°, 135°, 180°, 225°, 270° and 315° at the centre of each bin respectively. This means that the first and fifth bins are both cases where the separation of the masts is in the longitudinal direction, but in opposite directions. Similarly the third and seventh bins are both cases where the separation of the masts is in the lateral direction. The number of cases in the bins ranged between 9 cases and 89 cases for Horns Rev and between 9 and 92 cases for Nysted. 9 cases is not large enough to form a representative sample, but all bins are retained for completeness.

Figure 7 shows the co- and qu- spectra for the eight direction sectors for Horns Rev M2 and M7 (separated by 12.43 km) and Nysted M1 and M3

(separated by 8.13 km). It is important to realise that the directions labelled on the graphs are α (the angle between the wind direction and the separation of the masts), not the mean wind direction. Due to the orientation of the masts in a nearly east-west direction at Horns Rev, $\alpha = 0^{\circ}$ corresponds nearly to easterly wind directions and $\alpha = 180^{\circ}$ corresponds nearly to westerly wind directions. Most direction sectors are influenced by the wind farm wake, the land or both. In this analysis, all directions have been included, but the only sector that is completely uninfluenced by the land or the wake is $\alpha = 45^{\circ}$. At Nysted, $\alpha = 90^{\circ}$ corresponds nearly to northerly flow from the land, while $\alpha = 270^{\circ}$ nearly to southerly flow from the sea. All directions will be influenced by wind farm wake or the land or both.

The co-spectrum is similar for each of the 8 direction bins, while the quadrature-spectrum is strongly dependent on α. For the along-wind cases, where there will be a maximum lag or lead between the two time series as a result of advection between the masts, the quadrature-spectra reaches a peak of around 0.4 for the westerly direction and -0.3 for the easterly direction at Horns Rev. The difference in the quadrature-spectra for the two along-wind directions may reflect the fact that the Horns Rev wind farm is only around 11 km from the coast in the easterly direction, so that the flow will be strongly influenced by the land.

At Nysted, the quadrature-spectrum has a peak of around 0.4 for the westerly sector at Nysted, but does not follow any obvious pattern for the easterly sector. This may reflect an effect of the coast line, the fact that there are only 17 cases for this sector, or the different meteorological conditions over the Baltic Sea as compared with the North Sea. Similarly, the co-spectrum dips further below zero to -0.22 at Horns Rev for longitudinal flow from the sea, while the Nysted spectra appear to level off to zero for all direction sectors for normalized frequencies greater than 0.25.

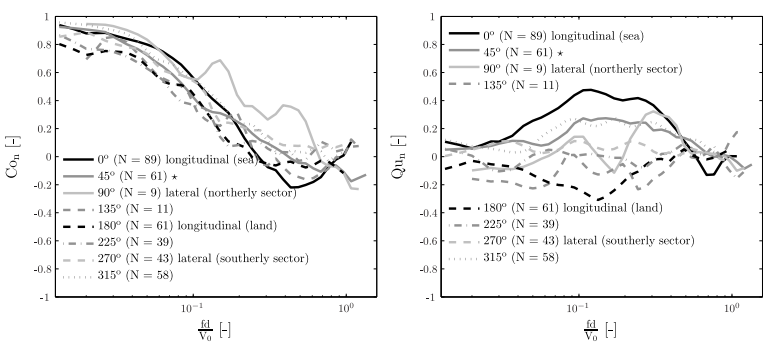

Fig. 7 Normalized co-spectra (left) and quadrature-spectra (right) of wind speed for 8 different direction sectors for the M2–M7 pair at Horns Rev. The separation distances is 12.43 km. The star indicates the only direction sector that is completely free from the influence of the wind farm wake or the land. The number of 24-hour periods included in each direction sector is indicated in brackets in the figure legends.

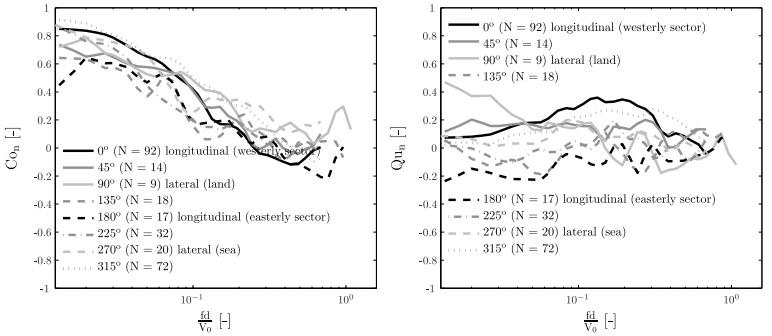

Fig. 8 Normalized co-spectra (left) and quadrature-spectra (right) of wind speed for 8 different direction sectors for the M1–M3 pair at Nysted. The separation distances is 8.18 km. The number of 24-hour periods included in each direction sector is indicated in brackets in the figure legends.

5.2 Normalized co-spectra and quadrature-spectra from WRF as functions of α

Calculation of co- and quadrature-spectra from observations is complicated by the difficulties of data availability. For any direction of interest, there will only be a handful of 24 hour periods where the wind direction stays within a satisfactorily small range of the target direction. To gain enough data for analysis, we are inevitably pushed to relax the conditions of stationarity and to consider a relatively wide window of wind directions.

Mesoscale modelling can alleviate some of these problems, because for any wind direction, it is easy to choose grid points that correspond to a given α and separation distance. Therefore, any 24 hour periods that satisfy the stationarity criteria can be used to study any number of wind directions and separation distances. On the other hand, mesoscale modelling is limited its coarse resolution. Amongst other things, the parametrized vertical mixing in the boundary layer and the absence of explicit turbulent fluctuations and entrainment at the top of the boundary layer make it impossible to use mesoscale modelling to study micro-scale processes in the atmosphere. In this paper, however, we are concerned with cross-spectra for separation distances of several km. As demonstrated by Skamarock (2004), the WRF mesoscale model begins to lose spectral power for scales smaller than about 6-7 times the horizontal grid spacing of the model. This agrees with the model results with horizontal resolution of 2 km in figure 5, which show excellent agreement between the observations and model up to the time scale of 20 min, which for an average wind speed of around 10 m s^{-1} corresponds to a spatial scale of around 12 km. This suggests that it is indeed reasonable to use a model with a horizontal resolution of 2 km to study co- and cross-spectra for separation distances longer than about 12 km.

After discarding the 24-hour periods from the 90 day simulation period that did not satisfy the stationarity criteria described in section 3, there were

36 and 60 days available for each direction sector for the North Sea and the Baltic Sea respectively. A reference point was chosen in each of the two domains, and for each 24-hour period, the grid-points corresponding to an angle α and separation distance d were chosen in relation to the reference point. The procedure is illustrated in figure 9, where the subset of domain 3 grid-points used for the analysis are shown as small grey dots. The large grey dot is the reference point, the mean wind speed is indicated by an arrow, the grid-points chosen for α=0°, 90°, 180° and 270° are indicated by the four symbols surrounding the reference point. The choice of grid-points corresponding to different values of α is dependent on the wind direction, and changes with each 24 hour period.

Unlike the co- and quadrature-spectra calculated from observations, which were a mixture of easterly sector wind directions influenced by the nearby land, and westerly sector wind directions influenced by the sea, the WRF reference points were located slightly further out into the water so that both points had at least 10 km of sea fetch. Furthermore, we do not link a particular value of α with a particular wind direction, since the choice of grid points relating to a particular value of α varies as the mean wind direction varies. Therefore, we are less likely to see systematic effects of the land or climatologically preferred weather regimes for certain values of α than we were for the observed spectra.

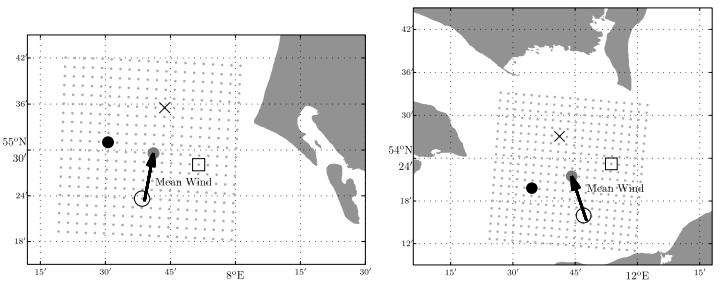

Fig. 9 The subset of domain 3 points used for the analysis (small grey dots). *Right*: North Sea near the Horns Rev wind farm *Left*: Baltic Sea near the Nysted wind farm. The large grey dot is the reference point, and the black arrow indicates mean wind direction. The grid points chosen for $\alpha = 0°$, 90°, 180° and 270° are indicated by the symbols open circle, closed circle, cross and square respectively.

The co- and quadrature-spectra calculated from the WRF simulations are shown in figure 10, based on a 12 km separation distance between the pairs of points. The spectra show many features in common with the corresponding spectra from observations. The co-spectra are not strongly dependent on α, while the quadrature-spectra are close to zero for across-wind cases and reach the maximum amplitude for the along wind cases.

However, there are some important differences between the observed and modelled spectra. Firstly, there is a greater dip below the zero axis for the two along wind directions for normalized frequencies higher than 0.25 for the

model spectra than the observed spectra. Secondly, the model quadrature-spectra are nearly symmetrical about the horizontal axis for supplementary values of α, while the observed quadrature-spectrum has a larger amplitude (0.42) for $\alpha = 0^o$ than $\alpha = 180^o$ (0.3).

These two differences are almost certainly due to two factors. Firstly, the spectra based on the WRF simulation use data points well away from the coast line, and particular values of α are not consistently connected with a certain wind direction. In contrast, the observed spectra with $\alpha = 0^o$ relate to flow from the sea, while the observed spectra with $\alpha = 180^o$ represent flow mainly from the land. To obtain systematic in-phase or out-of-phase fluctuations at two points separated by 12 km probably requires that the wind speed is not significantly altered by flow over topography or other surface inhomogeneities found over the land. Secondly, the model does not contain sub-mesoscale dynamics which could add an extra layer of complexity to the flow. These simpler dynamics might mean that the systematic mesoscale fluctuations are less likely to be broken up, making patterns in the co- and quadrature-spectra easier to interpret.

The clearer patterns in the spectra from the mesoscale simulation allow an obvious interpretation of the positions of the local extrema and zero crossings. At very low normalized frequencies, the two time series are perfectly in phase, since they are both governed by exactly the same large scale and diurnal forcing. Clearly, the normalized co-spectrum must start at 1, and the quadrature-spectrum must start at 0. For the frequency associated with eddies of size four times the separation distance, then the time series at the two points are 90^o out of phase. In this case, the period of the fluctuations is $\frac{4d}{V_0}$, and the normalized frequency is 1/4. For time series that are 90^oout of phase, the quadrature-spectrum is at its maximum value and the co-spectrum is exactly equal to zero. This is clearly seen on the plots - the extrema in the quadrature-spectra match with the zero crossing in the co-spectrum for a normalized frequency of 1/4. By similar reasoning, the minimum in the along wind co-spectra match with the zero crossing in the quadrature-spectrum for a normalized frequency of 1/2, the the extrema in the along-wind quadrature-spectra match with the final zero crossing in the co-spectra for a normalized frequency of 3/4.

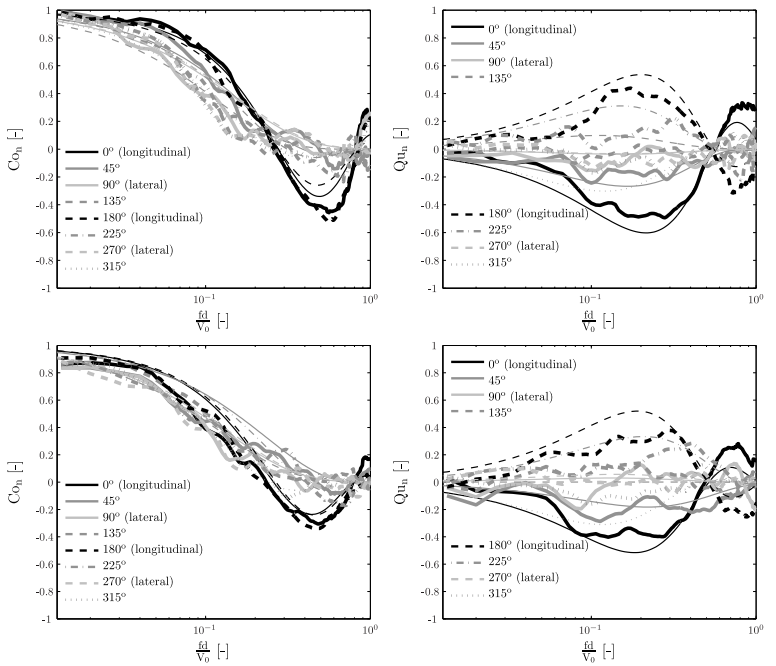

Fig. 10 Normalized co-spectra (*left*) and quadrature-spectra (*right*) for wind speed for 8 different values of α based on WRF simulations over the North Sea (*top*) and the Baltic Sea (*bottom*). The separation distance is 12 km. Thick lines: Spectra calculated from WRF simulations. Thin lines: Fitted spectra using equations 14 and 15.

5.3 Mathematical models for the normalized co- and quadrature-spectra

In equation 15, it was shown that the co- and quadrature-spectra could be expressed as functions of the normalized frequency and two fitted parameters a and b. Furthermore, it was shown that the two parameters could be determined from the slope of the real and imaginary parts of the complex coherence when plotted against the normalized frequency.

11 shows the parameters a and b as a function of the angle α, for separation distances from 12–18 km, which suggets that both parameters vary with α but are invariant to separation distance. Both parameters can be modelled by sinusoidal functions, which means that the co- and quadrature-spectra can be expressed as functions of only α and the normalized frequency, or alternatively as functions of α, wind speed, separation distance and frequency. The solid line shows a sinusoidal fit to the data for the parameter a. For parameter b, it was found that the theoretically derived $2\pi cos(\alpha)$ gave an excellent fit.

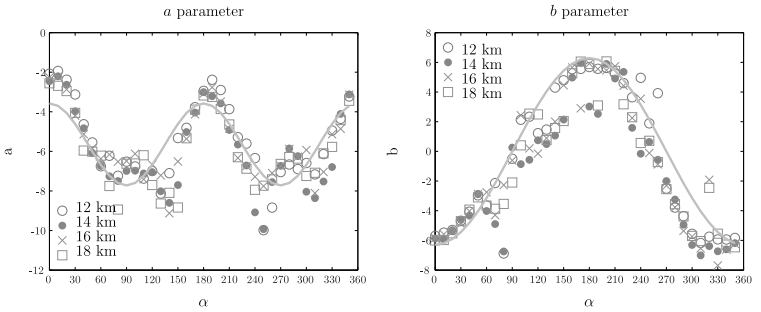

Fig. 11 a and b parameters as a function of α for wind speed.

Based on the fitted curves, the two parameters have the forms:

$$a(\alpha) = 1.8cos(\frac{2\pi\alpha}{180}) - 5.9 \tag{16}$$

$$b(\alpha) = 2\pi cos(\frac{\pi\alpha}{180}) \tag{17}$$

and

$$\mathrm{Co_n}(\alpha, d, V_0, f) = e^{a(\alpha)\frac{fd}{V_0}} cos(b(\alpha)\frac{fd}{V_0}) \tag{18}$$

$$\mathrm{Qu_n}(\alpha, d, V_0, f) = e^{a(\alpha)\frac{fd}{V_0}} sin(b(\alpha)\frac{fd}{V_0}) \tag{19}$$

In other words, if the wind direction and wind speed are known for a pair of points separated by a distance d, then the co- and quadrature- spectra can be estimated. The behaviour of the functions are demonstrated in figure 12, where α, d and V_0 are systematically varied.

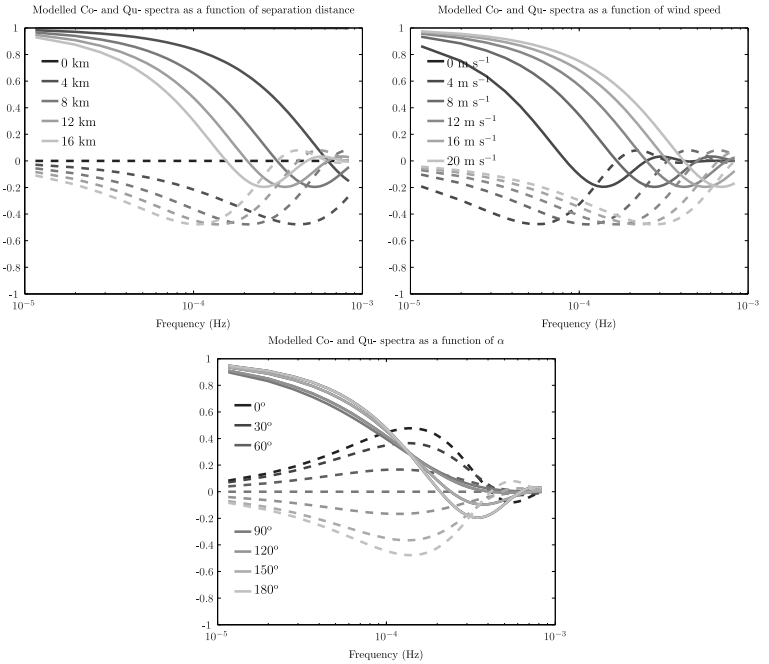

Fig. 12 Top left: Normalized co- and quadrature- spectra as a function of separation distance for constant wind speed (12 m s^{-1}) and α (0 degrees). Top right: Normalized co- and quadrature- spectra as a function of wind speed for constant separation distance (10 km) and α (0 degrees). Bottom: Normalized co- and qu- spectra as a function of α for constant wind speed (12 m s^{-1}) and separation distance (10 km).

Finally, the analytical models in equations 18 and 19 are fitted to two examples of observed flow from the sea for Horns Rev and Nysted respectively. We choose conditions that are well represented in the data, and which are indicative of flow from the sea. The conditions for selection of the data, and the parameters used in equations 18 and 19 are described in table **??**.

Table 2 Example conditions of flow from the sea for chosen for illustrating the models proposed in equations 18 and 19

Mast	α_{obs}	$V_{0,\mathrm{obs}}$ m s^{-1}	α_{model}	$V_{0,\mathrm{model}}$ m s^{-1}	d_{model} m
Horns Rev M2-M7	$> 337.5^o$, $< 22.5^o$	7–9	0^o	8	12420
Nysted M2-M3	$> 337.5^o$, $< 22.5^o$	7–9	0^o	8	8920

Figure 13 shows the modelled and observed spectra for the two sets of conditions described in Table 2. Both of the cases are representative of conditions over the sea, where the analytical model performs well. For flow that is more

influenced by the land than the sea, the analytical models do not perform as well, and we expect that for conditions over land, the spectra are more difficult to relate to the simple advection and exponential decay terms that were used in deriving equations 18 and 19.

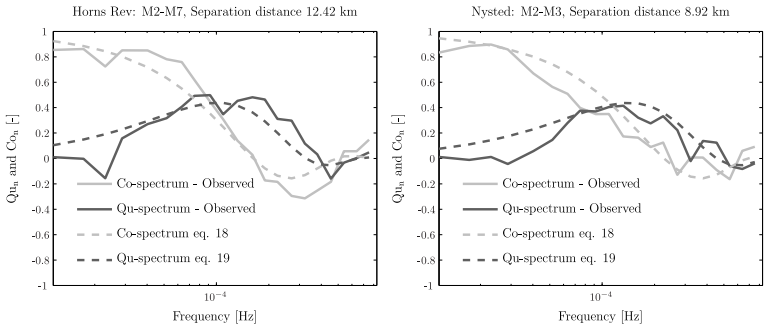

Fig. 13 Normalized co-spectra and quadrature-spectra calculated from observations (solid lines) and from analytical models in equations 18 and 19 for the conditions described in table 2.

6 Discussion

The shapes of the co-spectra and quadrature-spectra for Horns Rev and Nysted show the expected patterns with respect to the relative angle between the wind speed and the separation of the mast-pairs. For lateral flow, where there should not be any systematic phase shift in the wind speed at two sites, the quadrature-spectrum is close to zero for all frequencies, while the co-spectrum decreases exponentially. In this case, the co-spectrum is equal to the coherence. For longitudinal flow, there is a systematic phase shift in the wind speed at the two sites. This is reflected in the peak in the quadrature-spectrum and a zero-crossing in the co-spectrum, both of which occur at a normalized frequency close to 0.25. The normalized frequency of 0.25 corresponds to eddies or structures that have a length scale 4 times the separation distance, which will bring about a phase shift of 90°. Similarly, the co-spectrum reaches a local minimum and the quadrature-spectrum crosses the frequency axis at a normalized frequency of about 0.5, which corresponds to eddies or structures with a length scale of twice the separation distance. Such structures will result in a phase shift of 180° between the two sites. Thus it can be seen that the co-spectra and quadrature-spectra that are illustrated in this paper for time scales between 24 hours and 20 minutes form a pair of exponentially damped cosine and sine functions. The eddies or boundary layer structures corresponding to each frequency continue to cause in-phase or out-of-phase fluctuations at pairs of sites as the frequency increases, depending on the ratio between the length scale of the eddies and the distance between the sites. At the same time, as the eddies get smaller in relation to the distance between the sites, they are

more likely to have undergone changes in their size or amplitude as they are advected between the sites, which causes the overall coherence to decrease.

There was general agreement in the shape of the co-spectrum and quadrature-spectrum for Horns Rev and Nysted, but there were some important differences. At Nysted, the quadrature-spectrum has the characteristic peak at a normalized frequency of 0.25 only for the longitudinal westerly case, and does not show any peak at all for the longitudinal easterly case, and the magnitude of the quadrature spectrum is larger at Horns Rev than at Nysted. Similarly, the co-spectra decrease to zero as expected for normalized frequencies of about 0.25, but do not pass far below the zero axis. As illustrated in figure 2, the coastline surrounding the Nysted wind farm in the Baltic Sea is complex and there are few wind directions from which it has a long, interrupted sea fetch in the way that the Horns Rev wind farm does in westerly flow. Furthermore, less data was available for Nysted, implying that the spectra are less representative. This also effects the spectra calculated from the WRF simulation over the Baltic Sea - even though the grid points have been shifted southwards to avoid the land itself, the region is surrounded by coastlines. Finally, it is well established that different meteorological conditions exist over the North Sea and the Baltic Sea (Larsén et al, 2011b), and some of the differences may be attributable to the set of boundary layer phenomena that dominate the near-surface wind fields over the two seas.

In the WRF model output, the patterns in the co-spectra and quadrature-spectra are somewhat better defined and easier to relate to the simplistic conceptual model of eddies of various sizes being advected past the pair of sites while simultaneously decaying or deforming. For example, the longitudinal co-spectra from the model output dip further below zero than the observed longitudinal co-spectra. Furthermore, the quadrature spectra are nearly symmetrical about the horizontal axis for supplementary pairs of angles for the model spectra, while the peak in the observed quadrature spectrum is larger for flow from the sea than for flow from the land. There are several reasons for these differences. First, the model spectra are based on data that are further away from the land than the observed data, which means that the model spectra are less influenced by surface inhomogeneities. Secondly, the model is simpler than the real world, since there are no sub-grid scale processes. Real-world phenomena such as rain showers from individual cumulus clouds, entrainment at the top of the boundary layer and turbulent eddies do not exist in the model, and it therefore seems more likely that mesoscale eddies that have length scales of tens of kilometres could be advected between the masts relatively undisturbed.

The expressions in equations 18 and 19 were shown to be an excellent fit to the spectra from the WRF model output, which are representative of conditions over the sea. The expressions were also shown to be a good fit for the observed spectra from both Horns Rev and Nysted for selected cases where the wind was blowing from the sea with a relatively uninterrupted sea fetch. The additional input of the mesoscale model thus made it possible to extend the limited observational evidence to derive useful expressions for the shape

of the co-spectrum and quadrature-spectrum over the sea, and to describe the underlying physics behind the shape of the spectra. Although the prohibitive computational costs of mesoscale models are often cited as problematic for such work, we found physically reasonable and robust results using wind speeds saved every 10 minutes from simulations of length 3 months, run at a horizontal grid spacing of 2 km. The results suggest that mesoscale models could be used for conducting similar studies over land, although un-resolved sub-grid-scale topographic effects might have serious consequences at some sites.

The calculation of co-spectra and quadrature spectra is also a useful model verification tool, since it is insensitive to errors in the phase of high frequency fluctuations in the model with respect to the observed fluctuations, which are not possible to forecast in a deterministic sense. Instead, it addresses the amplitude of the fluctuations, and in the case of the cross-spectrum, the spatial patterns in fluctuations. This avoids the typical problems associated with the verification of mesoscale models, where a smooth model with no mesoscale fluctuations at all will actually perform better than a model with spectrally correct but out-of-phase mesoscale fluctuations on scores such as the root mean square error and bias (Mass et al, 2002). The results presented here show good agreement between modelled and observed spectra for time scales up to 20 minutes, and spatial scales up to 12 km. On the other hand, the precise spectral performance of the model in terms of modelling the spatial covariance during special meteorological conditions or topographically driven phenomena depends on whether the model is able to accurately reproduce the physical processes associated with the conditions, and this is an open area for further investigation.

The results presented here are climatological averages that include several years of observations, or 3 months of model data. Obviously many and varied physical processes are contained within the reasonable stationary and homogeneous situations that were identified according to the stationarity criteria. The general spectral shapes that were calculated therefore incorporate various dynamic and convective processes for unstable conditions, and turbulence and gravity wave processes for stable conditions. For example, a preliminary study of the co-spectrum and quadrature-spectrum for 24 hour periods where cellular convection was observed over the North Sea appear to show both a larger peak in the quadrature-spectrum and a deeper trough below zero in the co-spectrum than cases where cellular convection was not observed. In stable conditions, gravity waves affect the spectral properties of the wind speed, as demonstrated in Larsén et al (2011a,b). The shape of the spectra under specific meteorological conditions is an important area for further study, although finding sufficient data from pairs of tall masts under a narrowly defined set of conditions will always make this difficult. Furthermore, by filtering out cases where where was a large wind speed or direction change, a large number of situations that are of great scientific and practical interest have actually been excluded from the analysis. In particular, large changes in wind speed (often referred to as 'ramp events' in a wind energy context **?**) and the way they prop-

agate through wind farms or groups of wind farms are of obvious relevance to wind energy control and integration.

The analysis presented here focuses on the scalar wind speed, despite the fact that cross-spectral analysis of wind time series on microscales is traditionally separated into U (along wind) and V (across wind) components (eg. Kristensen (1979); Kristensen and Jensen (1979)). The decomposition into U and V components is considerably more difficult for mesoscale time scales (tens of minutes to tens of hours), where great care needs to be taken in defining and applying a mean wind direction. The wind direction is rarely even nearly constant for a 24 hour period, and fluctuations in wind direction can have a disproportionately large impact on the V wind component if the wind direction is treated as constant throughout the period. Although the decomposition into U and V components could be achieved with a very strict set of filtering criteria for wind direction, the decision was taken to restrict the analysis to the scalar wind speed. A careful analysis of the spectral and cross-spectral properties of the U and V wind components can reveal important results about the isotropy of the wind field, and is an interesting area for further analysis.

The analysis in this paper focused on conditions over the sea. However, the results implied that conditions may not be the same over the land as over the sea. For example, the shape of the quadrature-spectrum for Horns Rev was less pronounced for the easterly sector winds than the westerly sector winds, and the quadrature-spectrum for Nysted (which is closer to coastlines from all directions) did not show the clear or systematic patterns that were seen for the Horns Rev case. Furthermore, Woods et al (2011) found that it was not important to include wind speed in an analytical expression for the shape of the co-spectra and quadrature-spectra for pairs of meteorological masts over the land, which indicates that it might be less appropriate to apply Taylor's hypothesis over the land than over the sea. Overall, the models proposed here have a simpler form than those suggested by Woods et al (2011), which is likely to be due to the simpler and more homogeneous conditions over the sea compared to the land. Meteorological conditions over the sea are different to conditions over the land due to the low surface roughness, the absence of topographic effects the ample supply of moisture and the stability conditions driven by advection of air masses rather than the radiation balance. Such differences can influence the spectral properties of the wind speed, particularly in the mesoscale range. For example, organized mesoscale structures such as cellular convection, convective rolls or gravity waves may have a strong influence on the mesoscale wind speed over the sea, while topographic effects might be far more important over the land. These differences are important for the planning and operation of offshore wind energy, where the spatial correlation in wind speeds at a certain frequency can undermine the potential for smoothing of the aggregated power output from spatially distributed turbines.

7 Conclusions

In this paper, co-spectra and quadrature-spectra were calculated using 10 min wind speed observations from pairs of offshore meteorological masts over the North Sea and the Baltic Sea respectively. Separation distances of the masts ranged from 2.13 km to 12.4 km, and results were binned according to the relative direction between the mean wind and the orientation of the mast pairs. Co-spectra and quadrature-spectra were also calculated using 3 month mesoscale model simulations over the North Sea and the Baltic Sea, and good agreement was found between the observed and modelled spectra when the flow was coming from the sea.

For flow over the sea, it was shown that the co-spectrum and quadrature spectrum could be effectively modelled using damped cosine and sine functions based on a constant delay time associated with advection between the two sites. The simple analytical models were found to be an excellent fit to the spectra derived from mesoscale modelling over the sea, and for observed wind speed where the flow had a long sea fetch. For flow that did not have a long sea fetch, the patterns in the spectra were less clear, although there was still a greater contribution to the quadrature spectrum for longitudinal flow than for lateral flow. The extent to which the analysis presented here for flow over the sea could be extended or adapted to flow over a relatively homogeneous land area has not been tested.

The results presented here are unique because they are based on pairs of tall offshore measurement masts, which are much less common than onshore measurement masts. The situation of the Horns Rev I wind farm, with a long sea fetch to the west, and a coastline orientated nearly in the North-South direction to the east, provided a particularly simple and useful site for the analysis. Furthermore, the use of the WRF model to expand the scope of the observation analysis was a useful and novel application of mesoscale modelling.

Like most spectral analysis of geophysical time series, the results were somewhat limited by the assumptions of stationarity. This meant that many interesting meteorological cases were not included in the analysis, because they contained large changes in wind speed or wind direction. In addition, no attempt to separate the analysis into different classes of local or large scale atmospheric conditions was made. The precise impact of mesoscale features such as cellular convection or gravity waves on the shapes of the spectra is an interesting area for future work.

Acknowledgements The contribution of C.L. Vincent was supported by the Danish Council for Independent Research – Technology and Production Sciences (case number 10-093196) individual post-doc project. The contribution of the remaining authors was supported by the Danish project 'Mesoscale variability and the variability of wind and production of offshore wind farms (contract number PSO-1741). The authors are grateful to Dong Energy and Vattenfall for permission to use observational data from the Horns Rev I and Nysted wind farms.

References

Davenport AG (1961) The spectrum of horizontal gustiness near the grounds in high winds. Quart J Roy Meteor Soc 87:194–211

Davies-Jones R (2002) Linear and nonlinear propagation of supercell storms. J Atmos Sci 59:3178–3205

Gage KS, Nastrom GD (1986) Theoretical interpretation of atmospheric wavenumber spectra of wind and temperature observed by commercial aircraft during GASP. J Atmos Sci 43:729–740

Kain JS, Fritsch JM (1990) A one-dimensional entraining/detraining plume model and its application in convective parameterization. J Atmos Sci 47:2784–2802

Kristensen L (1979) On longitudinal spectral coherence. Bound Layer Meteorol 16:145–163

Kristensen L, Jensen NO (1979) Lateral coherence in isotropic turbulence and in the natural wind. Bound Layer Meteorol 17:353–373

Kristensen L, Kirkegaard P (1986) Sampling problems with spectral coherence. Risø report Risø-R-526, Risø National Laboratory, Roskilde, Denmark

Larsen GC, Mann J, Ighil TA, Mouritzen AS (2009) Do wind farms influence large scale turbulence? Extended Abstracts for Euromech Colloquium 508, pp 38–40

Larsén XG, Larsen S, Badger M (2011a) A case-study of mesoscale spectra of wind and temperture, observed and simulated. Quart J Roy Meteor Soc 137:264–274

Larsén XG, Vincent CL, Larsen SE (2011b) Xiaoli's co-spectra paper. Journal Manuscript under preparation

Madsen H (2007) Time Series Analysis. Chapman & Hall

Mass CF, Ovens D, Westrick K, Colle BA (2002) Does increasing horizontal resolution produce more skillful forecasts? Bull Amer Meteor Soc 83:407–430

Molinari J, Dudek M (1992) Parameterization of convective precipitation in mesoscale numerical models: a critical review. Mon Wea Rev 120:326–344

Nakanishi M, Niino H (2009) Development of an improved turbulence closure model for the atmospheric boundary layer. JMSJ 87:895–912

Nastrom GD, Gage KS (1985) A climatology of atmospheric wavenumber spectra of wind and temperature observed by commercial aircraft. J Atmos Sci 42:950–960

Schlez W, Infield D (1998) Horizontal, two point coherence for separations greater than the measurement height. Bound Layer Meteorol 87:459–480

Sioutas MV, Flocas HA (1996) Influence of environmental winds on propagation and motion of thunderstorms in northern greece. J Geophys Res 101:26,255–26,265

Skamarock WC (2004) Evaluating mesoscale NWP models using kinetic energy spectra. Mon Wea Rev 132:3019–3032

Skamarock WC, Klemp JB, Dudhia J, Gill DO, Barker DM, Duda MG, Huang XY, Wang W, Powers JG (2008) A description of the advanced research WRF version 3. NCAR Technical Note TN-475+STR, NCAR, Boulder, Col-

orado

Sørensen P, Hansen AD, Rosas PAC (2002) Wind models for simulation of power fluctuations from wind farms. J Wind Eng Ind Aerodyn 90:1381–1402

Vigueras-Rodrìguez A, Sørensen P, Cutululis NA, Viedma A, Donovan MH (2010) Wind model for low frequency power fluctuations in offshore wind farms. Wind Energy 13:471–482, DOI 10.1002/we.368

Woods JW, Davy RJ, Russell CJ, Coppin PA (2011) Cross-spectrum of wind speed for meso-gamma scales in the upper surface layer over South-Eastern Australia. Bound Layer Meteorol 141:93–116, DOI: 10.1007/s10546-011-9632-2

Markov-Switching AR-GARCH models for the characterization and forecasting of short-term offshore wind power fluctuations

Pierre-Julien Trombe*, Pierre Pinson, Henrik Madsen
DTU Informatics, Technical University of Denmark

August 15, 2011

Abstract

Short-term wind power fluctuations at offshore wind farms are characterized by complex dynamics combining several effects often observed independently of each others in time series: autocorrelation, heteroscedasticity and regime switching. Short of on-site meteorological observations to relate these effects to meteorological phenomena, we propose a general model formulation to capture the different effects observed, solely based on wind power measurements. The model is an extension of Markov-Switching Autoregressive (MSAR) models and includes a GARCH specification to cope with the heteroscedasticity. We present an advanced estimation method based on Markov Chain Monte Carlo (MCMC) and address its strengths and weaknesses. Finally, we analyze the predictive power of our model on a one-step ahead exercise of time series sampled over 10 minute intervals. Its performances are compared to state-of-the-art models and highlight the interest of including a GARCH specification for density forecasts.

Keywords: Wind power forecasting, Markov-Switching, Garch, Probabilitsic forecasting, Offshore, MCMC, Griddy-Gibbs.

*Corresponding author: Pierre-Julien Trombe
Department of Informatics and Mathematical Modelling, Technical University of Denmark,
Richard Petersens Plads, DK-2800 Kgs Lyngby, Denmark.
e-mail: pjt@imm.dtu.dk

1 Introduction

Climate change calls for the reduction of greenhouse gas emissions and thus a growing development of renewable energy sources. Benefiting from favorable governmental policies and large wind resources, countries in the north-west of Europe are rapidly increasing their wind power capacities. Historically, onshore installations have prevailed, but offshore wind energy is now growing significantly. In Denmark, the latest figures stated that wind power accounted for about 20% of the domestic electricity supply and, out of 3124 MW wind power capacity, 424 MW were installed offshore [1]. The current trend is towards the development of large-scale offshore projects capable of generating several hundreds of MW each. Indeed, sitting wind farms out at sea has substantial advantages (i) more space available, (ii) a decrease of the frequency and duration of low wind speeds and (iii) an increased persistence for high wind speeds. Offshore wind farms are then expected to have higher capacity factors (i.e. the ratio of the actual power output over a given period of time, to the maximum output if the plant had been operated at full capacity) [2].

However, in practice, integrating significant amounts of wind power into electricity systems remains a challenge and requires dedicated prediction tools for real-time monitoring, operation scheduling and energy trading. A comprehensive introduction on these aspects from a physical perspective is given in [3]. Lately, problems regarding the grid balance have arisen as a result of the new integration of large offshore wind farms into the power supply system. Power generation of these wind farms turns out to be highly volatile, increasing the risk of imbalance in the power system. This originates from the specific design of large offshore wind farms which concentrate a large amount of wind power capacity within a relatively small area, increasing the impact of local meteorological phenomena (wind and rain fronts among others) on their short-term power production. For instance, measurements from the offshore site of Horns Rev reveal changes in the output power with an amplitude of 60% the wind farm maximum capacity, within 15-20 minutes [4]. Such levels of fluctuations can rarely be observed onshore where similar capacities would be spread over a much wider area, smoothing out the effects of the weather instabilities [5]. As a consequence, maintaining the short-term balance of the transmission system (i.e. matching the power supplied by the plant and the electricity demand) and the stability of the electricity system has become a critical issue and needs to be handled carefully to prevent potential damages (blackouts, etc.) on the power system.

The contribution of this paper is to present a real-world case study of modeling and forecasting of high frequency wind power time series. The innovation of our approach comes from the formulation of the proposed model which allows to capture up to three different effects: autocorrelation, heteroscedasticity and regime switching (the generic name of our model is MS-AR-GARCH). This leads to a very general model formulation which requires an advanced estimation method for identifying and separating these different effects. Furthermore, our will is also to bridge the gap between the formulation of such model and the issues linked to its implementation in practice, for both synthetic and real data.

This paper is organized as follows. Section 2 summarizes the latest achievements in wind power meteorology for very short-term applications and states the motivations for this study. Section 3 introduces the data and shows some of their major features. Then, in Section 4, specifications for the model we propose are discussed throughout a brief overview of the literature on Markov-Switching models which constitute a special class of regime switching models, and on GARCH models which are generalized forms of heteroscedastic models. Section 5 gives a detailed description of the estimation method based on a Markov Chain Monte Carlo algorithm and the reasons for such a choice. Applications to both synthetic and real data are presented and the accuracy and robustness of the estimation method are assessed. A forecast evaluation on real data is performed in Section 6 where the performances

of our model are compared to current benchmark models for very short-term wind power fluctuations. Finally, Section 7 delivers concluding remarks.

2 Motivations based on the state-of-the-art

The motivation of this paper is twofold. First, with the planned deployment of large-scale offshore wind farms, there is an urging need to build up on the existing knowledge on these wind power fluctuations by characterizing the dynamics and identifying the factors which drive the wind power fluctuations in the very short-term. As a first step towards this understanding, [6] reported that at a temporal resolution of 10 minutes, certain weather conditions at Horns Rev and in particular north-westerly winds very much favored large wind power fluctuations. Then, [7] proposed an aggregated model of individual wind turbines and showed its relative ability to simulate consistent wind power fluctuations at different time scales, from a few minutes up to 2 hours ahead. Very recently, a spectral analysis of wind speed measurements at Horns Rev by [8] identified specific seasonal cycles as key features of wind variability.

Second, most of the state-of-the-art statistical methods gives focus to large prediction horizons, from 1 hour to a couple of days, and show limited forecasting skills for very short-term horizons, within tens of a minute, at which large wind power fluctuations must be monitored [9]. This low level of predictability is due to the complex nonlinearities in the output power dynamics which cannot be captured by conventional models. Hence, there is a need for dedicated statistical methods capable of generating accurate forecasts for very short-term horizons. In that regard, our approach on forecasting is probabilistic and the respective performance of the models presented in this paper will be evaluated accordingly [10].

As a first attempt to deal with the low predictability of the output power of large-scale offshore wind farm, regime-switching approaches and more specifically Markov-Switching models have received a growing interest within the wind power community. Since their very first introduction in econometrics by [11], they have been commonly used in many disciplines such as speech recognition [12] or computational biology [13], for instance. This class of models is prized for its ability to account for structural breaks or sudden changes in the process dynamics. In meteorology, Markov-Switching models are often used to estimate an unobservable climate state which ideally governs other climate variables such as wind speed or wind direction. For the specific case of large-scale offshore wind farms, the inferred states or regimes can be interpreted as changes of the wind farm behavior, in terms of power generation. Besides that, Markov-Switching AutoRegressive (MSAR) models are shown to have better point forecast performances than AutoRegressive Moving Average (ARMA), Smooth Transition AutoRegressive (STAR) and Self-Exciting Threshold AutoRegressive (SETAR) [14]. Alternatively, a MSAR model is proposed in [15] with adaptive estimation of the parameters which allows parameter estimates to change over time to better account for the long-term variations of the wind characteristics. Density forecasts generated with that method are shown to be much sharper and have a better calibration than those generated with AR models.

Nevertheless, one can argue that keeping the variance constant over time within each regime stands as a strong limitation for the forecasts sharpness when periods of different volatility levels alternate. This may mistakenly lead to over determine the optimal number of states when fitting the model to the data. One class of models capable of relaxing the constant variance assumption is the Generalized AutoRegressive Conditional Heteroscedasticity (GARCH) model, allowing the conditional variance in each regime to follow an ARMA process [16]. The GARCH class of models is appealing because it can cope with volatility clustering which is a clear issue when studying offshore wind power generation at high fre-

quencies. Therefore, the present study proposes to extend MSAR models with a GARCH specification for the conditional variance dynamic in each regime (hence the resulting model name MS-AR-GARCH). This extension of the original MSAR model is expected to allow for a better identification of the volatility clustering effect and to a more parsimonious parametrization regarding the number of regimes.

3 Data from large offshore wind farms

The data considered in the present study cover the time period from 16 February 2005 to 25 January 2006 and were recorded at Horns Rev I, the second largest offshore wind farm in operation in the world at that time. Horns Rev I is located 15 km away from the west coast of Jutland (Denmark) and consists of 80 turbines of 2MW, for a nominal capacity of 160 MW. Original data were provided as individual time series of wind power measurements for each of the 80 turbines at one second time intervals.

The original data are averaged in order to generate an aggregated time series of wind power fluctuations for the entire wind farm. A 10 minute resolution is arbitrarily chosen within the range of values over which significant power fluctuations are observed [4]. An other reason to justify this choice is that grid operators monitor offshore wind farms at similar temporal resolutions [9]. The sampling procedure first consists in producing spatio-temporal averages over 10 minute intervals for which a minimum of 75% of the data are of good quality. These averages are then normalized by the nominal capacity of the wind farm, following [17]. No attempt is made to fill in missing data points and many gaps remain present in the data. A 10 day episode of this time series is depicted on Figure 1. It can be noticed that the power generation is a double-bounded process, below and above. As a matter of fact, the power generation of a wind farm can neither be negative nor exceed its maximum capacity.

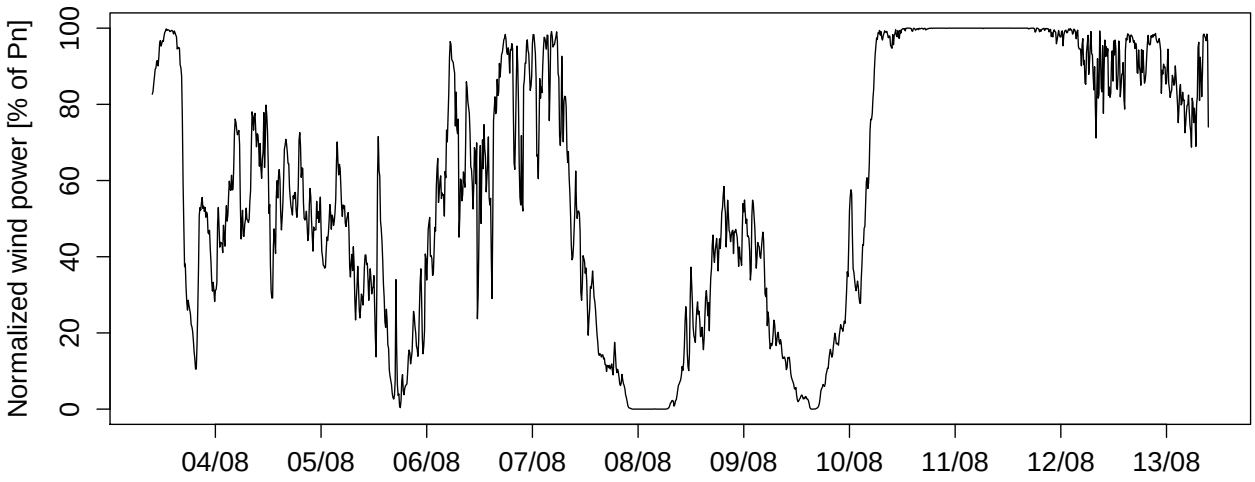

Figure 1: Time series of normalized wind power generation at Horns Rev I over a 10 day episode in August 2005. The time series is sampled at a time scale of 10 minutes.

Moreover, technical specificities and constraints of wind turbines make that wind power generation is not a linear function of the wind speed. The relationship between wind speed and power generation is described by the so-called power curve. This relationship is often estimated to convert wind speed forecasts into wind power forecasts. For a more detailed description of its use in practice, we refer to [18]. More generally, the power curve is considered a function of both the wind speed and the wind direction and must be estimated for every

single wind farm. Nevertheless, wind speed and wind direction are not the only two factors that are believed to govern wind farm behavior. In the specific case of large offshore wind farms, it is also commonly assumed that complex local meteorological phenomena have a strong impact on the power generation. Ongoing research works on these phenomena are still in an early stage, and identifying them would require to combine both meteorological and statistical approaches which is not the purpose of this study. As for now, early assumptions based on empirical observations have described these phenomena as combinations of intense precipitations and wind gusts [19].

From Figure 1, one can see periods characterized by very different dynamics alternate with various frequencies and durations. This latter observation reveals the non-stationary behavior of this wind power time series, whatever the time scale one considers. This issue is further discussed in [8]. Non-stationarity is one of the reasons why most linear time series models show limited prediction skills. This feature is further illustrated on figure 2 which plots the squared residuals of the best autoregressive model (of order 3), the associated autocorrelation function (ACF) and the partial ACF (PACF) for the wind power time series. The model was fitted to the whole time series but to enhance visualization of the results, the squared residuals are only plotted for the period of time spanning 1 August 2005 to 26 January 2006. First, a look at the squared residuals highlights the volatility clustering effect, meaning that large errors tend to be followed by large errors and similarly, small errors tend to be followed by small errors. It is a feature often observed for data sampled at a high frequency. Then, the ACF of the squared residuals indicates that the autocorrelation is significant up to very large lags which reveals the heteroscedastic behavior of the errors. Finally, the PACF allows one to evaluate the number of significant lags for the time series of squared residuals. It indicates that the conditional variance should be modeled as the weighted sum of approximately the last 20 squared errors. However, for the sake of parsimony, an ARCH process of large order can well be substituted by a GARCH specification [16]. This well spread empirical approach offers the double advantage of drastically reducing the number of coefficients to be estimated while conserving the model adequacy. It also introduces a decreasing weight structure, from the most recent to the oldest past squared errors, for the computation of the conditional variance.

4 Model specifications

4.1 Wind power predictive density

As mentioned in the previous section, the time series of wind power is nonlinear and non-stationary. The smoothing effect outlined when considering a collection of wind turbines scattered over a wide area does not apply in the case of a single large-scale offshore wind farm. Furthermore, wind turbines do not generate electricity for wind speeds below the so called cut-in speed ($\sim 4m.s^{-1}$) or above the the cut-off speed ($\sim 25m.s^{-1}$). In addition, for wind speeds ranging from $15m.s^{-1}$ to $25m.s^{-1}$, wind turbines operate at full capacity and produce a constant level of power. Consequently, the power generation drops to 0 or reaches its maximum in a significant number of occasions. From a statistical modeling perspective, it means that the process does meet its lower and upper bounds which generates mass points at the extremities of the wind power distribution. This prevents the use of a logistic transformation as adopted in [20] since the mass points would remain, even after transformation. In view of these limitations, truncated and censored normal distributions stand as appealing alternatives to the more classical Normal distribution. Recent developments that use the two former distributions applied to wind data include [21]. However, Markov-Switching models imply the computation of distribution mixtures. For the sake of the estimation method

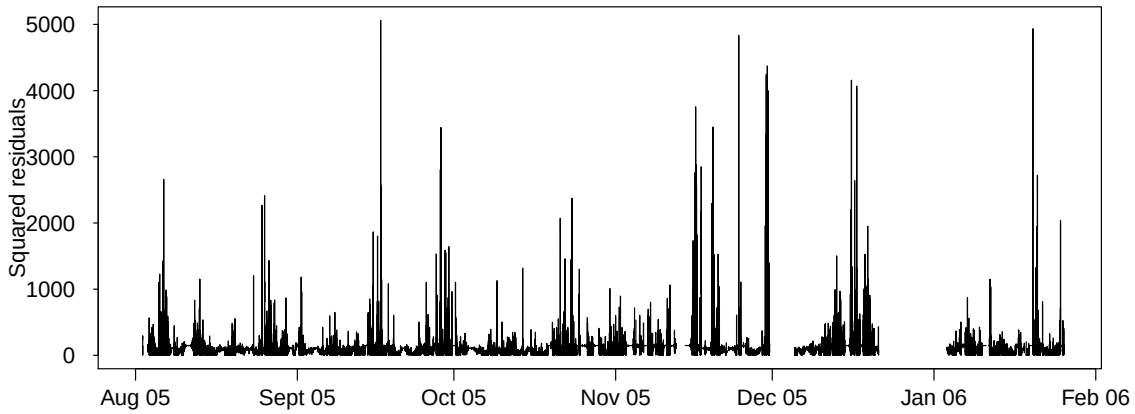

(a) Squared residuals obtained after fitting an AR(3) model to the wind power time series.

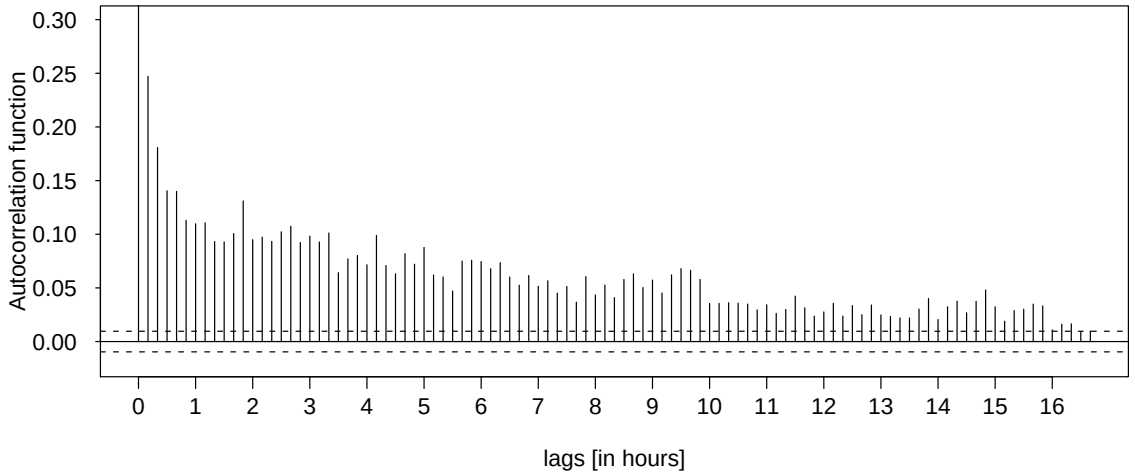

(b) Autocorrelation function of the squared residuals.

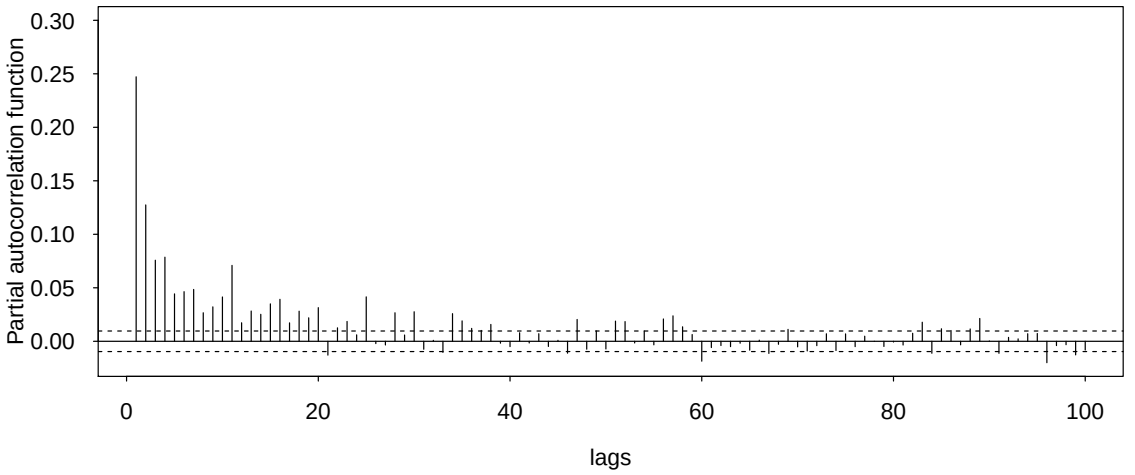

(c) Partial autocorrelation function of the squared residuals.

Figure 2: Volatility clustering and heteroscedasticity of the wind power time series.

simplicity, we choose to consider neither the truncation nor the censoring of the Normal distribution since mixtures of these distributions would be to cumbersome to compute. For similar reasons, the Generalized Logit-Normal distribution as proposed in [22] was not considered. Finally, we focused on 2 symmetric distributions, namely the Student-t and Normal distributions. The Student-t distribution has the advantage of being more heavy-tailed than the Normal distribution, making the regimes more stable [23]. Its drawback is that it has

one extra parameter (its degree of freedom) which is difficult to estimate [24]. The use of the Normal distribution, though known as not optimal for wind power time series is therefore considered as a natural starting point for validating the model in this study. We leave questions on more appropriate distributions for further research.

4.2 GARCH models in meteorology

An overview of the time series analysis literature shows that GARCH models have been extensively used in econometrics and finance but remains rather unpopular in other fields. In meteorology, GARCH models are often employed in a single regime framework and applied to wind speed or air temperature time series for characterizing their volatility. [25] first fitted an AR-GARCH model to daily wind speed measurements from Canada and illustrated the better in-sample performance of his heteroscedastic model over homoscedastic ones in presence of high volatility in the data. A bivariate GARCH model was then used in [26] to characterize wind components (i.e. the rectangular components of wind speed and wind direction) and their variability at a time scale of 1 minute and relate them to local meteorological events in the Sydney harbor. An other meteorological application of GARCH models presented the usefulness of a ARMA-GARCH-in-mean model to estimate the persistence in the volatility of wind speed measurements at different heights [27]. Other works investigating on the applicability of GARCH models to air temperature time series include [28].

In contrast to these latter studies whose primary focus is in-sample estimation, [29] and [30] use AR-GARCH models to generate point and density forecasts for temperature and weather derivative pricing, respectively. In addition, the recent work by [31] also presents out-of-sample results. It extends the methodology developed in [29] and used several types of GARCH models to generate daily wind speed density forecasts and converts them into wind power forecasts. This work demonstrates the good ability of GARCH models for generating density forecasts when compared to atmospheric models for early look ahead horizons, from 1 up to 4 days. Another methodology is proposed by [20] in which an ARIMA-GARCH model is used to generate multi-step density forecasts of wind power, outperforming current benchmark models in the short-term, from 15 minutes up to 6-12 hours. Interestingly, all these studies give empirical evidence of the strong potential of using the GARCH class of models for predicting weather related variables in the very short-term when these variables are highly volatile.

4.3 Existing Markov-Switching models with GARCH errors

Seminal references of combining Markov Switching and AutoRegressive Conditional Heterossedasticity (MS-ARCH) include [32] and [33]. In practice, capturing time-varying variance with a reasonable number of ARCH terms remains an issue. It often calls for a GARCH specification instead in order to reduce the number of coefficients to be estimated. The difficulty that arises when generalizing MS-ARCH to MS-GARCH relates to the historical path dependency of the conditional variance which is intractable, making that generalization almost computationally infeasible.

Nevertheless, there exist a few approaches to avoid that problem. Regarding maximum likelihood methods, the idea consists in approximating the conditional variance as a sum of past conditional variance expectations as in [24]. This model was later extended by [23] yielding improved volatility forecasts. Alternatively, [34] suggested a new formulation for MS-GARCH models by disaggregating the overall variance process into separate processes in each regime. An other way of tackling the path dependency problem consists in using Monte Carlo Markov Chain (MCMC) simulations to infer that path by sampling from the conditional distribution of the states of the Markov chain. This can be implemented by

data augmentation as described in [35]. The strength of this approach is that it can be applied for the estimation of many variants of Markov-Switching models.Closer to our problem, [36], [37], [38] proposed three different MCMC algorithms for the Bayesian estimation of MS-ARMA-GARCH, MS-ARX-GARCH and MS-GARCH models, respectively.

Some other difficulties arise when estimating MS-GARCH models. They may be caused by the structural specification of the model or else by the numerical tool used for parameter estimation. For instance, maximum likelihood estimation methods implemented with a numerical optimizer often encounter specific optimization problems due to starting values, inequality constraints or else local minima. Besides, the two formulations of the MS-GARCH model developed in [24] and [23] are based on an approximation for the recursive update of the conditional variance which leads to further estimation complexity. As for the MS-GARCH model in [34], it looses its initial appeal of being analytically tractable along with the inclusion of autoregressive terms in the mean equation which does not match with our model specification to combine AR and GARCH effects with Markov Switching. Along that last comment, it is important to emphasize that most of the studies involving likelihood estimation of MS-GARCH models have as a prime concern the capture of the heteroscedasticity present in the time series and were not designed to cope with data also featuring strong autocorrelation.

In comparison, Bayesian inference offers an alternative framework which allows to overcome most of likelihood estimation problems:

- the robustness of MCMC samplers to starting values can be evaluated by running several Markov chains with different starting values and tested for differences in their outputs,
- inequality constraints can be handled through the definition of prior distributions (Gibbs sampler) or through a rejection step when the constraint is violated (Metropolis-Hastings sampler),
- theoretically, local minima pitfalls are avoided by simulating the Markov chain over a sufficiently large number of iterations (law of large numbers)
- misspecification of the number of states of the Markov chain can be assessed by a visual inspection of the parameter posterior distributions (check for multiple modes).

Moreover, model parametrization limitations linked to the integration of autoregressive terms in the mean equation do not apply in Bayesian estimation and there is no fundamental implementation differences in estimating a MS-GARCH and a MS-ARMA-GARCH model. Of course, the present study would be very partial if the main bottlenecks in using MCMC simulations such as computational greediness or the tuning of the prior distributions were not mentioned. Therefore, we refer to subsection 4.4 for a detailed description of the main implementation issues of MCMC samplers. In addition, studies on the respective advantages and drawbacks of maximum likelihood and Bayesian estimation methods are available in [39]. To conclude this discussion, let us say that our goal is not to contribute to the pros and cons debate of maximum likelihood against Bayesian estimation but rather to find the method that is the most suitable for our problem. In this light, our choice to estimate the MS-AR-GARCH model in a Bayesian fashion was motivated by the enhanced flexibility in combining AR and GARCH effects under the assumption of structural breaks in the process.

4.4 The model definition

To model the stochastic behavior of a given time series of wind power $\{y_t\}$, a MS(m)-AR(r)-GARCH(p,q) model is proposed as follows:

$$y_t = \theta_0^{(S_t)} + \sum_{i=1}^{r} \theta_i^{(S_t)} y_{t-i} + \sqrt{h_t}\varepsilon_t \tag{1}$$

$$h_t = \alpha_0^{(S_t)} + \sum_{i=1}^{q} \alpha_i^{(S_t)} \varepsilon_{t-i}^2 + \sum_{j=1}^{p} \beta_j^{(S_t)} h_{t-j} \tag{2}$$

where $\{h_t\}$ is the conditional variance at time t, $\{\varepsilon_t\}$ is a sequence of independently distributed random variables following a Normal distribution $\mathcal{N}(0,1)$ and $\boldsymbol{S} = (S_1, \ldots, S_T)$ is a first order Markov chain with a discrete and finite number of states m and transition probability matrix $\mathbf{P}$ of elements:

$$Pr(S_t = j | S_{t-1} = i) = p_{ij} \quad \text{for} \quad i, j = \{1, \ldots, m\} \tag{3}$$

For full flexibility, all AR and GARCH coefficients are chosen to be state dependent. In addition, to ensure positivity of the conditional variance, constraints on the model coefficients are imposed as follows:

$$\alpha_0^{(k)} \geq 0,\ \alpha_i^{(k)} > 0,\ \beta_j^{(k)} \geq 0 \quad \text{for} \quad i = \{1, \ldots, p\},\ j = \{1, \ldots, q\},\ k = \{1, \ldots, m\} \tag{4}$$

Finally, the following inequality constraints are applied to ensure covariance stationarity:

$$0 < \sum_{i=1}^{q} \alpha_i^{(k)} + \sum_{j=1}^{p} \beta_j^{(k)} < 1 \quad \text{for} \quad k = \{1, \ldots, m\} \tag{5}$$

From here on, we adopt the following notations:

$$y = (y_1, y_2, \ldots, y_T) \tag{6}$$

$$y_{[1,t]} = (y_1, \ldots, y_t) \tag{7}$$

$$S_{[1,t]} = (S_1, \ldots, S_t) \tag{8}$$

$$S_{\neq t} = (S_1, \ldots, S_{t-1}, S_{t+1}, \ldots, S_T) \tag{9}$$

$$\pi_k = (p_{k1}, \ldots, p_{km})' \quad \text{for} \quad k = \{1, \ldots, m\} \tag{10}$$

$$\theta^{(k)} = [\theta_0^{(k)}, \ldots, \theta_r^{(k)}]' \quad \text{for} \quad k = \{1, \ldots, m\} \tag{11}$$

$$\alpha^{(k)} = [\alpha_0^{(k)}, \ldots, \alpha_q^{(k)}, \beta_1^{(k)}, \ldots, \beta_p^{(k)}]' \quad \text{for} \quad k = \{1, \ldots, m\} \tag{12}$$

$$\boldsymbol{\Theta} = [\theta^{(1)}, \ldots, \theta^{(m)}, \alpha^{(1)}, \ldots, \alpha^{(m)}, \pi_1, \ldots, \pi_m] \tag{13}$$

5 MCMC implementation

Bayesian inference applied to complex models and large amounts of data has been strongly enhanced by the development of computational methods such as Markov chain simulations. Besides providing a robust and easy-to-implement solution to circumvent the path dependency problem when estimating the MS-GARCH class of models, MCMC techniques offer broader possibilities such as incorporating existing information on the parameter distributions and estimating their full conditional posterior distributions, for instance. Their major interest is the possibility to divide the set of unknown parameters $\boldsymbol{\Theta}$ into smaller blocks to sample from the block conditional posterior distributions instead of sampling from the

complex and joint posterior of the full set of parameters. For a practical presentation of MCMC techniques, we refer to [40].

Estimating MS-AR-GARCH models in a Bayesian framework is a procedure that implies sampling from the augmented parameter distribution $p(\boldsymbol{S}, \boldsymbol{\Theta}|y)$:

$$p(\boldsymbol{S}, \boldsymbol{\Theta}|y) \propto p(y|\boldsymbol{S}, \boldsymbol{\Theta})p(\boldsymbol{S}|\boldsymbol{\Theta})p(\boldsymbol{\Theta}) \tag{14}$$

This can be achieved through a 3 step procedure by implementing a MCMC algorithm that iterates as follows:

- sample the regime sequence by data augmentation,
- sample the transition probabilities from a Dirichlet distribution,
- sample the AR and GARCH coefficients with the Griddy-Gibbs sampler.

5.1 Sampling the regime sequence

Generating sample paths of the regime sequence $\boldsymbol{S}$ for Markov-Switching models is facilitated by a class of techniques known as data augmentation. The early idea by [41] is to recursively consider each of the latent state variables S_t of the hidden Markov chain as missing and compute its conditional distribution $p(S_t|S_{\neq t}, \boldsymbol{\Theta})$. It becomes then possible to generate a random draw from that conditional distribution with the Gibbs sampler as in [42]. This procedure is called *single-move sampling* and requires the number of regimes m to be known and finite. Later variants for Hidden Markov Models (HMM) and Markov switching models are respectively reviewed in [43] and [35].

At a given time t, the conditional distribution of the latent state variable S_t is obtained as follows:

$$\begin{aligned} \forall\ k \in \{1, \dots, m\}, \quad P(S_t = k|y, S_{\neq t}, \boldsymbol{\Theta}) &= \frac{P(y, S_t = k, S_{\neq t}, \boldsymbol{\Theta})}{P(y, S_{\neq t}, \boldsymbol{\Theta})} \\ &= \frac{P(y|S_t = k, S_{\neq t}, \boldsymbol{\Theta})P(S_t = k, S_{\neq t}, \boldsymbol{\Theta})}{P(y|S_{\neq t}, \boldsymbol{\Theta})P(S_{\neq t}, \boldsymbol{\Theta})} \\ &= \frac{P(y|S_t = k, S_{\neq t}, \boldsymbol{\Theta})P(S_t = k|S_{\neq t}, \boldsymbol{\Theta})}{P(y|S_{\neq t}, \boldsymbol{\Theta})} \end{aligned} \tag{15}$$

And after discarding the scaling factor $P(y|S_{\neq t}, \boldsymbol{\Theta})$, we obtain:

$$P(S_t = k|S_{\neq t}, y, \boldsymbol{\Theta}) \propto P(y|S_t = k, S_{\neq t}, \boldsymbol{\Theta})P(S_t = k|S_{\neq t}, \boldsymbol{\Theta}) \tag{16}$$

In the equation above, 2 different quantities have to be computed. First, $P(y|S_t = k, S_{\neq t}, \boldsymbol{\Theta})$ is the complete data likelihood, conditioned on the chain being in state k at time t and given the full set of parameters $\boldsymbol{\Theta}$ and can be calculated as follows:

$$\begin{aligned} P(y|S_t = k, S_{\neq t}, \boldsymbol{\Theta}) &= \prod_{t=max(r,p,q)}^{T} P(y_t|, S_t = k, S_{[1,t-1]}, y_{[1,t-1]}, \boldsymbol{\Theta}) \\ &= \prod_{t=max(r,p,q)}^{T} \frac{1}{\sqrt{2\pi h_t}} \exp\left(-\frac{(y_t - \theta_0^{(S_t)} - \sum_{i=1}^{r} \theta_i^{(S_t)} y_{t-i})^2}{2h_t}\right) \end{aligned} \tag{17}$$

with h_t being defined as in equation (2).

Second, the Markov property applies on $P(S_t = k|S_{\neq t}, \boldsymbol{\Theta})$. Given a sample $S_{\neq t}$ of the entire regime sequence but at time t, the state variable S_t only depends on S_{t-1}, and S_{t+1} only depends on S_t:

$$\begin{aligned} P(S_t = k|S_{\neq t}, \boldsymbol{\Theta}) &= P(S_t = k|S_{t-1} = i, S_{t+1} = j) \\ &= \frac{p_{ik}p_{kj}}{\sum_{k=1}^{m} p_{ik}p_{kj}} \end{aligned} \tag{18}$$

Finally, the Gibbs sampler [44] is used to generate a random sample of the latent state variable S_t from its updated conditional distribution. The state of the Markov chain at time t can then be updated and this sampling procedure is recursively repeated for the remaining state variables of the hidden Markov chain.

Because of the path dependency structure of MS-GARCH models, computing marginal likelihood of the state variables is not feasible as it is for MSAR or MS-ARCH models [35]. Hence, the posterior distributions of the states variables can only be obtained in the form of smoothed probabilities. Let us recall that one can derive different quantities for the optimal inference of the regime sequence:

- *the filtered probabilities* $P(S_t = k|y_{[1,t]}, \boldsymbol{\Theta})$ which infer the state variable S_t conditioning upon the vector of parameters and all past and present information $y_{[1,t]}$,
- *the smoothed probabilities* $P(S_t = k|y, \boldsymbol{\Theta})$ which are the outputs of the inference of S_t using the past, present and future information $y = y_{[1,T]}$,
- *the predicted probabilities* $P(S_{t+1} = k|y_{[1,t]}, \boldsymbol{\Theta})$ which correspond to the one-step ahead inference S_{t+1} at time t and only use past information $y = y_{[1,t]}$.

For a given state variable S_t, its posterior distribution $P(S_t = k|y)$ is computed by averaging the number of occurrences of the Markov chain being in state k at time t over the N iterations of the algorithm:

$$P(S_t = k|y) = \frac{1}{N}\sum_{n=1}^{N} \mathbb{1}\{S_t^{(n)} = k\} \quad \text{for} \quad k = \{1, \ldots, m\} \tag{19}$$

with $S_t^{(n)}$ being the draw of S_t at the n^{th} iteration of the MCMC algorithm.

5.2 Transition probability matrix sampling

Sampling the transition probability matrix $\mathbf{P}$ is done by using a Dirichlet distribution [35]. The key assumption is that the rows of $\mathbf{P}$ are mutually independent since $\mathbf{P}$ only depends on the regime sequence $\mathbf{S}$. Therefore, they can be sampled in a random order. Given an independent prior distribution $p(\pi_k)$ and using Bayes' theorem, we obtain the conditional distribution of the k^{th} row of $\mathbf{P}$ as follows:

$$\begin{aligned} p(\pi_k|y, \boldsymbol{S}, \boldsymbol{\Theta}_{-\pi_k}) &\propto p(\pi_k)p(\pi_k|\boldsymbol{S}) \\ &\propto p(\pi_k)\prod_{r}^{T}(d_{k1})^{\eta_{k1}} \ldots (d_{km})^{\eta_{km}} \end{aligned} \tag{20}$$

where the η_{ki}'s correspond to the numbers of one-step transitions from regime k to regime i in the hidden Markov chain and the d_{ki}'s are the parameters of the multivariate distribution modelling the transition probabilities.

For a 2 state Markov chain, the beta distribution is traditionally used as prior for binomial proportions, with parameters d_{k1} and d_{k2}, resulting in the conditional distribution of the k^{th} row of P being Beta distributed:

$$p(\pi_k|y, \boldsymbol{S}, \boldsymbol{\Theta}_{-\pi_k}) \sim B(\eta_{k1} + d_{k1}, \eta_{k2} + d_{k2}) \tag{21}$$

For a m state Markov chain, and $m \geq 2$, the posterior Beta distribution can be generalized to a Dirichlet distribution [45]:

$$p(\pi_k|y, \boldsymbol{S}, \boldsymbol{\Theta}_{-\pi_k}) \sim D(\eta_{k1} + d_{k1}, \eta_{k2} + d_{k2}, \ldots, \eta_{km} + d_{km}) \tag{22}$$

with $d_{k1}, d_{k2}, \ldots, d_{km}$ being the parameters of the Dirichlet distribution used as prior.

The posterior estimates of the transition probabilities are obtained as the empirical means of the posterior densities:

$$\hat{p}_{ij} = \frac{1}{N} \sum_{n=1}^{N} p_{ij}^{(n)} \quad \text{for} \quad i, j = \{1, \ldots, m\} \tag{23}$$

with $p_{ij}^{(n)}$ being the random draw of p_{ij} at the n^{th} iteration of the MCMC algorithm.

5.3 AR and GARCH coefficient sampling

Existing MCMC algorithms for the estimation of MS-AR-GARCH models are proposed in [36] and [37]. Alternatively, it is possible to apply a MCMC algorithm for MS-GARCH models presented in [38] and include extra autoregressive terms in the mean equation, instead of a single intercept. The difference in those three algorithms lays in the sampler used for the estimation of the autoregressive and heteroscedastic coefficients. The two formers sample the posterior distributions of the model coefficients with the Metropolis-Hastings sampler (MH) whereas the latter uses the Griddy-Gibbs sampler (GG). The MH sampler [46] is based on an acceptance/rejection rule and was designed to generate samples from a target distribution. However, the rate of acceptance can turn out to be very small for complex models and slow down the convergence of the chain. As for the GG sampler [47], it is based on a principle similar to the Gibbs sampler. The key idea is to discretize the support of the parameter to be estimated. At each knot point, the likelihood of the parameter is evaluated and by a numerical integration rule, the conditional distribution of the parameter can then be approximated.

Unlike the MH sampler, the GG sampler does not require to define the analytical form of the posterior distribution a priori. It is notably useful when the conditional posterior to sample from has a complex shape (multimodality, strongly skewed, fat tails) or when one does not want to impose a shape a priori because of a lack of knowledge. Its implementation fully relies in the informativeness of the data likelihood $p(y|\boldsymbol{S}, \boldsymbol{\Theta})$ and all priors are uniform, even for short time series. Tips for implementing the GG sampler for accurate estimation of posterior distributions are given in [47]. Its main drawback is its high computational cost because of the many likelihood evaluations at each iteration but this can be overcome by parallelization of the code. Empirical results presented in [48] and [49] for the classical GARCH model are consistent and conclude that estimation methods based on the MH or the GG sampler lead to posterior estimates of similar accuracy. One of the most notable differences is that the MH sampler does not fully explore the distribution tails. This is due to the shape of the target distribution chosen which in some cases may mislead the exploration of the posterior distribution. This type of problems is avoided when estimating posterior distributions with a GG sampler because it does not require the posterior density to be known in closed form. Taking these considerations into account, it was chosen to follow

the methodology presented in [38] which uses the GG sampler for estimating MS-GARCH models. Adding extra autoregressive terms for the estimation of MS-AR-GARCH models is then straightforward.

Conditional posterior distributions of our model coefficients are derived from the Bayes' theorem. Let us consider the case of an unknown AR or GARCH coefficients that will be noted γ, and $p(\gamma)$ its prior. Its conditional posterior distribution is defined as follows:

$$p(\gamma|y, \boldsymbol{S}, \boldsymbol{\Theta}_{-\gamma}) \propto p(\gamma)p(y|\boldsymbol{S}, \boldsymbol{\Theta}) \tag{24}$$

The conditional density and cumulative distribution function (cdf) of γ are noted g_γ and G_γ. Their numerical approximation are noted $f_\gamma = f(\gamma|y, \boldsymbol{S}, \boldsymbol{\Theta}_{-\gamma})$ and F_γ, respectively. At each iteration, the GG sampler builds a numerical approximation of the conditional posterior density of each AR and GARCH coefficient. The support of γ is first discretized with n knot points $(x_1, \ldots, x_n)$. Further details on how to set up n are discussed in the next subsection. Then, the complete data likelihood $P(y|\gamma = x_i, \boldsymbol{S}, \boldsymbol{\Theta}_{-\gamma})$ is evaluated for each knot point x_i and by a numerical rule of integration, we obtain an approximation $f_\gamma(x_i)$ of the conditional density g_γ. Linear interpolation in between 2 successive knot points was found to be satisfactory in term of accuracy. Therefore, we use the trapezoidal integration method to compute f_γ. From there, approximating the cdf G_γ is direct. Finally, a random number is uniformly generated on $[0, 1]$ and by inverse transformation of F_γ, we obtain a random sample of γ. The principle of the GG sampler is graphically summarized on Figure 3. The posterior estimates of the AR and GARCH coefficients are obtained by computing the means of the posterior densities.

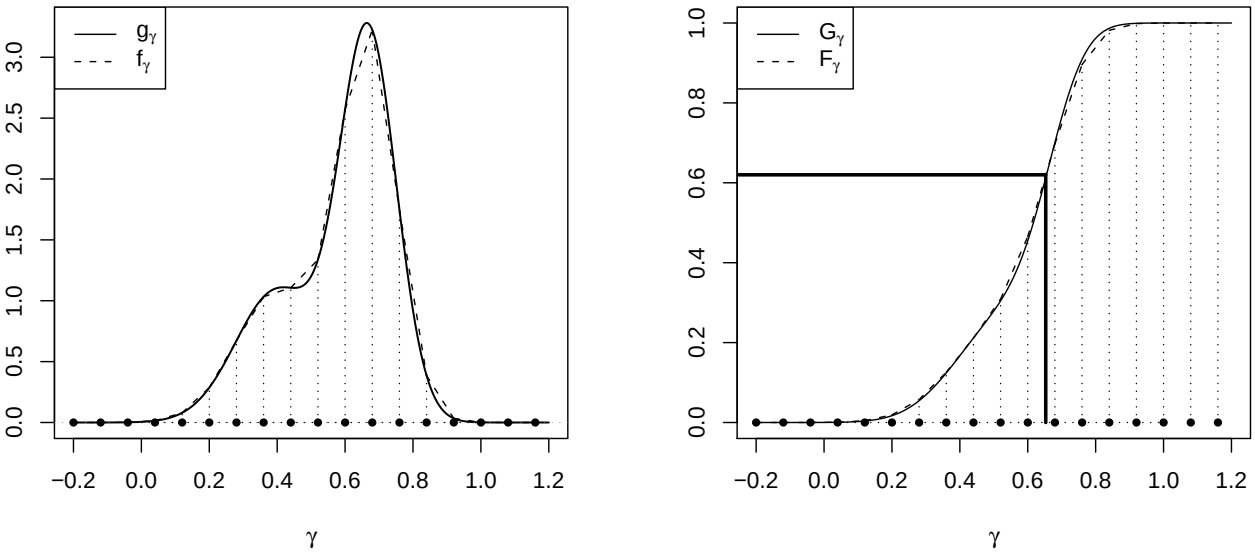

Figure 3: The conditional density g_γ of a given coefficient γ is approximated by numerical integration over a grid of points (left). An approximation F_γ of the cdf G_γ can then be computed. Finally, a random number is uniformly generated on $[0, 1]$ and by inverse transformation of F_γ, a random draw of γ is obtained (right).

5.4 Implementation details

Obvious advantages of the GG sampler are its easiness of implementation and most definitely its ability to approximate posterior densities of various shapes (skewed, multimodal and/or fat-tailed) when other samplers are more restrictive on this latter aspect. However, there is

a number of issues that have to be handled carefully for its implementation when applied to models with many parameters to be estimated as in the present study.

5.4.1 Prior distributions

First, prior distributions have to be defined for sampling the transition probabilities. For a given regime $k \in \{1, \ldots, m\}$, setting the parameters $d_{kk} > d_{ki}$ with $i \neq k$ is one way to reflect the prior knowledge that the probability of persistence (staying in the same regime) is larger than the probability of switching from regime k to i. For instance, a $B(8, 2)$ distribution is used as prior in [37] whereas a uniform $B(1, 1)$ is preferred in [38]. Several simulations with various values for the d_{ij} parameters were run on synthetic time series with more than 1000 data points. The influence of the prior distributions was noticeable for d_{ij} of very high orders of magnitude, due to the length of the time series. For instance, a $B(80, 20)$ clearly influences the posterior distribution estimates of the transition probabilities while a $B(8, 2)$ almost not, even though these 2 distributions have equal means. Arguably, we found it relatively risky to favor some regimes over others. Therefore, we favored the approach with uniform priors, meaning that $d_{k1} = d_{k2} = \ldots = d_{km} = 1$.

Second, and most important, uniform distributions are required for the GG sampler. Defining these priors consists in setting their bounds which is all the more difficult when one has very little prior knowledge of the process being considered. For each AR and GARCH coefficient, one has to make sure that the bounds of the uniform prior encompass the entire support of the true conditional density. Poor settings of the prior bounds may either prevent the convergence of the Markov chain or lead to wrong posterior density and mean estimates. One easy solution is to use a coarse-to-fine strategy for the MCMC simulation which is divided into 3 phases:

- a burn-in phase whose draws are discarded until the Markov chain reaches its stationary distribution,
- a second phase at the end of which posterior density estimates are computed and prior bounds are refined (the draws generated during this second phase are also discarded),
- a last phase with adjusted prior bounds at the end of which the final posterior densities are computed.

Refinement of the prior bounds consists in computing the posterior mean and the standard deviation of the densities. The priors are then adjusted and centered around their respective mean with their radius set to 5 standard deviations. That way the uniform priors are shrinked when they were initially too large and enlarged when too small. This approach proved to be robust enough even in case of fat-tailed posterior densities.

5.4.2 Label switching

Not least, fine settings of the prior bounds can prevent the label switching problem affecting HMM models estimated with Bayesian methods. Since posterior densities are invariant to relabeling the states, that problem can cause erroneous multimodal posterior densities. This can be circumvent by imposing structural constraints on the regimes which can be identified with the permutation sampler presented in [35]. For the specific case of MS-AR-GARCH models, the most effective constraint against label switching was set on the intercept parameters of the GARCH equation as follows: $\alpha_0^{(1)} < \alpha_0^{(2)} < \ldots < \alpha_0^{(m)}$. At each iteration, the inequality is checked and if not true, regimes are permutated. Another way to make sure that this constraint is true is to define the bounds of the uniform priors of the $\alpha_0^{(k)}$ such that they do not fully overlap.

5.4.3 Grid shape

Support discretization for the GG sampler implies choosing a suitable structure for the grid along with a fine number of knot points n. As for the structure, [47] advised to use an evolutive grid with more knot points over areas of high mass and fewer knot points over areas of low mass. Simulations on synthetic data show that this type of grid is difficult to implement in practice and that it yields relatively low gains in accuracy. The use of such a grid is not necessary in this study and instead a grid with equidistant knot points is preferred. A grid made of 42 knot points is generated for each coefficient to be estimated, with the likelihood of the 2 knot points at the extremities of the grid being set to 0, by default. This number was found sufficiently large to accurately approximate conditional densities and is comparable to the 33 knot points used in [38].

5.4.4 Mixing of the MCMC chain

MCMC simulations on synthetic time series reveal that, within a same regime, AR coefficients are strongly correlated with each others, resulting in a poorly mixing chain, slow convergence rate and significant estimation errors. The same observations were made for the GARCH parameters. In order to improve the mixing of the chain, the GG sampler is implemented with random sweeps [50]. At each iteration of the MCMC algorithm, instead of updating the AR and GARCH coefficients in a deterministic order, we generate a random permutation of the sequence $(1, \ldots, m(2+r+p+q))$ to determine which coefficients to update first, second and so on. For the empirical study on the wind power time series, it was found that the mixing of the chain could be further improved by repeating the sampling of the AR and GARCH coefficients a given number of times for every update of the state sequence. These implementation details positively enhance the well mixing behavior of the chain and lead to much sharper posterior densities (i.e. smaller estimation errors and standard deviations) of the AR and GARCH coefficients, notably.

5.4.5 Implementation summary

In order to enhance the implementation understanding and to summarize the key steps of our method, we report its structure in Algorithm 1. For the sake of the notation simplicity, let us note γ_i the i^{th} AR or GARCH coefficients of the vector of parameters $(\theta^{(1)}, \ldots, \theta^{(m)}, \alpha^{(1)}, \ldots, \alpha^{(m)})$. The vector of parameters is now noted $(\gamma_1, \ldots, \gamma_{m(2+r+p+q)})$.

5.5 Simulation on synthetic time series

Before moving on to the time series of wind power, the MCMC estimation procedure is tested on a synthetic MS-AR-GARCH process that is plotted on Figure 4 and whose coefficients are reported in Table 1. This process is composed of 2 regimes, each one of them combining an autoregressive structure of order 2 for the conditional mean equation along with a GARCH(1,1) specification for the conditional variance. The values of its coefficients are chosen so as to generate a simplistic series with two well differentiated dynamics for the 2 regimes. The values of the autoregressive coefficients are set so that the autoregressive process in each regime is stationary. The GARCH coefficients in each regime are defined so that the constraint ensuring a finite variance holds. Finally, the errors are normally distributed. The process simulated hereafter neither aims at recreating nor mimicking the wind power fluctuations presented in Section 3. It simply stands for a test case to assess the robustness and the efficiency of our estimation method.

50 series of 1500 data points are generated. Following the coarse-to-fine strategy described in the previous subsection, the bounds of the uniform prior distributions are set coarsely so

Algorithm 1 MCMC procedure for the estimation of MS-AR-GARCH models

Initialize prior distribution: $p(\gamma_1), \ldots, p(\gamma_{(m(2+r+p+q))})$
Initialize regime sequence and parameter: $\boldsymbol{S}^{(0)}, \boldsymbol{\Theta}^{(0)}$
$n = 0$
while Convergence of the Markov chain is not reached **do**
  $n = n + 1$
  for $t = 1$ to T **do**
    Sample $S_t^{(n)}$ from $p(S_t^{(n)} = k | S_1^{(n)}, \ldots, S_{t-1}^{(n)}, S_{t+1}^{(n-1)}, \ldots, S_T^{(n-1)}, \boldsymbol{\Theta}^{(n-1)}, y)$ by the single-move procedure
  end for
  Compute the Dirichlet parameters $\eta_{11}^{(n)}, \ldots, \eta_{mm}^{(n)}$
  for $k = 1$ to m **do**
    Sample $\pi_k^{(n)}$ from $D(\eta_{k1}^{(n)} + 1, \eta_{k2}^{(n)} + 1, \ldots, \eta_{km}^{(n)} + 1)$
  end for
  Generate a random permutation ρ of $\{1, \ldots, m(2 + r + p + q)\}$
  for $i = 1$ to $m(2 + r + p + q)$ **do**
    Sample $\gamma_{\rho(i)}^{(n)}$ from $p(\gamma_{\rho(i)} | \boldsymbol{S}^{(n)}, \boldsymbol{P}^{(n)}, \gamma_{\rho(1)}^{(n)}, \ldots, \gamma_{\rho(i-1)}^{(n)}, \gamma_{\rho(i+1)}^{(n-1)}, \gamma_{\rho(m(2+r+p+q))}^{(n-1)}, y)$ with the Griddy-Gibbs sampler
  end for
  if End of the second phase is reached **then**
    Adjust/update the prior distributions
  end if
end while

Table 1: Statistics on the posterior estimates for a synthetic MS(2)-AR(2)-GARCH(1,1) process, for 1 and 50 samples: Posterior means, standard deviations and coverage probabilities (CP).

			50 samples			1 sample		
	True value	Initial prior support	Posterior mean	Posterior std. dev.	CP	Refined prior support	Posterior mean	Posterior std. dev.
$\theta_0^{(1)}$	**0.5**	[-0.2 ; 1.2]	**0.500**	0.072	96%	[0.20 ; 0.78]	0.488	0.050
$\theta_1^{(1)}$	**0.5**	[-0.2 ; 1.2]	**0.502**	0.054	98%	[0.26 ; 0.72]	0.495	0.037
$\theta_2^{(1)}$	**0.2**	[-0.5 ; 0.9]	**0.197**	0.051	98%	[-0.01 ; 0.43]	0.212	0.035
$\alpha_0^{(1)}$	**0.1**	[0 ; 0.5]	**0.109**	0.041	94%	[0 ; 0.17]	0.084	0.020
$\alpha_1^{(1)}$	**0.2**	]0 ; 0.5]	**0.195**	0.068	94%	]0 ; 0.38]	0.175	0.046
$\beta_1^{(1)}$	**0.6**	[0 ; 1]	**0.593**	0.101	94%	[0.36 ; 0.88]	0.621	0.059
$\theta_0^{(2)}$	**0**	[-0.7 ; 0.7]	**-0.015**	0.041	94%	[-0.44 ; 0.36]	-0.038	0.100
$\theta_1^{(2)}$	**0.7**	[0 ; 1.4]	**0.689**	0.081	98%	[0.55 ; 0.99]	0.764	0.051
$\theta_2^{(2)}$	**-0.3**	[-1 ; 0.2]	**-0.308**	0.081	98%	[-0.59 ; -0.17]	-0.381	0.052
$\alpha_0^{(2)}$	**0.4**	[0.1 ; 0.8]	**0.512**	0.189	98%	[0 ; 0.82]	0.373	0.105
$\alpha_1^{(2)}$	**0.1**	]0 ; 0.5]	**0.114**	0.073	92%	]0 ; 0.33]	0.135	0.041
$\beta_1^{(2)}$	**0.85**	[0 ; 1]	**0.813**	0.087	96%	[0.62 ; 1[	0.831	0.044
p_{11}	**0.98**	]0 ; 1[	**0.977**	0.009	90%	]0 ; 1[	0.983	0.005
p_{22}	**0.96**	]0 ; 1[	**0.950**	0.023	92%	]0 ; 1[	0.961	0.012

as not to be too informative on the true coefficient values. The goal is to check whether the MCMC method is robust enough not to get trapped by local minima. The coefficients

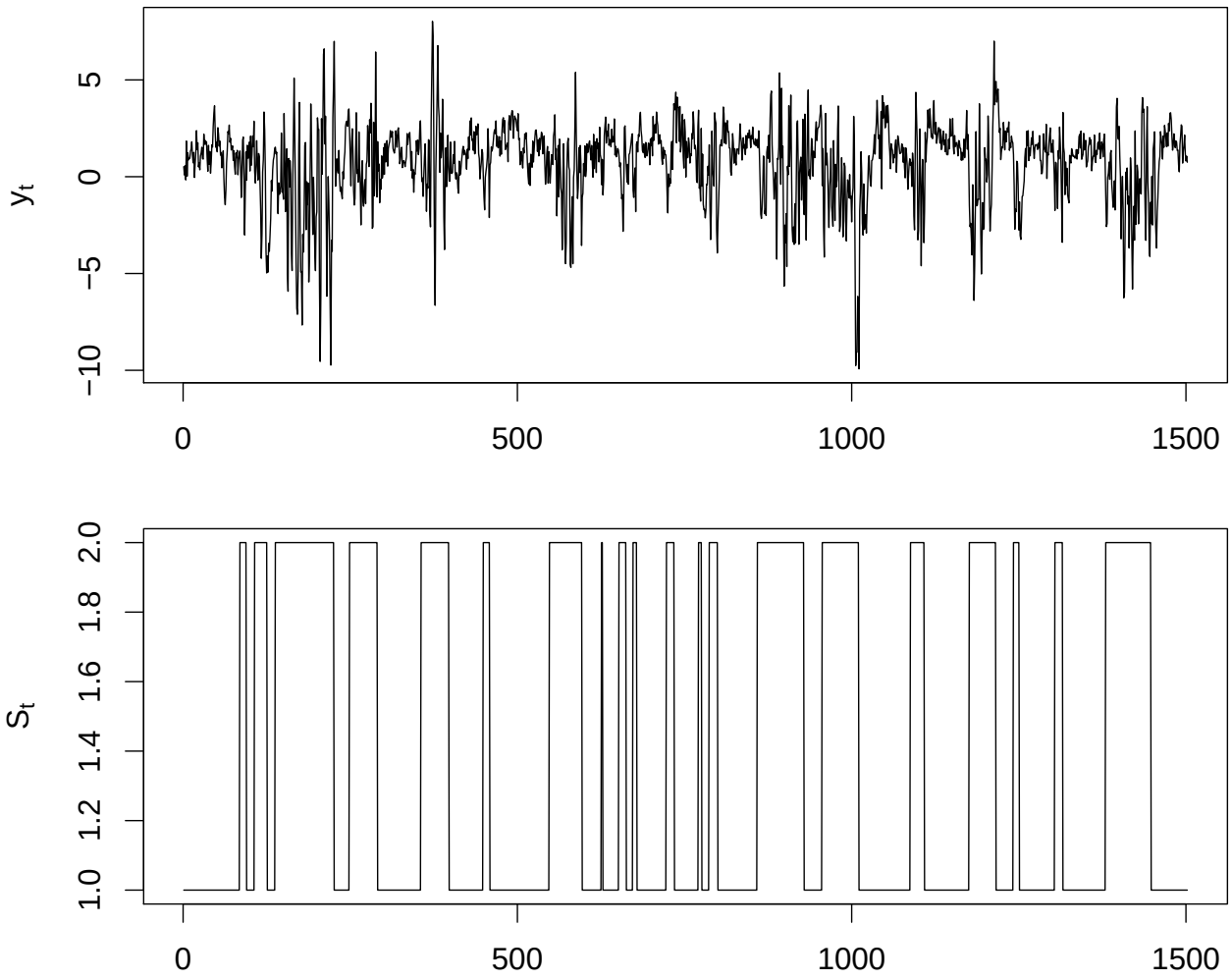

Figure 4: Simulation of a MS(2)-AR(2)-GARCH(1,1) whose coefficients and transition probability values are given in Table 1. Top: simulated process $y = (y_1, \ldots, y_T)$. Bottom: regime sequence $\boldsymbol{S} = (S_1, \ldots, S_T)$.

supports are then discretized with 42 equidistant points. Starting values for the regime sequence and all 16 parameters are randomly initialized within the range of possible values defined by their respective prior support. 50000 iterations of the MCMC algorithm are run of which the last 30000 iterations are used for posterior inference, the first 10000 being discarded as burn-in and the second 10000 being used to refine the prior supports. For each simulation, convergence of the chain is assessed with the diagnostic proposed in [51] by running 3 chains in parallel, with different starting values. No evidence of non-convergence was noticed. When considering single sample, large estimation bias can be observed on both AR and GARCH coefficients. More satisfactorily, when considering 50 samples, absolute estimation errors for all parameters are smaller than their corresponding posterior standard deviations. As observed in [37], the largest estimation errors are found for the posterior distributions of the GARCH coefficients whereas AR coefficients are estimated with a much higher accuracy. In each of the two regimes, β_1 is biased downwards and α_0 is biased upwards, which is a well-known issue with MS-GARCH models. For a given parameter, the coverage probability (CP) correspond to the probability of its true value being encompassed within the interval defined by the 2.5% and 97.5% quantiles of its posterior distribution. In other words, these probabilities are the nominal 95% confidence intervals of the posterior estimates. Large deviations could indicate recurrent failure of the estimation method for

some parameters. Globally, the estimated CP are all close to 95% and no large deviation is observed which is satisfactory. The grid refinement procedure shows that the supports of the AR coefficients are significantly smaller than the initial supports coarsely set. As for the final supports of GARCH coefficients, they consist of small adjustments of their initial supports. The verification for label switching is performed by analyzing the full posterior densities displayed on Figure 5 where no bimodality is observed. We can also add that the sampler performs quite well in terms of mixing since the densities are rather peaky and have small tails.

Inference on the regime sequence can also be performed. However, methods for global decoding such as the Viterbi algorithm [52] are not applicable to MCMC outputs since the sole smoothed probabilities of the regime sequence can be computed. Instead, we use a simple labelling rule to infer the regime sequence: state variables with a smoothed probability of being in regime k larger than 0.5 are classified as being in regime k. Following that rule, we can compute the successful regime inference rate and the probability of regime retrieval (the probability of the true regime being k knowing that the inferred regime is k). Results are reported in Table 2. Ideally, these quantities should be as close to 1 as possible. The rate of successful inference is higher for regime 1 (96%) than for regime 2 (90%). The same result holds for the probability of successful regime retrieval. These results are reasonably good according to the complexity of the model dynamics. Three of the model features may explain these differences: (i) regime 1 is characterized by a higher persistence probability that regime 2 ($p_{11} > p_{22}$), (ii) the unconditional variance ($\sigma^{(k)} = \frac{\alpha_0^{(k)}}{1-\alpha_1^{(k)}-\beta_1^{(k)}}$) in regime 1 ($\sigma^{(1)} = 0.5$) is lower than in regime 2 ($\sigma^{(2)} = 8$) and (iii) persistence of shocks measured by $\alpha_1^{(k)} + \beta_1^{(k)}$ is also lower in regime 1 than in regime 2. The higher persistence probability makes that parameters defining the first regime can be estimated over a larger number of data points and over longer time intervals clear off any structural breaks, on average, which leads to more accurate posterior estimates. The lower unconditional variance combined to the lower persistence to shocks in regime 1 makes that the autoregressive and the conditional variance dynamics are easier to identify and separate. These latter comments are confirmed by the estimated posterior standard deviations of the model parameters (see Table 1) which are smaller in regime 1 than in regime 2, for corresponding parameters.

Table 2: Statistics on the inferred regime sequence.

Rate of successful regime inference	Probability of regime retrieval
$P(\widehat{S}_t = 1 \mid S_t = 1) = 0.96$	$P(S_t = 1 \mid \widehat{S}_t = 1) = 0.95$
$P(\widehat{S}_t = 2 \mid S_t = 2) = 0.90$	$P(S_t = 2 \mid \widehat{S}_t = 2) = 0.91$

5.6 Study on an empirical time series of wind power

One of the main issue that arises when fitting Markov-Switching models to an empirical time series is the determination of the number of states m of the Markov chain. Theoretically, its determination is not to be separated of the autoregressive and conditional variance structure (orders r, p and q in equations 1 and 2). Along that idea, [53] review different penalized likelihood criteria for the joint determination of the number of hidden states and autoregressive order for MSAR models. However, in practise, misspecification in the parametrization of the model may result in over estimating the optimal number of regimes. For instance, ignored volatility clustering effects can falsely be reported as regime-switching effects [54].

The model identification approach taken in this study is to define the autoregressive and conditional variance orders a priori and determine the optimal number of regimes accordingly. Most studies involving Markov-Switching test for a limited number of regimes, from 1 to 4. The underlying theoretical reason is that regime switchings occur infrequently. The more practical reason is that the number of parameters to be estimated grows quadratically with respect to the number of regimes and constraints for regime identification become more difficult to define.

One reason to proceed that way and not by computing the Bayesian Information Criterion is that there is no method for computing the marginal likelihood of MS-GARCH models to our knowledge. An empirical cross-validation procedure is used instead. The time series of interest is the one presented in Section 3 for which measurements from the Horns Rev 1 wind farm are averaged over 10 minute intervals. All available observations from August 2005 (i.e. 4125 observations) are used for estimating the posterior distributions of the MS-AR-GARCH model. Several parametrizations with respect to m, r, p and q are tested. Then, all available observations from September 2005 (i.e. 4320 observations) are used for cross-validation and the parametrization resulting in the best one-step ahead Continuous Ranked Probability Score [10] was chosen. The best performances were obtained for models with 3 autoregressive lags and a GARCH(1,1) structure for the conditional variance in each regime. The autoregressive order is in agreement with previous studies on the same data set [15, 55]. To keep the computational complexity and burden reasonable, only models defined with 1 and 2 regimes were tested. Furthermore, no constraint for regime identification could be found for a number of regimes larger than 2. Posterior estimates for MS(m)-AR(3)-GARCH(1,1) with $m = 1$ and $m = 2$ are reported in Table 3. Posterior densities for the MS(2)-AR(3)-GARCH(1,1) are shown on Figure 7.

One of the reason why we prefer the GG over the MH sampler is that it can estimate posterior densities of various shape without prior knowledge of their closed form. From Figure 7, it can be noticed that the posterior densities of the GARCH equation are asymmetric, more notably in regime 2. This is due to the constraints imposed in (4) and (5) and the asymmetry becomes stronger as the posterior mean of a given parameter is close to the bounds of the constraints. $\alpha_0^{(1)}$ is numerically close to 0 and its posterior density has the shape of a mass point. Omitting this parameter for fitting the model makes the regimes less stable and it is decided to keep it in the formulation of the MS(2)-AR(3)-GARCH(1,1) model. The posterior densities of the AR equation have symmetric shapes. However, they are characterized by large posterior standard deviations and rather flat shapes which is the consequence of the strong autocorrelation between coefficients within a same regime, as mentioned earlier in this Section. That problem was neither encountered in our simulations on synthetic data nor in other studies such as [37], [38] or [36] since the parametrization of the conditional mean equation is restricted to one lag at most. Since it may affect the final posterior mean estimates used for prediction, further research will be dedicated to investigate potential techniques to overcome it.

In addition, analyzing the posterior estimates of our model may reveal interesting features on the very short-term wind power fluctuations of the Horns Rev 1 wind farm. The low (respectively high) frequency wind power fluctuations are captured by the AR (respectively GARCH) coefficients of the model and different profiles of fluctuations are expected across regimes. In addition, transition probability estimates may indicate whether one regime is more persistent over time than the other.

Regarding the model with one regime, AR(3)-GARCH(1,1), we report its posterior estimates in order to illustrate the transition from a single regime model to a two regime model and appraise how the posterior estimates of the 2 regime model may relate to those of the single regime model. Initial prior bounds were defined based on the estimates obtained by numerical maximization of the likelihood function (NML). The posterior estimates of the AR

coefficients are in close agreement with those obtained by NML while the posterior estimates of the GARCH coefficients deviate more. After verification, this can be due to a bimodality on the posterior density of the α_0 coefficient which makes that its estimated posterior mean is larger than the one estimated by NML. These results are not presented here in order to save space but are available upon request.

As for the MS(2)-AR(3)-GARCH(1,1), the autoregressive dynamics are rather similar in the two regimes but for the intercept terms $\theta_0^{(1)}$ and $\theta_0^{(2)}$ which confirms the earliest results in [15]. More interestingly, the dynamics of the conditional variance in the two regimes differ in several ways. First, the intercept terms in regime 1 is significantly lower than in regime 2 ($\alpha_0^{(1)} \ll \alpha_0^{(2)}$) which means that regime 2 can be interpreted as the regime for which the amplitude of the wind power fluctuations are the largest. Then the posterior mean estimates of the GARCH coefficients in regime 1, $\alpha_1^{(1)}$ and $\beta_1^{(1)}$ are approximately equal which indicates that small prediction errors are followed by fast decreases of the conditional variance value while large errors give rise to sudden explosions. In regime 2, $\beta_1^{(2)} \gg \alpha_1^{(2)}$ makes that the conditional variance level is more stable between successive observations and has a longer memory of large errors. Finally, one can also notice that $p_{11} > p_{22}$ which translates into regime 1 being more persistent than regime 2 (i.e. periods of low volatility last longer than periods of high volatility).

An illustration of the estimated sequence of smoothed probabilities for the MS-AR-GARCH model is given on Figure 6. In particular, it depicts the smoothed probabilities of being in regime 1. It can be noticed that the 2 regimes do not seem to be well separated but for periods where the wind power generation is null or close to its nominal capacity P_n, with smoothed probabilities close to 1. Even though a clear separation of the regimes is a very desirable feature, it does not automatically translate into a loss of predictive power of the Markov-Switching model. This aspect will be further addressed in the next Section of this study.

First, simulations on synthetic data have allowed us to design and tune our estimation method for MS-AR-GARCH models. Then, its applicability to an empirical time series of wind power is tested and demonstrated a good ability to estimate posterior densities of various shapes despite some limitations regarding the posterior densities of the autoregressive coefficients. Nevertheless, our will is not to identify the best class of models for the modeling of very short-term wind power fluctuations but rather to investigate new alternatives such as the proposed MS-AR-GARCH model for (i) providing additional insights on these wind power fluctuations and (ii) investigating on their potential predictive power.

6 Wind power forecast evaluation

Forecasting wind power fluctuations of large offshore wind farms at a time scale of a few minutes is a relatively new and difficult challenge. The difficulty stems from the lack of meteorological observations in the neighborhood of the wind farm. The consequences are that state-of-the-art models often fail in predicting wind power fluctuations of large amplitude caused by sudden changes in the weather conditions nearby the wind farm. In practise, naive forecasts are difficult to significantly outperform [14].

The literature on short-term wind power forecasting is abundant and a recent overview is available in [56]. Originally, the quality and accuracy of statistical forecasts of wind power were evaluated with respect to point prediction scores. From a decision making perspective, the drawback of such an approach is that it clearly neglects the uncertainty associated with the forecast, often leading to sub-optimal control strategies. Therefore, quantifying the probability of all potential outcomes greatly enhances the usefulness of wind power forecasts [57]. These probabilistic forecasts can either take the form of density functions or

Table 3: Statistics on the posterior estimates of the AR(3)-GARCH(1,1) and MS(2)-AR(3)-GARCH(1,1) model fitted to the time series of wind power.

	1 Regime: AR(3)-GARCH(1,1)				2 Regimes: MS(2)-AR(3)-GARCH(1,1)			
	Initial prior support	Refined prior support	Posterior mean	Posterior std. dev.	Initial prior support	Refined prior support	Posterior mean	Posterior std. dev.
$\theta_0^{(1)}$	[-0.01 ; 0.01]	[-0.007 ; 0.006]	-2.10^{-4}	0.002	[-0.04 ; 0.04]	[-0.004 ; 0.004]	$\mathbf{-3.10^{-5}}$	6.10^{-4}
$\theta_1^{(1)}$	[1 ; 1.7]	[0.68 ; 2.11]	1.358	0.232	[1 ; 1.8]	[0.64 ; 2.18]	**1.417**	0.273
$\theta_2^{(1)}$	[-0.85 ; -0.05]	[-1.33 ; 0.34]	-0.460	0.284	[-0.95 ; -0.15]	[-1.36 ; 0.21]	**-0.574**	0.304
$\theta_3^{(1)}$	[-0.15 ; 0.35]	[-0.52; 0.72]	0.107	0.206	[-0.35 ; 0.55]	[-0.67 ; 0.99]	**0.156**	0.300
$\alpha_0^{(1)}$	$[0 ; 3.10^{-4}]$	$[0 ; 3.10^{-4}]$	7.10^{-5}	6.10^{-5}	$[5.10^{-6} ; 10^{-4}]$	$[2.10^{-6} ; 10^{-5}]$	$\mathbf{3.10^{-6}}$	2.10^{-7}
$\alpha_1^{(1)}$	[0.2 ; 1[	[0.03 ; 1[	0.513	0.161	]0 ; 1[	[0.23 ; 0.74]	**0.499**	0.077
$\beta_1^{(1)}$	[0 ; 0.7]	[0 ; 0.95]	0.467	0.161	[0 ; 1[	[0.25 ; 0.74]	**0.489**	0.074
$\theta_0^{(2)}$	-	-	-	-	[-0.06 ; 0.10]	[-0.04 ; 0.09]	**0.011**	0.013
$\theta_1^{(2)}$	-	-	-	-	[0.7 ; 1.7]	[0.27 ; 2.02]	**1.178**	0.285
$\theta_2^{(2)}$	-	-	-	-	[-0.7 ; 0.3]	[-1.22 ; 0.58]	**-0.323**	0.341
$\theta_3^{(2)}$	-	-	-	-	[-0.4 ; 0.6]	[-0.76 ; 1.01]	**0.126**	0.284
$\alpha_0^{(2)}$	-	-	-	-	$[1.10^{-3} ; 8.10^{-3}]$	$[0 ; 4.10^{-3}]$	$\mathbf{5.10^{-4}}$	3.10^{-4}
$\alpha_1^{(2)}$	-	-	-	-	]0 ; 1[	]0 ; 0.54]	**0.079**	0.080
$\beta_1^{(2)}$	-	-	-	-	[0 ; 1[	[0 ; 1[	**0.892**	0.088
p_{11}	-	-	-	-	]0 ; 1[	]0 ; 1[	**0.913**	0.029
p_{22}	-	-	-	-	]0 ; 1[	]0 ; 1[	**0.783**	0.114

prediction intervals when numerically approximated and should preferably be evaluated with respect to their calibration and sharpness [10]. Accurate quantification of the uncertainty associated with a point forecast is an information as valuable as the value of the forecast itself. It could first assist wind farm operators in anticipating the risks of unexpected wind power fluctuations when point forecast fail in doing so. And, ultimately, it could help them in determining backup strategies based on available energy reserves.

One of the drawbacks of MS-GARCH models is that the conditional variance becomes intractable with the addition of autoregressive terms in the model formulation. This stands as a clear limitation for the use of such class of models for prediction applications. To bypass that problem, the approach chosen in [37] is to repeat the estimation of the model over a sliding window and generate one-step ahead forecasts based on the new set of estimates. We think that this approach is too computationally intensive and instead, we prefer to use the recursive update formula of the conditional variance as presented by Gray in [24].

6.1 Approximating the conditional variance for prediction applications

The formula developed in [24] recursively approximates the conditional variance as the weighted average of past conditional variances. One of its advantages is that it is flexible and it can be extended to include autoregressive terms. One may then argue and wonder why we did not use that formula to estimate our MS-AR-GARCH model. We did investigate the possibility of using it with an estimation method based on numerical maximization of the Likelihood function. Nevertheless, the complexity of the Likelihood function made that parameter either ended up on the bounds of the constraints (4) and (5) or convergence could

not be reached which prevented its use for the estimation step of the study.

For a MS(m)-AR(r)-GARCH(1,1) model, the approximated conditional variance at time t, h_t, is defined as follows:

$$h_t = E[y_t^2|y_{[1,t-1]}, \boldsymbol{\Theta}] - E[y_t|y_{[1,t-1]}, \boldsymbol{\Theta}]^2 \tag{25}$$

First, the term $E[y_t|y_{[1,t-1]}, \boldsymbol{\Theta}]$ is the optimal one-step predictor and, under normality conditions, can be calculated as the weighted sum of the predictions in each regime:

$$E[y_t|y_{[1,t-1]}, \boldsymbol{\Theta}] = \hat{y}_{t|t-1} = \sum_{k=1}^{m} \hat{\xi}_{t|t-1}^{(k)} (\theta_0^{(k)} + \sum_{i=1}^{r} \theta_i^{(k)} y_{t-i}) \tag{26}$$

Second, the term $E[y_t^2|y_{[1,t-1]}, \boldsymbol{\Theta}]$ can be computed as follows:

$$E[y_t^2|y_{[1,t-1]}, \boldsymbol{\Theta}] = \sum_{k=1}^{m} \hat{\xi}_{t|t-1}^{(k)} (h_t^{(k)} + (\theta_0^{(k)} + \sum_{i=1}^{r} \theta_i^{(k)} y_{t-i})^2) \tag{27}$$

with $h_t^{(k)}$ the one-step ahead predicted conditional variance in regime k computed as follows:

$$h_t^{(k)} = \alpha_0^{(k)} + \alpha_1^{(k)} \varepsilon_{t-1}^2 + \beta_1^{(k)} h_{t-1} \tag{28}$$

and $\hat{\xi}_{t|t-1}^{(k)}$ the predictive probability of being in regime k at time t, given all information available at time $t-1$. The vector of predictive probabilities $\hat{\xi}_{t|t-1} = [\hat{\xi}_{t|t-1}^{(1)}, \ldots, \hat{\xi}_{t|t-1}^{(m)}]^T$ can be computed in a recursive manner as follows:

$$\hat{\xi}_{t|t-1} = \boldsymbol{P}^T \hat{\xi}_{t-1|t-1} \tag{29}$$

with $\hat{\xi}_{t-1|t-1} = [\hat{\xi}_{t-1|t-1}^{(1)}, \ldots, \hat{\xi}_{t-1|t-1}^{(m)}]^T$ the vector of filtered probabilities at time $t-1$ whose elements can be computed as follows:

$$\hat{\xi}_{t-1|t-1}^{(k)} = \frac{\hat{\xi}_{t-1|t-2}^{(k)} \times f(y_{t-1}|S_{t-1} = k, y_{[1,t-2]}, \boldsymbol{\Theta})}{\sum_{k=1}^{m} \hat{\xi}_{t-1|t-2}^{(k)} \times f(y_{t-1}|S_{t-1} = k, y_{[1,t-2]}, \boldsymbol{\Theta})} \tag{30}$$

where $f(y_{t-1}|S_{t-1} = k, y_{[1,t-2]}, \boldsymbol{\Theta})$ is the conditional density of y_{t-1} given the set of information available at time $t-2$.

We are aware that the approximation presented here above is not optimal for prediction applications since it may introduce a permanent bias in the computation of the conditional variance. It is a choice governed by the necessity to bypass a problem not yet solved and to minimize its computational cost. It could then be expected that the prediction skills of our model would benefit from advances towards a better tracking of the conditional variance for MS-AR-GARCH models. As for now, we can proceed to the evaluation of the prediction skills of our model.

6.2 Evaluation of point forecasts

The out-of-sample predictive power of our MS-AR-GARCH model is evaluated based on its performance on one-step ahead forecasts. Point forecast skills are first considered and compared to common benchmark models for very short-term wind power fluctuations as well as state-of-the-art models. Common benchmark models include persistence (i.e. $\hat{y}_t = y_{t-1}$) and the simple but robust AR model. State-of-the-art models include the class of MSAR models as initially applied to wind power time series in [14]. MSAR models were not estimated with the method presented in the previous Section since more robust estimation methods exist

for that type of models. Instead, they were estimated by numerical maximization of the Likelihood function. Following the standardized framework for the performance evaluation of wind power forecasts discussed in [17], the proposed score functions to be minimized are the Normalized Mean Absolute Error (NMAE) and Root Mean Square Error (NRMSE). A higher importance is given to the NRMSE over the NMAE in the final evaluation of point forecast skills because the RMSE is a quadratic score function and is more likely to highlight the power of a given model to reduce large errors. Reducing these large prediction errors is indeed a very desirable ability of prediction models that we aim at developing. The out-of-sample evaluation is performed over more than 21000 data points of which more than 3000 are missing (from September 2005 to January 2006). The optimal parametrization for each of the models cited here above was defined by cross validation in the same way as for the MS-AR-GARCH model. NMAE and NRMSE scores are computed for all models and reported in Table 4 and 5. For Markov-Switching models, the optimal one-step ahead predictor is given by equation (26).

Table 4: NMAE score given in percentage of the nominal capacity of the Horns Rev 1 wind farm. Results are given for persistence, an AR model with 3 lags AR(3), a MSAR model with 2 regimes and 3 lags in the conditional mean equation MSAR(2,3), a MSAR model with 3 regimes and 3 lags in the conditional mean equation MSAR(3,3), an AR-GARCH model with 3 lags in the conditional mean equation and a GARCH(1,1) specification for the conditional variance, and finally for the MS-AR-GARCH model estimated in Section 5.

	Sept.	Oct.	Nov.	Dec.	Jan.	Total
Persistence	2.50	2.41	2.58	3.01	2.47	2.55
AR(3)	2.44	2.36	2.64	2.98	2.46	2.53
AR(3)-GARCH(1,1)	2.39	2.29	2.60	2.95	2.41	2.49
MS(2)-AR(3)-GARCH(1,1)	2.38	2.27	2.50	2.89	2.38	2.44
MSAR(2,3)	2.38	2.28	2.49	2.89	2.37	2.44
MSAR(3,3)	2.36	2.26	2.49	2.89	2.36	2.42

Table 5: NRMSE score given in percentage of the nominal capacity of the Horns Rev 1 wind farm. Results are given for the same models as for the NMAE.

	Sept.	Oct.	Nov.	Dec.	Jan.	Total
Persistence	4.66	4.17	6.22	5.76	4.28	5.02
AR(3)-GARCH(1,1)	4.50	4.00	6.18	5.72	4.24	4.93
AR(3)	4.45	3.98	5.99	5.56	4.17	4.83
MS(2)-AR(3)-GARCH(1,1)	4.43	3.96	6.00	5.55	4.15	4.82
MSAR(2,3)	4.43	3.98	5.95	5.55	4.17	4.81
MSAR(3,3)	4.42	3.96	5.95	5.55	4.17	4.80

As it could have been expected, MSAR models, with 2 or 3 regimes, outperform all other models for both the NMAE and NRMSE. The best improvement in NMAE over persistence is about 5.1% while it is 4.4% for the NRMSE. These levels of improvement agree with earlier results in [14] and [55]. If moving from AR to MSAR models leads to appreciable improvements, moving from AR to AR-GARCH models results in the opposite effect. However, moving from single regime AR-GARCH to regime switching AR-GARCH has a significant

positive effect, more notably for the NRMSE. The relatively good performances of the MS-AR-GARCH model are comparable to those of the MSAR model with 2 regimes. All these results tend to indicate that the MSAR class of models, explicitly designed to capture regime switching and autocorrelation effects, has better point prediction skills.

If accounting for heteroscedastic effects in regime switching models makes that part of the dynamics originally captured by the AR component of MSAR models is instead captured by the GARCH component and results in lower performances in point forecasting. It can then be expected that this will translate into better performances for probabilistic forecasts of models explicitly designed to capture the heteroscedastic effects such as the AR-GARCH and MS-AR-GARCH models.

6.3 Evaluation of interval and density forecasts

Probabilistic forecasts are very useful in the sense that they provide us with a measure of the uncertainty associated with a point forecast. They can either take the form of density or interval forecasts. For their evaluation we follow the framework presented in [58].

First, we consider the overall skill of the probabilistic forecasts generated by the proposed MS-AR-GARCH model. The traditional approach consists in evaluating the calibration and sharpness of the density forecasts. The calibration of a forecast relates to its statistical consistency (i.e. the conditional bias of the observations given the forecasts). As for the sharpness of a forecast, it refers to its concentration or, in other words, to its variance. The smaller the variance, the better, given calibration. One score function known to assess both the calibration and sharpness of density forecasts simultaneously is the Continuous Ranked Probability Score (CRPS). The exercise consists in generating one-step ahead density forecasts. For the single regime model, these density forecasts take the form of Normal density functions while for Markov-Switching models, they takes the form of mixtures of conditional Normal distributions weighted by the predictive probabilities of being in each of the given regime. The CRPS criterion is computed for the same models as for the point prediction exercise and the results are reported in Table 6.

Table 6: CRPS criterion given in percentage of the nominal capacity of the Horns Rev 1 wind farm. Results are given for the same models as for the point prediction exercise.

	Sept.	Oct.	Nov.	Dec.	Jan.	Total
AR(3)	2.08	1.99	2.33	2.48	2.02	2.15
MSAR(2,3)	1.89	1.81	2.01	2.26	1.88	1.94
MSAR(3,3)	1.85	1.78	1.98	2.24	1.85	1.91
AR(3)-GARCH(1,1)	1.84	1.76	1.99	2.24	1.85	1.91
MS(2)-AR(3)-GARCH(1,1)	1.83	1.76	1.95	2.20	1.83	1.88

From Table 6, it can noticed that the proposed MS-AR-GARCH model has the best overall skill. Its improvement over AR models is about 12.6%. More generally, GARCH models outperform non GARCH models even though the improvements are very small in some cases. The relatively good performance of the MSAR model with 3 regimes tend to indicate that the volatility clustering effect captured by GARCH models may partly be captured as a regime switching effect by MSAR models. This may appear as a paradox but it is not, in our opinion. As noticed in [15], the respective dynamics in the three regimes of the MSAR model can be more easily characterized with respect to the values of their respective variance rather than their respective conditional mean dynamics. While GARCH models are explicitly designed for capturing the heteroscedastic effect, the formulation of MSAR models

Table 7: Nominal coverage rates and Empirical coverage rates of interval forecasts generated by the following three models: AR(3), MSAR(3,3) and MS(2)-AR(3)-GARCH(1,1). The coverage rates are expressed in %.

Nom. cov.	Emp. cov AR(3)	Emp. cov. MSAR(3,3)	Emp. cov. MS(2)-AR(3)-GARCH(1,1)
10	13.2	07.1	09.4
20	42.6	25.8	20.7
30	55.5	35.2	31.3
40	64.3	43.9	42.3
50	71.4	52.4	63.2
60	77.2	60.3	71.2
70	81.6	68.8	78.1
80	89.9	77.7	84.4
90	90.0	86.9	90.0

makes that the same effect can be captured in an implicit manner by the combination of several dynamics with different variances. The consequence of these findings is that MS-AR-GARCH models which combine both a Markov-Switching and GARCH formulation are not very powerful for separating the regimes (see Figure 6) since there may be a conflict in their formulation. However, it does not automatically affect their predictive power since a clear separation of the regimes may not automatically translate into better prediction skills. Instead, it is reflected in a more parsimonious parametrization of the MS-AR-GARCH models regarding the optimal number of regimes.

In order to better evaluate the contribution of the calibration to the overall skill of probabilistic forecasts, one can compare the empirical coverage rates of intervals forecasts to the nominal ones. Intervals forecasts can be computed by means of two quantiles which define a lower and an upper bound. They are centered around the median (i.e. the quantile with nominal proportion 0.5). For instance, the interval forecast with a coverage rate of 0.8 is defined by the two quantiles with nominal proportion 0.1 and 0.9. Empirical coverage rates of interval forecasts generated from an AR, MSAR and MS-AR-GARCH are computed and reported in Table 6.3. Recurrent and large positive deviations are observed for the interval forecasts generated from the AR model, indicating that the intervals are too wide. In contrast, the empirical coverage rate of the interval forecasts generated from the MSAR model exhibit a relatively good match with the nominal coverage rates. The maximum deviation is around 6%. While these intervals seem too wide for small nominal coverage rates (i.e. from 10 up to 50%), they become too narrow for large nominal coverages. As for the intervals generated from the MS-AR-GARCH models, the agreement is excellent for the smallest nominal coverage rates (i.e. from 10 up to 40%) and the largest one (i.e. 90%) whereas it significantly deviates from the nominal coverage of intermediate widths. This latter result may be the consequence of a bias introduced by the approximation of the conditional variance as presented earlier. This also tends to indicate that the relatively good overall skill of probabilistic forecasts generated from MS-AR-GARCH models are more likely to be the result of sharp forecasts rather than consistent.

7 Discussion and concluding remarks

We presented a general model formulation for the modeling and forecasting of very-short term wind power fluctuations at large offshore wind farms. The dynamics of these fluctuations

are very complex and developing models for prediction applications is an ongoing challenge within the wind power community. The interest of the proposed MS-AR-GARCH model is that it extends the state-of-the-art methodology based on MSAR models and specifies the conditional variance in each regime as a GARCH model in order to better account for heteroscedastic effects. This calls for an advanced estimation method to overcome the problem linked to the historical path dependency of the conditional variance. In that regard, Bayesian methods offer an alternative framework to methods based on Maximum Likelihood Estimation. In particular, they allow to break down the complexity of the global estimation problem into a set of smaller problems more easily handleable.

In a first stage, we gave a thorough introduction on the estimation method based on a MCMC algorithm. Then, we addressed its practical implementation issues in details. In a second stage, the estimation method for the proposed MS-AR-GARCH model was tested on both synthetic and empirical time series. It proved to apply successfully on synthetic time series. The results on the empirical time series of wind power are more mixed. In particular, the method encountered clear problems to deal with the high correlation of the AR coefficients of the model which resulted in rather flat posterior densities. On the opposite, it seemed to work well for the other model parameters (i.e. GARCH coefficients and transition probabilities). In that respect, directions for future research could include the investigation of more appropriate sampling methods for the AR coefficients.

The predictive ability of the MS-AR-GARCH model was evaluated on a one-step ahead forecasting exercise of wind power time series sampled over a 10 minute intervals. Empirical comparisons of its performances against common benchmark and state-of-the-art models showed that (i) it is slightly outperformed by MSAR models for point forecasts according to NMAE and NRMSE score functions, (ii) it outperforms all other models in terms of overall skill of probabilistic forecasts evaluated with respect to the CRPS criterion. However, these results need to be put into a broader perspective. First, both point forecast improvements of MSAR and MS-AR-GARCH models over the simple but robust AR model are very small for the NRMSE score function while they are larger for the NMAE score function. This tends to indicate that Markov-Switching models contribute to reduce point forecast errors over periods where the wind power fluctuations are characterized by small rather than large amplitude. Second, and more interestingly, all three MSAR, AR-GARCH and MS-AR-GARCH models are able to capture periods characterized by different volatility levels of wind power fluctuations at the Horns Rev 1 wind farm. For the time being and in the absence of meteorological observations to explain the origin of the volatility, these models do not have the ability to anticipate the most abrupt changes in the dynamics of the wind power fluctuations. In contrast, future approaches based on the integration of observations of local weather conditions are likely to fill in that gap. A first step was achieved in [55] with the integration of on-site wind speed and direction measurements into prediction models, resulting in appreciable improvements of wind power fluctuation predictability. An other lead was given in [19] with the observations of convective rain cells during episodes of extreme wind speed variability. Following these observations, a weather radar capable of measuring rain reflectivity at high spatio temporal resolution is currently operated at the offshore site of Horns Rev in order to provide additional insights on these wind power fluctuations and help improving their predictability.

8 Acknowledgments

The present study was supported by the "SafeWind" project (ENK7-CT2008-213740) and the Danish Public Service Obligation (PSO) fund under the projects "Mesoscale atmospheric variability and the variation of wind and production for offshore wind farms" (contract

PSO-7141) and "Radar@Sea" (contract no. 2009-1-0226) which are hereby acknowledged. Vattenfall is greatly acknowledged for sharing the wind power data for the Horns Rev 1 wind farm.

References

[1] Danish Energy Agency. Energy statistics 2007, October 2008. [Available at: www.ens.dk].

[2] S.C. Pryor and R.J. Barthelmie. Comparison of potential power production at on-and offshore sites. *Wind Energy*, 4:173–181, 2002.

[3] M. Lange and U. Focken. *A Physical Approach to Short-term Wind Power Prediction*. Springer, 2005.

[4] V. Akhmatov. Influence of wind direction on intense power fluctuations in large offshore wind farms in the North Sea. *Wind Engineering*, 31:59–64, 2007.

[5] U. Focken, M. Lange, K. Mönnich, H-P Wald, G. Beyer, and A. Luig. Short term prediction of the aggregated power output of wind farms - a statistical analysis of the reduction of the prediction error by spatial smoothing effects. *Journal of Wind Engineering and Industrial Aerodynamics*, 90:231–246, 2002.

[6] V. Akhmatov, C. Rasmussen, P. B. Eriksen, and J. Pedersen. Technical aspects of status and expected future trends for wind power in Denmark. *Wind Energy*, 10:31–49, 2007.

[7] P. Sørensen, A. Cutululis, A. Vigueras-Rodriguez, H. Madsen, P. Pinson, L.E. Jensen, J. Hjerrild, and M.H. Donovan. Modelling of power fluctuations from large offshore wind farms. *Wind Energy*, 11:29–43, 2008.

[8] C. Vincent, G. Giebel, P. Pinson, and H. Madsen. Resolving nonstationary spectral information in wind speed time series using the Hilbert-Huang transform. *Journal of Applied Meteorology and Climatology*, 49:253–269, 2010.

[9] J.R. Kristoffersen and P. Christiansen. Horns rev offshore wind farm: its main controller and remote control system. *Wind Engineering*, 27:351–359, 2003.

[10] T. Gneiting. Editorial: Probabilistic forecasting. *Journal of the Royal Statistical Society*, 171:319–321, 2008.

[11] J.D. Hamilton. A new approach to the economic analysis of nonstationary time series and the business cycle. *Econometrica*, 57:357–384, 1989.

[12] L. Rabiner and B.H. Juang. *Fundamentals of speech recognition*. Englewoods Cliffs, New Jersey: Prentics-Hall, Int., 2005.

[13] R. Durbin, S. Eddy, A. Krogh, and G. Mitchison. *Biological sequence analysis*. Cambridge University Press, 1998.

[14] P. Pinson, L.E.A. Christensen, H. Madsen, P.E. Sørensen, M.H. Donovan, and L.E. Jensen. Regime-switching modelling of the fluctuations of offshore wind generation. *Journal of Wind Engineering and Industrial Aerodynamics*, 96:2327–2347, 2008.

[15] P. Pinson and H. Madsen. Adaptative modelling and forecasting of offshore wind power fluctuations with Markov-Switching autoregressive models. *Journal of Forecasting*, 2010. Available online.

[16] T. Bollerslev. Generalized AutoRegressive Conditional Heteroskedasticity. *Journal of Econometrics*, 31:307–327, 1986.

[17] H. Madsen, P. Pinson, T.S Nielsen, H.Aa. Nielsen, and G. Kariniotakis. Standardizing the performance evaluation of short-term wind power prediction models. *Wind Engineering*, 29:475–489, 2005.

[18] I. Sánchez. Short-term prediction of wind energy production. *International Journal of Forecasting*, 22:43–56, 2006.

[19] C. Vincent. *Mesoscale wind fluctuations over Danish waters*. PhD thesis, Risø - Technical University of Denmark, 2010. (ISBN 978-87-550-3864-6).

[20] A. Lau and P. McSharry. Approaches for multi-step density forecasts with application to aggregated wind power. *The Annals of Applied Statistics*, 4(3):1311–1341, 2010.

[21] T. Gneiting, K. Larson, K. Westrick, M.G. Genton, and E. Aldrich. Calibrated probabilistic forecasting at the Stateline wind energy center: The regime-switching space-time method. *Journal of the American Statistical Association*, 101:968–979, 2006.

[22] P. Pinson. On probabilistic forecasting of wind power time-series. Technical report, DTU Informatics, Kgs. Lyngby, 2010.

[23] F. Klaasen. Improving GARCH volatility forecasts with regime-switching GARCH. *Empirical Economics*, 27:363–394, 2002.

[24] S.F. Gray. Modeling the conditional distribution of interest rates as a regime-switching process. *Journal of financial Economics*, 42:27–62, 1996.

[25] R.S.J. Tol. Autoregressive conditional heteroscedasticity in daily wind speed measurements. *Theoretical and Applied Climatology*, 56:113–122, 1997.

[26] E. Cripps and W.T.M. Dunsmuir. Modeling the variability of Sydney Harbor wind measurments. *Journal of Applied Meteorology*, 42:1131–1138, 2003.

[27] B.T. Ewing, J.B. Kruse, and J.L. Schreoder. Time series analysis of wind speed with time-varying turbulence. *Environmetrics*, 17:119–127, 2006.

[28] S.D. Campbell and F.X Diebold. Weather forecasting for weather derivatives. *Journal of the American Statistical Association*, 100:6–16, 2005.

[29] J.W. Taylor and R. Buizza. A comparison of temperature density forecasts from garch and atmospheric models. *Journal of Forecasting*, 23:337–355, 2004.

[30] J.W. Taylor and R. Buizza. Density forecasting for weather derivative pricing. *International Journal of Forecasting*, 22:29–42, 2006.

[31] J.W. Taylor, P.E. McSharry, and R. Buizza. Wind power density forecasting using ensemble predictions and time series models. *IEEE Transactions on Energy Conversion*, 24:775–782, 2009.

[32] J. Cai. A Markov model of switching-regime ARCH. *Journal of Business & Economic Statistics*, 12:309–316, 1994.

[33] J.D. Hamilton and R. Susmel. Autoregressive conditional heteroskedasticity and changes in regime. *Journal of Econometrics*, 64:307–333, 1994.

[34] M. Haas, S. Mittnik, and M.S. Paolella. A new approach to Markov-Switching GARCH models. *Journal of financial Econometrics*, 2:493–530, 2004.

[35] S. Fruhwirth-Schnatter. *Finite mixture and Markov switching models*. Springer, 2006.

[36] J.S. Henneke, S.T. Rachev, F.J. Fabozzi, and M. Nikolov. MCMC-based estimation of Markov-Switching ARMA-GARCH models. *Applied Economics*, 43:259–271, 2011.

[37] C.W.S Chen, M.K.P. So, and E.M.H. Lin. Volatility forecasting with Double Markov switching GARCH models. *Journal of Forecasting*, 28:681–697, 2009.

[38] L. Bauwens, A. Preminger, and V.K.J. Rombouts. Theory and inference for a Markov switching GARCH model. *Econometrics Journal*, 13:218–244, 2010.

[39] Rydén T. EM versus Markov chain Monte Carlo for estimation of hidden Markov models: a computational perspective. *Bayesian Analysis*, 3:659–688, 2008.

[40] W.R. Gilks, S. Richardson, and D.J. Spiegelhalter. *Markov Chain Monte Carlo in practice*. Chapman & Hall, London, 1996.

[41] M. Tanner and W. Wong. The calculation of the posterior distributions by data augmentation. *Journal of the American Statistical Association*, 82:528–540, 1987.

[42] C.P. Robert, G. Celeux, and J. Diebolt. Bayesian estimation of hidden Markov chains: A stochastic implementation. *Statistics & Probability Letters*, 16:77–83, 1993.

[43] S.L. Scott. Bayesian methods for hidden Markov models: Recursive computing in the 21st century. *Journal of the American Statistical Association*, 97:337–351, 2002.

[44] S. Geman and D. Geman. Stochastic relaxation, Gibbs distribution and bayesian restoration of images. *IEEE Transactions on Pattern Analysis and Machine Intelligence*, 6:721–741, 1984.

[45] S. Chib. Calculating posterior distributions and modal estimates in Markov mixture models. *Journal of Econometrics*, 75:79–97, 1996.

[46] W.K. Hastings. Monte Carlo sampling methods using Markov chains and their applications. *Biometrika*, 57:97–109, 1970.

[47] C. Ritter and M.A. Tanner. Facilitating the Gibbs Sampler: The Gibbs stopper and the Griddy Gibbs sampler. *Journal of the American Statistical Association*, 87:861–868, 1992.

[48] L. Bauwens and M. Lubrano. Bayesian inference on GARCH models using the Gibbs sampler. *Econometrics Journal*, 1:23–46, 1998.

[49] M. Asai. Comparison of MCMC methods for estimating GARCH models. *Journal of the Japan Statistical Society*, 36:199–212, 2006.

[50] J.S. Liu, W.H. Wong, and A. Kong. Covariance structure and convergence rate of the Gibbs sampler with various scans. *Journal of the Royal Statistical Society, Series B*, 57:157–169, 1995.

[51] A. Gelman and D.B. Rubin. Inference from iterative simulation using multiple sequences. *Statistical Science*, 7:457–472, 1992.

[52] G.D. Forney Jr. The viterbi algorithm. *Proceedings of the IEEE*, 61(3):268–278, 1973.

[53] Z. Psaradakis and N. Spagnolo. Joint determination of the state dimension and autoregressive order for Markov regime switching. *Journal of Time Series Analysis*, 27:753–766, 2006.

[54] C.S. Cheung and P Miu. Currency instability: Regime switching versus volatility clustering. *Quarterly Journal of Finance & Accounting*, 48:67–81, 2009.

[55] C. Gallego, P. Pinson, H. Madsen, A. Costa, and A. Cuerva. Influence of local wind speed and direction on wind power dynamics - Application to offshore very short-term forecasting. *Applied Energy*, 88:4087–4096, 2011.

[56] G. Giebel, R. Brownsword, G. Kariniotakis, M. Denhard, and C. Draxl. The state-of-the-art in short-term prediction of wind power: A literature overview. Technical report, ANEMOS. plus, 2011.

[57] P. Pinson, C. Chevallier, and G. Kariniotakis. Trading wind generation with short-term probabilistic forecasts of wind power. *IEEE Transactions on Power Systems*, 22:1148–1156, 2007.

[58] T. Gneiting, F. Balabdaoui, and Raftery A.E. Probabilistic forecasts, calibration and sharpness. *Journal of the Royal Statistical Society B*, 69:243–268, 2007.

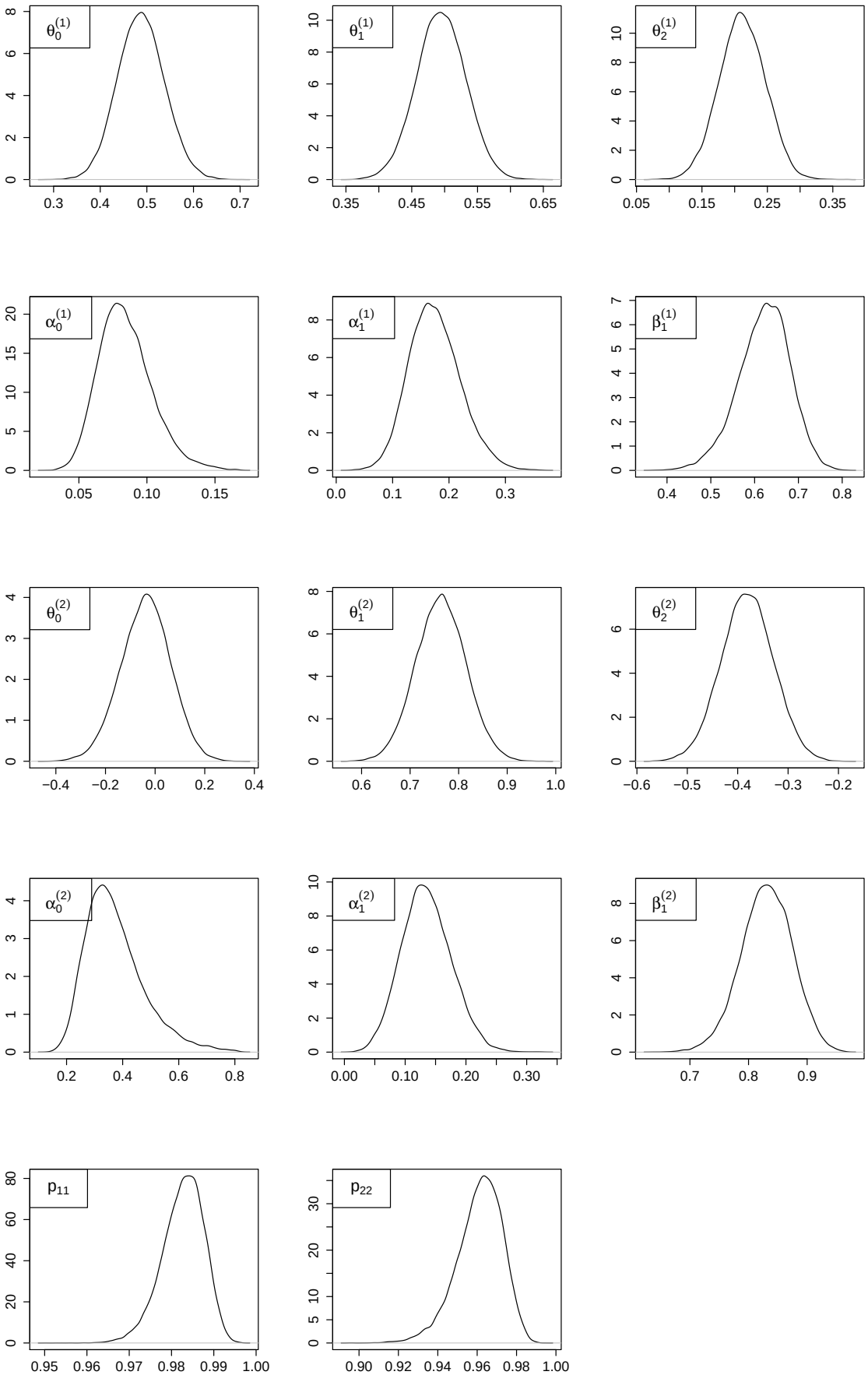

Figure 5: Estimated posterior densities of the simulated MS(2)-AR(2)-GARCH(1,1) process parameters.

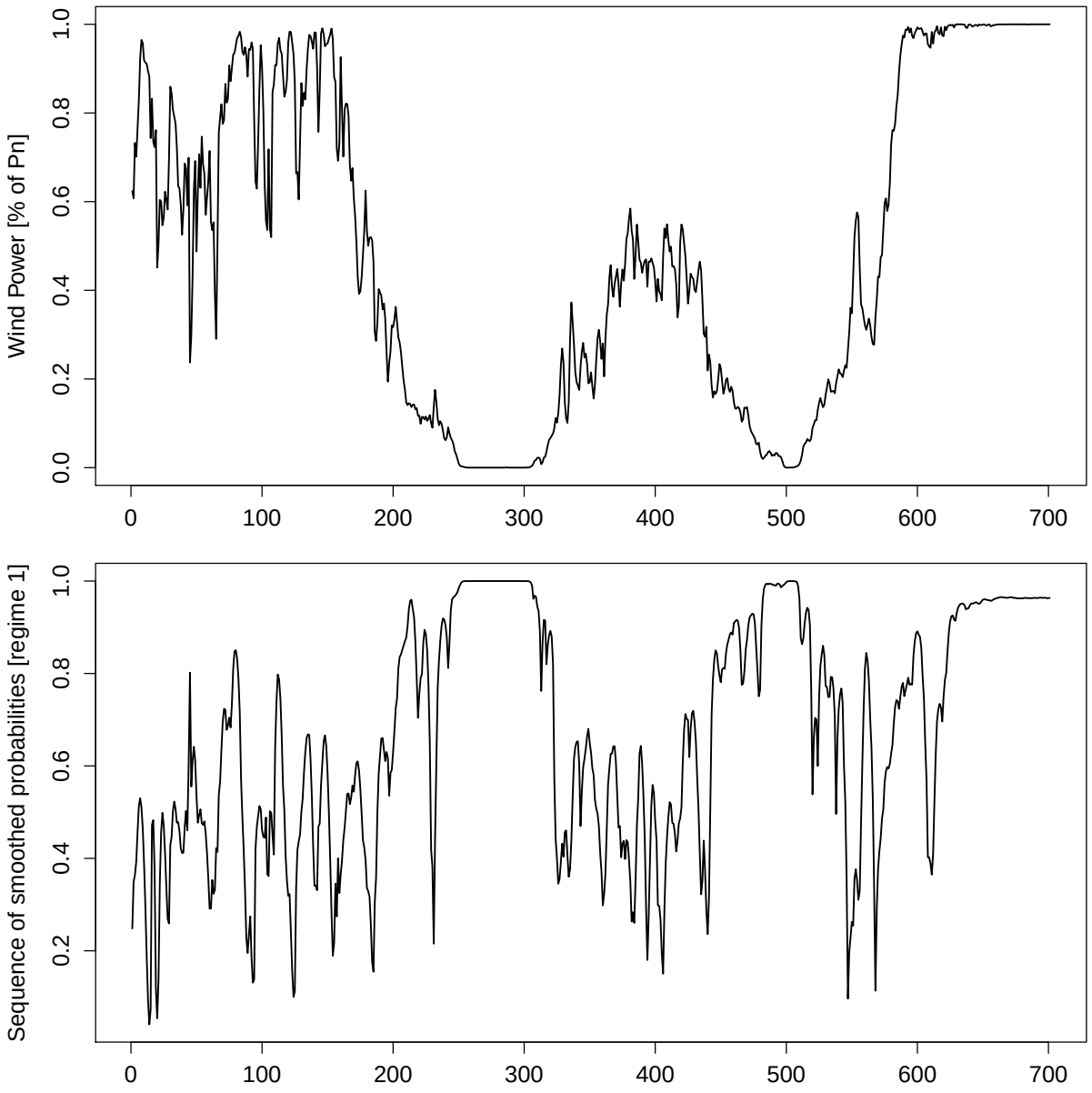

Figure 6: Time series of wind power and its estimated sequence of smoothed probabilities of being in regime 1 (i.e. low volatility regime).

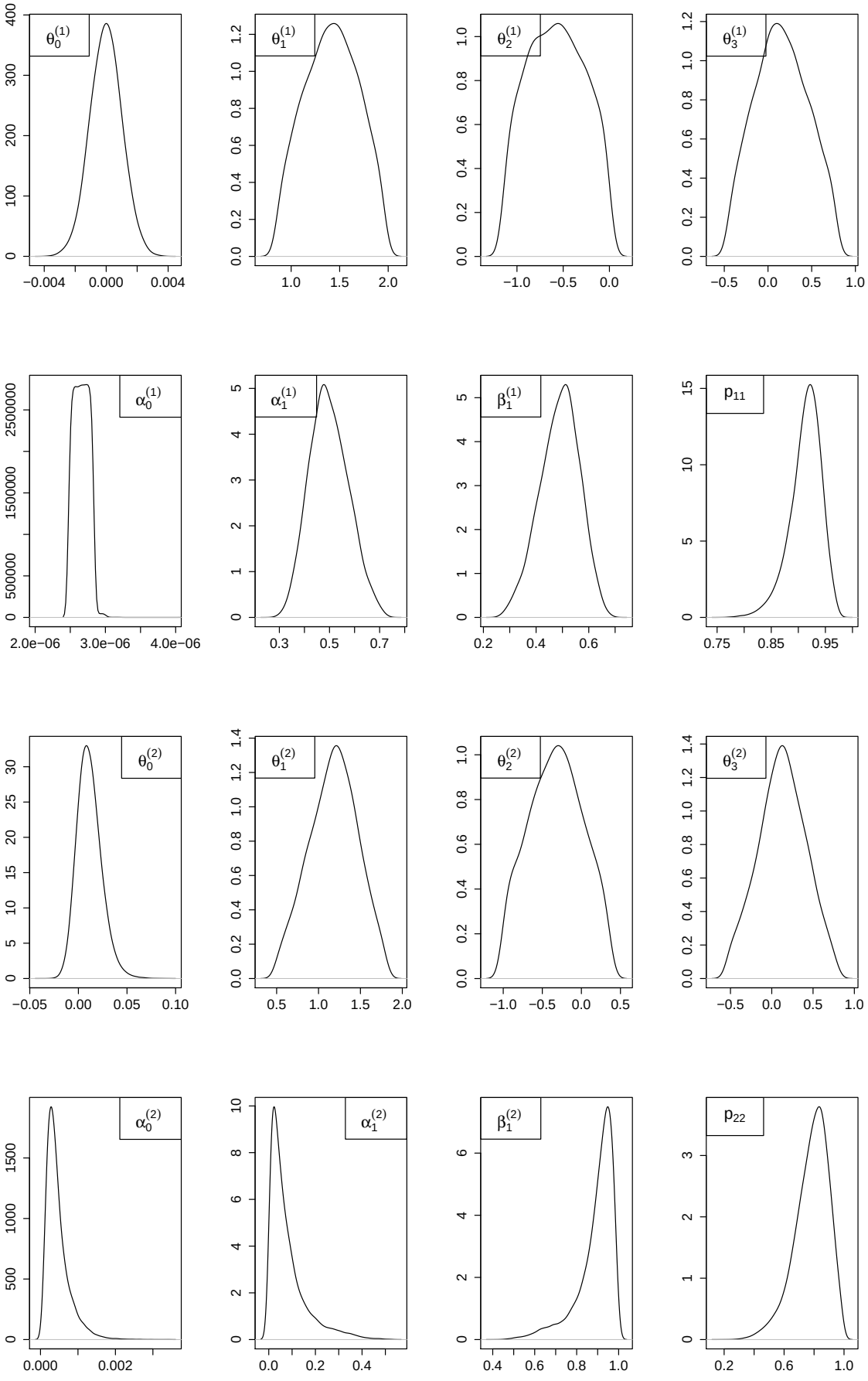

Figure 7: Estimated posterior densities of the MS(2)-AR(3)-GARCH(1,1) model fitted to the time series of wind power.

Risø DTU is the National Laboratory for Sustainable Energy. Our research focuses on development of energy technologies and systems with minimal effect on climate, and contributes to innovation, education and policy. Risø has large experimental facilities and interdisciplinary research environments, and includes the national centre for nuclear technologies.

Risø DTU
National Laboratory for Sustainable Energy
Technical University of Denmark

Frederiksborgvej 399
PO Box 49
DK-4000 Roskilde
Denmark
Phone +45 4677 4677
Fax +45 4677 5688

www.risoe.dtu.dk